BRASKI

DOE/ET-0058/5

Alloy Development for Irradiation Performance

Quarterly Progress Report
For Period Ending March 31, *1979*

U.S. Department of Energy
Assistant Secretary for Energy Technology
Office of Fusion Energy

Printed in the United States of America. Available from
National Technical Information Service
U.S. Department of Commerce
5285 Port Royal Road, Springfield,'Virginia 22161
NTIS price codes—Printed Copy: *A09* Microfiche A01

DOE/ET-0058/5
Distribution
Category
uc-20. 20c

ALLOY DEVELOPMENT FOR IRRADIATION PERFORMANCE QUARTERLY PROGRESS REPORT FOR PERIOD ENDING MARCH 31,1979

Compiled and Edited by Sigfred Peterson, ORNL
from Contributions of Participating Laboratories

ARGONNE NATIONAL LABORATORY

GENERAL ATOMIC COMPANY

HANFORD ENGINEERING DEVELOPMENT LABORATORY

McDONNELL DOUGLAS ASTRONAUTICS COMPANY

NAVAL RESEARCH LABORATORY

OAK RIDGE NATIONAL LABORATORY

WESTINGHOUSE FUSION POWER SYSTEMS

Date Published: April 1980

Prepared by
OAK RIDGE NATIONAL LABORATORY
Oak Ridge, Tennessee 37830
operated by
UNION CARBIDE CORPORATION
for the
DEPARTMENT OF ENERGY
Under Contract No. W-7405-eng-26

FOREWORD

This report is the fifth in a series of Quarterly Technical Progress Reports on *"Alloy Development for Irradiation Performance"* (ADIP), which is one element of the Fusion Reactor Materials Program, conducted in support of the Magnetic Fusion Energy Program of the U.S. Department of Energy. Other elements of the Materials Program are:

- *Damage Analysis and Fundamental Studies (DAFS)*
- *Plasma-Materials Interaction (PMI)*
- *Special-Purpose Materials (SPM)*

The ADIP program element is a national effort composed of contributions from a number of National Laboratories and other government laboratories, universities, and industrial laboratories. It was organized by the Materials and Radiation Effects Branch, Office of Fusion Energy, DOE, and a Task Group on *Alloy Development for Irradiation Performance*, which operates under the auspices of that Branch. The purpose of this series of reports is to provide a working technical record of that effort for the use of the program participants, for the fusion energy program in general, and for the Department of Energy.

This report is organized along topical lines in parallel to a Program Plan of the same title so that activities and accomplishments may be followed readily relative to that Program Plan. Thus, the work of a given laboratory may appear throughout the report. Chapters 1, 2, 7, and 8 review activities on analysis and evaluation, test methods development, status of irradiation experiments, and corrosion testing and hydrogen permeation studies, respectively. These activities relate to each of the alloy development paths. Chapters 3, 4, 5, and 6 present the ongoing work on each alloy development path. The Table of Contents is annotated for the convenience of the reader.

This report has been compiled and edited under the guidance of the Chairman of the Task Group on *Alloy Development for Irradiation Performance*, E. E. Bloom, Oak Ridge National Laboratory, and his efforts, those of the supporting staff of ORNL and the many persons who made technical contributions are gratefully acknowledged. T. C. Reuther, Materials and Radiation Effects Branch, is the Department of Energy Counterpart to the Task Group Chairman and has responsibility for the ADIP Program within DOE.

Klaus M. Zwilsky, Chief,
Materials and Radiation Effects Branch
Office of Fusion Energy

CONTENTS

1. ANALYSIS AND EVALUATION STUDIES

The designs for power-producing fusion reactors are in a very embryonic and rapidly changing state. Requirements for materials performance are thus not well defined. However, regardless of the final designs, the environment will clearly be extremely demanding on materials in regions of high neutron flux. One cannot identify a class of alloys on which the development efforts should focus — thus the parallel paths of the Alloy Development Program. The combination of reactor designs that are evolving and the necessity for including alloys with widely different physical, chemical, and mechanical properties in the program could lead to an impossibly large number of potential problems and possible solutions. Analysis and evaluation studies are an essential part of the Alloy Development Program in order to translate fusion reactor performance goals into material property requirements and to identify crucial and generic problems on which development activities should be focused. As the Alloy Development Program proceeds and a better understanding of the behavior of materials in potential fusion reactor environments is attained, these studies will also identify problems that will necessitate design solutions.

1.1 THE APPLICATION OF MAGNETIC STAINLESS STEELS TO TOKAMAK REACTOR DESIGN - S. D. Harkness, K. Evans, and L. Turner (Argonne National Laboratory)

1.1.1 ADIP Task

Task 1-A-1 Define Material Property Requirements and Make Structural Life Prediction.

1.1.2 Objective

The objective of this work is to establish from a plasma engineering view whether or not magnetic materials can be considered as tokamak reactor structural materials.

1.1.3 Summary

An assessment of the effect of using a martensitic stainless structure on the MHD equilibrium and the pulsed field penetration times has revealed no significant detrimental effects as long as the material is saturated by the TF coils. Experimental measurements of the B-H curve of an improved 9-Cr stainless steel developed by Combustion Engineering has shown that this material saturates at ∿ 1.8 T at room temperature. To put this in perspective a 7 meter major radii tokamak with a maximum field of 9 T imposes a steady-state field of 3.3 T on the outer blanket first wall and of 3.0 T on the furthest edge of a meter thick blanket/shield system.

Operation of a substantial portion of the blanket system with a ferritic steel therefore appears possible. An analysis of the pressures imposed OR a ferritic first wall/blanket structure using the Rutherford three dimensional code has shown that these will vary from 1 to 10 atmospheres, depending on the thickness of ferritic stainless used. These pressure levels are well within the structural design capability.

1.1.4 Progress and Status

Martensitic stainless steels offer the potential of significantly improved lifetimes in a fusion reactor environment over austenitic stainlesses. This possible incremental gain in performance is based on

the dimensional stability observed over a wide range of temperature and fluence in the LMFBR program and to their inherently better performance under cyclic thermal loading. For a given thermal loading the thermal stress is reduced by roughly a factor of two over what would be expected in a Type 316 stainless steel. Since crack growth rates and fatigue lives are dependent on the stress level raised to an exponent of from four to six, this factor of two reduction in stress is translated into significantly increased wall lifetimes.

A major obstacle to the use of the ferritic stainless steels in tokamak systems has been their ferromagnetic nature. To determine the consequences of this for both the plasma engineering and the structural design aspects of the system, initial analysis has been conducted in the areas of MHD equilibrium, pulsed field penetration times, and magnetic first wall pressures.

From a plasma engineering viewpoint the key result has been that as long as the structure is saturated by the steady-state toroidal fields, neither the MHD equilibria or feedback systems are significantly affected. MHD equilibria analyses were conducted by Ken Evans using existant codes as a function of the toroidal field and the thickness of the ferritic structure.

Evans also has calculated the time for pulsed magnetic field to diffuse through a conducting boundary and found that fifty percent of the field will penetrate in a time given by $0.35\ \mu\sigma a\Delta$ and 99% in a time of $3.4\ \mu\sigma a\Delta$ where μ is the permeability, σ is the conductivity, a is the radial distance to the first conducting wall and Δ is the wall thickness. Table 1.1.1 shows the expected ranges of these parameters as represented by different reactor designs and structural material choice. It can be seen that the 20% variation in permeability introduced by the application of ferritics is a minor perturbation when compared to the possible variation in the other parameters.

The magnetostatic pressures on a 3 cm thick ferritic stainless steel first wall structure are shown in Figure 1.1.1 as calculated from the Rutherford 3-d code. These pressures increase roughly linearly with increasing thickness of the ferritic region. Thus, if ferritics were used for the first 20 cm of structure (or in the region where radiation

Table **1.1.1** Typical Ranges for Field Penetration Parameters

$t \alpha \mu \sigma a \Delta$

	μ	σ	a, M	Δ, CM
AUSTENITIC	1.0	0.002 - 0,005	1.6 - 2.5	0.3 - 3
FERRITIC	1.0 - 1.2	0.002 - 0.005	1.6 - 2.5	0.3 - 3
TITANIUM	1.0	0.001	1.6 - 2.5	0.3 - 3

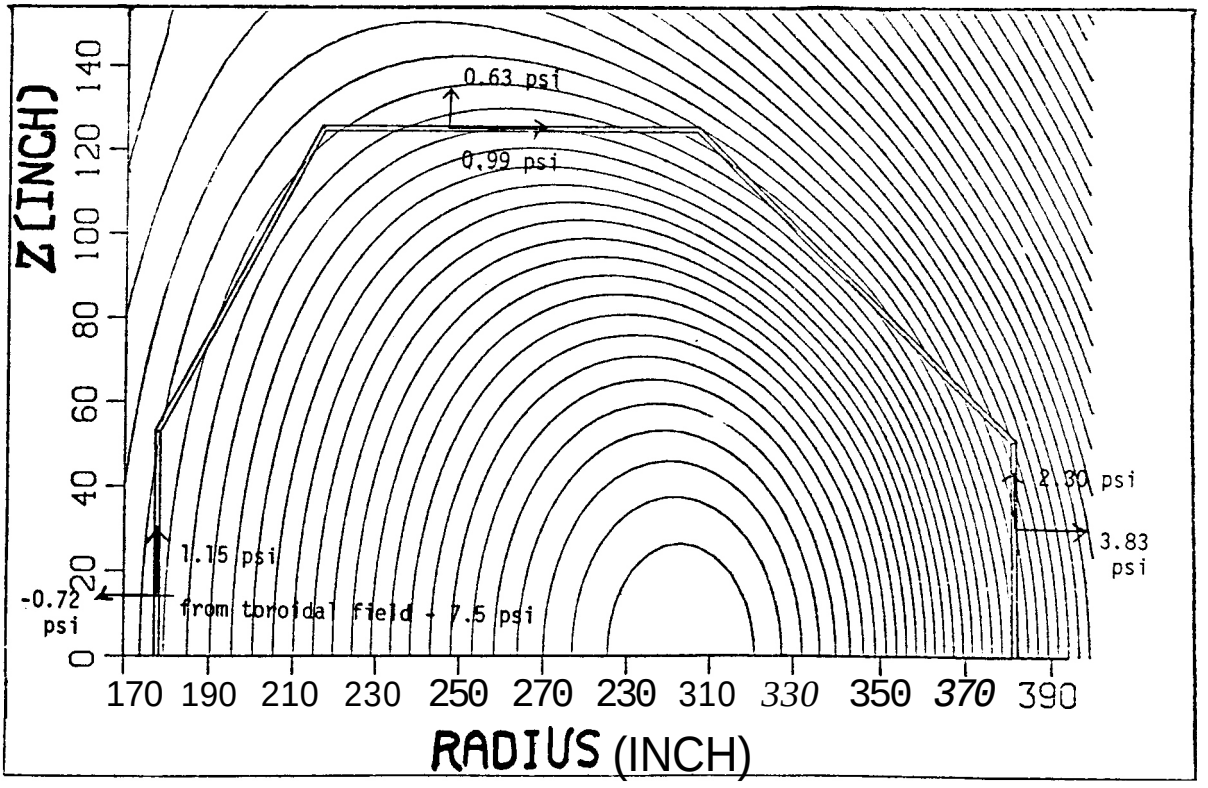

Figure **1.1.1** Forces on 3 cm ferritic stainless steel can from EF & TF coils.

effects are expected to be important) pressures of 50 psi might be expected. These are well within the levels that can be accomodated by the structural design.

1.1.5 Conclusions

The plasma engineering consequences of using magnetic structural materials such as the stabilized 9–Cr stainless steels appear to be small. Attention to the development of material property data is needed, particularly in the areas of radiation effects on the ductile–brittle transition temperature, helium effects, and cyclic mechanical properties.

1.2 FERRITIC STAINLESS STEELS FOR FUSION APPLICATIONS — S. N. Rosenwasser, P. Miller, J. A. Dalessandro, and J. M. Rawls (General Atomic Company).

1.2.1 ADIP Task

ADIP Task I.A.1, Define material property requirements and make structural life predictions.

1.2.2 Objective

The objective of this study is to assess the feasibility of incorporating ferromagnetic (martensitic) steels in fusion reactor designs and to evaluate the advantages of this class of material with respect to first wall/blanket lifetime. The irradiated and unirradiated property data needed for the application of ferritic stainless steels in fusion designs are also being defined as part of this task.

1.2.3 Summary

An assessment was made of the feasibility and design impact of using a ferromagnetic martensitic stainless steel such as HT9 in first wall/blanket structures. The results of this preliminary evaluation suggested that use of Fe–Cr martensitic stainless steels in fusion first-wall/blanket structures might result in significantly increased component lifetimes relative to 20% cold-worked type 316 stainless steel, particularly up to operating temperatures of about 520°C. Measurements of some pertinent magnetic properties and the results of rough calculations indicated that the effects of ferromagnetic walls on the static and dynamic fields required for plasma confinement will be relatively minor and could be accommodated by proper reactor design.

1.2.4 Progress and Status

Recent results from fast-fission reactor irradiation experiments in the United States and Europe suggest that the Fe–Cr martensitic stainless steels might offer the potential of significantly greater first wall/blanket lifetimes and, therefore, should be given serious consideration. The general class of alloys under consideration are ferromagnetic steels containing from about 9 to 13 percent Cr with some small additions of

various strengthening and stabilizing elements such as Mo. These steels are conventionally used in the normalized and tempered condition for high temperature applications' and can compete favorably with austenitic alloys up to about 600°C. Although the heat treatment can result in either a tempered martensite or bainite structure, depending on the alloy and thermal treatment parameters, this class of materials will be referred to as "martensitic" stainless steels for simplicity.

On the basis of impressive EBRII irradiation test results, the alloy Sandvik HT9 (DINX20CrMoWV121) was among a group of six prime advanced candidate materials identified by the United States National FBR Cladding/Duct Materials Development Program and is in fact the only commercial candidate alloy. Because of the encouraging and rapidly expanding data base from the FBR Program, the significant application history and the current interest in the alloy, HT9 was selected as a representative martensitic alloy for the current evaluation.

The nominal composition of alloy HT9 is given in Table 1.2.1. For high temperature, extended time service, the alloy is usually heat treated at 1050°C for 0.5 hr, air cooled and then tempered at 780°C.

Table 1.2.1. Nominal Composition of Alloy HT9 in Weight Percent

Fe	Cr	Ni	Mo	W	V	Si	Mn	C
Balance	11.5	0.5	1.0	0.5	0.3	0.25	0.5	0.20

1.2.4.1 Mechanical Behavior

The strength of HT9 is compared to that for several other candidate first wall/blanket alloys in Fig. 1.2.1. The variation of minimum ultimate tensile strength with temperature is plotted for HT9[2], 20% cold-worked type 316 stainless steel (20CW316); annealed 316 stainless steel (316), Inconel 718[3], titanium alloys Ti-6Al-4V and Ti-6A1-2 Sn-4 Zr-2 Mo[4], vanadium alloy V-20 Ti[5], and niobium alloy Nb-1 Zr[6]. It is evident that the short term strength of HT9 is between that for type 316 and 20% cold-worked type 316 stainless steel to about 500°C, is equivalent to that for 316 at about 550°C, and is similar to that for Ti-6Al-4V at about 550°C. Above 500°C HT9 short term strength decreases rapidly.

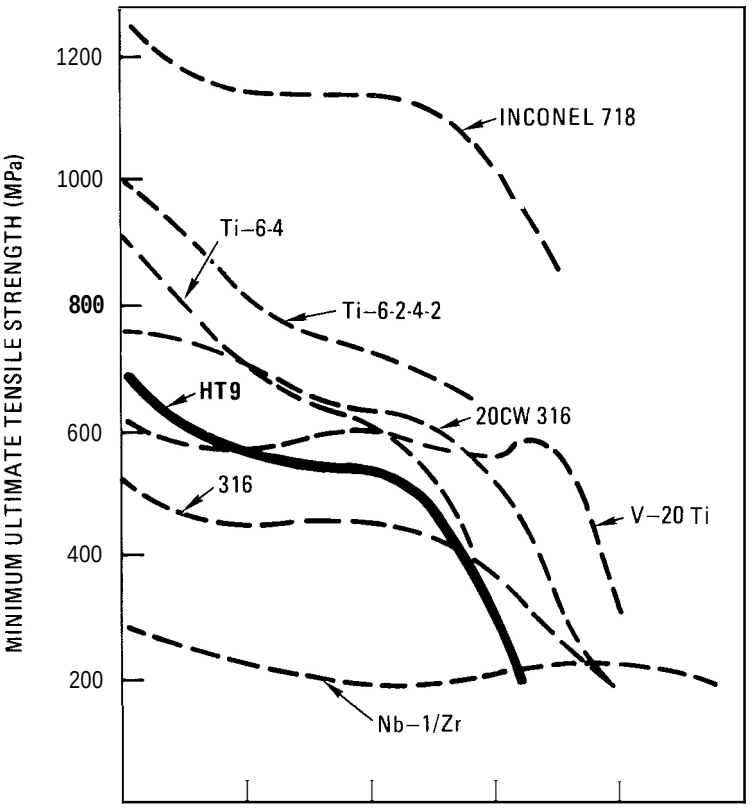

Fig. 1.2.1. Minimum Ultimate Strength of HT9 and Other Candidate Alloys.

Thermal stresses are an important source of cyclic fatigue and creep fatigue damage, particularly in pulsed tokamak fusion systems. The comparative resistance to thermal stress can be estimated by a parameter, M, which is a function of thermal conductivity, thermal expansion coefficient, Poisson's ratio, Young's modulus and yield strength. Thermal stress resistance increases with increasing value of M. Thermal stress resistance of HT9 at 500°C is compared to that of other candidate materials in Table 1.2.2. The significantly higher thermal conductivity and lower thermal expansion coefficient of ferritic HT9 relative to austenitic 316 provides the former with a significantly greater resistance to thermal stress effects. Thermal stress resistance of HT9 is slightly lower than that for the Ti alloys and for the precipitation strengthened Ni alloy 718.

Table 1.2.2. Thermal Stress Resistance of Candidate Fusion Alloys at 500°C

Alloy	Thermal Stress Resistance M (W/m) × 10^{-3}
Annealed 316	1.3
20CW316	4.9
HT9	8.5
Ti-6Al-4V	10.2
Ti-6Al-2Sn-4Zr-2Mo	10.4
Inconel 718	10.7
V-20Ti	12.3
Nb-1Zr	19.8

where $M = \frac{2\sigma_Y K(1 - \nu)}{\alpha E}$

and σ_Y = yield strength
K = thermal conductivity
ν = Poisson's ratio
α = thermal expansion coefficient
E = Young's modulus

1.2.4.2 Radiation Damage Resistance

The primary reason for investigating the application of HT9 is, of course, its apparent resistance to neutron radiation damage. Most of the pertinent information with respect to void swelling, in-reactor creep, and embrittlement has been developed in the United States FBR program, and has not yet been released for general dissemination. Although discussion of the radiation damage resistance of HT9 must therefore be qualitative, a number of relevant observations can be made on the basis of EBR II data to exposures greater than 1×10^{23} n/cm^2 (E > 0.1 MeV).

Void swelling in HT9 is at least an order of magnitude less than in 20% cold-worked 316. Ccrrent results indicate that swelling is even lower than the 3.7%, 500°C peak swelling at 150 dpa previously reported for HT9 under heavy ion bombardment.[7] The currently published equation for 20% cold-worked 316[8] predicts peak swelling of about 60% at 580°C and 100 dpa. In addition, in-reactor creep resistance of HT9 appears better than that for 20% cold-worked 316 to temperatures in excess of 600°C.[9]

Although only low helium levels and low helium/dpa ratios relative to fusion neutron conditions have been evaluated, tensile ductility

retention of HT9 appears superior to that for 20% cold-worked 316 (particularly when tested above the irradiation temperature) and vastly superior to that for the precipitation strengthened nickel alloys up to 600°C. Furthermore, the microstructure of HT9 appears stable under irradiation in the temperature range of interest, but the upward shift in ductile-brittle transition temperature and the upper and lower shelf fracture energies after irradiation must be determined.

1.2.4.3 Preliminary Comparative Lifetime Analysis

A preliminary evaluation of the lifetime of an HT9 first wall/blanket module relative to the lifetimes of 20% cold-worked 316 and Inconel 718 was made, assuming a helium cooled cylindrical module developed for GA's demonstration plant reactor.[11] The following design parameters were used:

Neutron wall loading	1.0 MW/m^2
Module radius	0.25 m
Helium pressure	4.1 MPa
Helium inlet temperature	285°C
Helium outlet temperature	585°C
Burn time	300 s
Dwell time	30 s

The analysis, which has been described in detail,[12] employs a computer program which integrates material property data with thermal and stress analysis. Prior to calculating wall life, adequate strength is checked for based on established ASME B&PV Nuclear Code allowable values for pressure stress and combined pressure and thermal stress. In this preliminary analysis, only creep-fatigue interactions, fatigue flaw growth and volume change from stress-free swelling were considered as life-limiting mechanisms. Irradiation (helium) embrittlement was taken into account by assuming a fluence independent operating temperature limit of 550°C for all three materials. The effect of irradiation on creep, fatigue and fatigue flaw growth was neglected as were differential swelling stress and the effects of stress and helium production on swelling stress and the effects of stress and helium production on swelling. The end-of-life criteria used were creep-fatigue, cyclic flaw growth, swelling and residual ductility.

Creep-fatigue life was calculated according to ASME Code Case N47 (1592) using linear creep-fatigue interaction. Cyclic flaw growth was based on the growth to penetration of a minimum detectable 0.75 mm radius semi-circular surface flaw oriented normal to the principal stress, located on the inside surface of the minimum wall section. Swelling life was taken as that for two percent volume change. In the absence of definitive data, it was assumed that any finite fluence produced sufficient helium to reduce ductility to the two percent limit at 550°C and above in all three alloys.

The data used for this analysis was a combination of published[2,11-16] and recent unpublished information. A key assumption was that the S-N fatigue and flaw growth curves of 20% cold-worked 316 and HT9 were identical in the temperature range of interest. No high temperature flaw growth data was located for HT9, but low temperature data on a similar martensitic steel'[7] indicated that this is a reasonable assumption.

The results of this preliminary analysis are shown in Fig. 1.2.2, which gives the predicted lifetime of HT9, 20% cold-worked 316 and

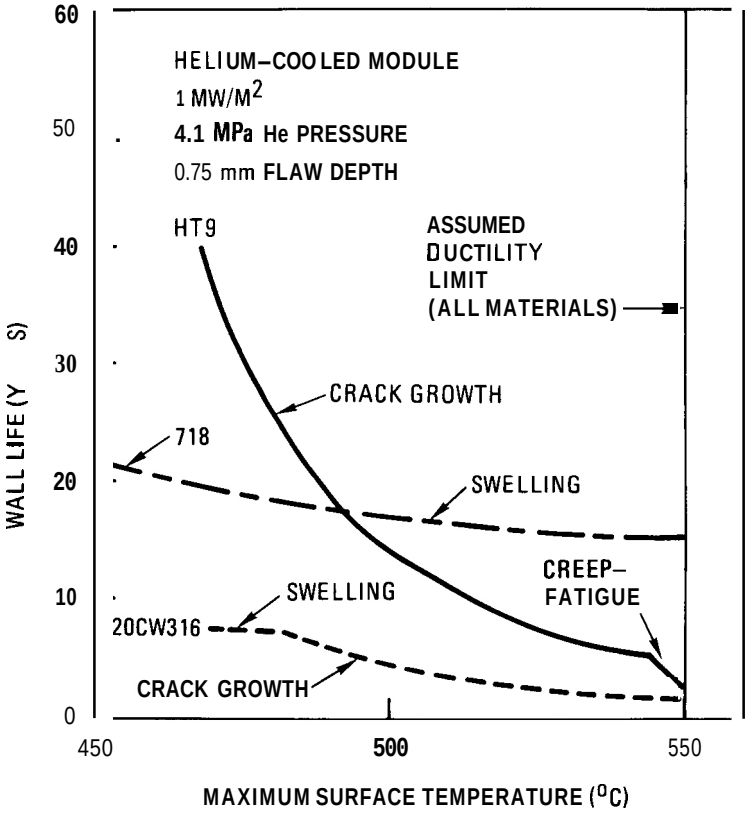

Fig. 1.2.2. Preliminary Wall Life Comparison of HT9, 20% Cold-Worked 316 Stainless Steel and Inconel 718.

Inconel 718 as a function of maximum surface temperature. Only the controlling life limiting modes are shown for each material. Although the quantitative results must be considered in the context of the limited available data and the limited number of failure modes considered, a number of conclusions can be drawn. First, at temperatures from 470°C to about 520°C, HT9 offers the possibility of significantly greater lifetimes than 20% cold-worked 316 because of HT9's much greater resistance to swelling and because of its lower rate of crack growth. The better crack growth resistance of HT9 is due to lower thermal bending stresses. (The crack growth rate-stress intensity factor curves for HT9 were assumed identical to those of 20% cold-worked 316.) Second, due to its better swelling resistance, HT9 may give greater lifetimes at temperatures below 500°C than high strength nickel base alloys, such as Inconel 718. At higher temperatures the superior crack growth resistance of 718 dominates, although above 500°C there is growing concern with radiation embrittlement of these precipitation-strengthened nickel alloys. Finally, creep-fatigue considerations may limit the maximum allowable service temperature of HT9 to about 500°C.

1.2.4.4 Magnetic Properties and Effect on Reactor Performance

Alloy HT9 is a hard magnetic material with a large area inside the hysteresis loop (induction versus magnetizing force); hence, its dynamic magnetic properties depend on the past history of the material. For fusion reactor applications, however, only magnetic properties when the steel is saturated by the toroidal field are of specific interest. Because the required information on magnetic properties was not available in the literature, several exploratory measurements were made at General Atomic on commercial grade HT9 tube, heat treated as described previously. Typical hysteresis loops were measured at 23°C and 538°C as shown in Fig. 1.2.3. The important result is that the saturation induction decreases from 1.3 tesla at 25°C to 1.0 tesla at 538°C at a magnetizing field of 8×10^3 amp-turns/meter.

In the second type of experiment a torus of HT9 was wound with primary and secondary windings to permit measurement of the small signal magnetic permeability as a function of bias fields. Table 1.2.3 displays the permeability for various values of applied magnetic field. The table

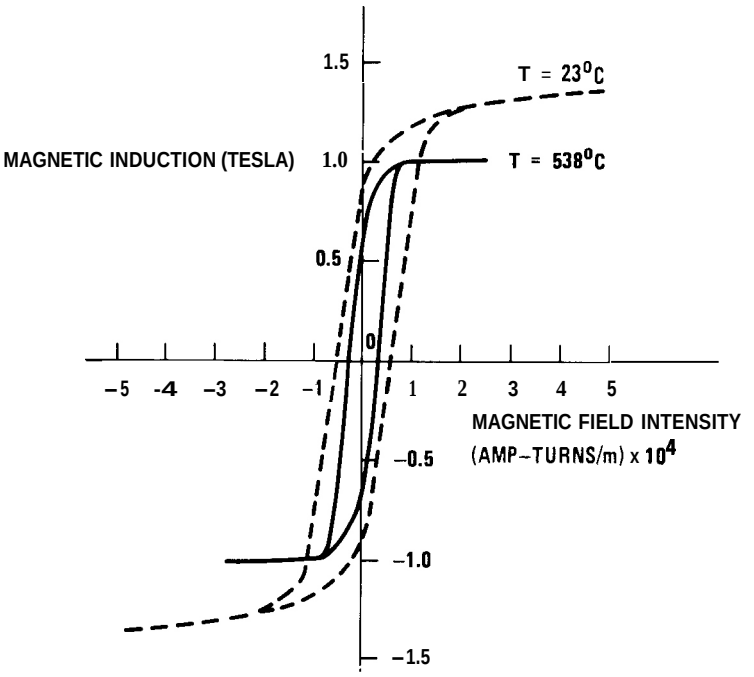

Fig. 1.2.3. Hysteresis Loops of HT9 Measured at 23°C and 538°C.

Table 1.2.3. A-c Permeability of HT9 at 315°C as a Function of Bias Field, up to the Assumed Toroidal Field of 3T

Applied Magnetic Field (T)	0.03	0.3	0.6	1.2	2.2	3.0
Permeability	76	73	12	2.0	1.2	1.2

demonstrates that as the toroidal field increases toward its expected reactor operating value of 3T, which saturates the material, the a-c permeability decreases to within 20% of the asympotic theoretical value of unity. Even if the a-c permeability is as high as 1.2 it will be shown later that the impact on plasma shaping and control is negligible.

Further measurements were taken in a configuration with two circular coils wound around a cylindrical tube of HT9. One coil was located above and the other below the equatorial plane. The measured mutual inductance

for increasing magnitude of the bias field was compared with the calculated value for the same two coils in vacuum. The results, accurate to within about 10%, are shown in Fig. 1.2.4, and provide further evidence that HT9 behaves as a non-magnetic material under typical reactor conditions.

The field of non-linear magnetic control devices has long exploited the fact that when a magnetic substance is saturated in one direction, a perpendicular field will see a permeability very close to unity. In a tokamak power reactor, the toroidal field will saturate the region near the plasma so that the poloidal coil system will see an essentially non-magnetic metal when HT9 or a similar ferritic alloy is used as a construction material.

The steady state magnetic field in the plasma region is disturbed only slightly by the extra magnetic flux in the wall materials associated with the saturation induction of 1T determined in the hysteresis loop measurements. The effect of apertures or abutments in the ferromagnetic

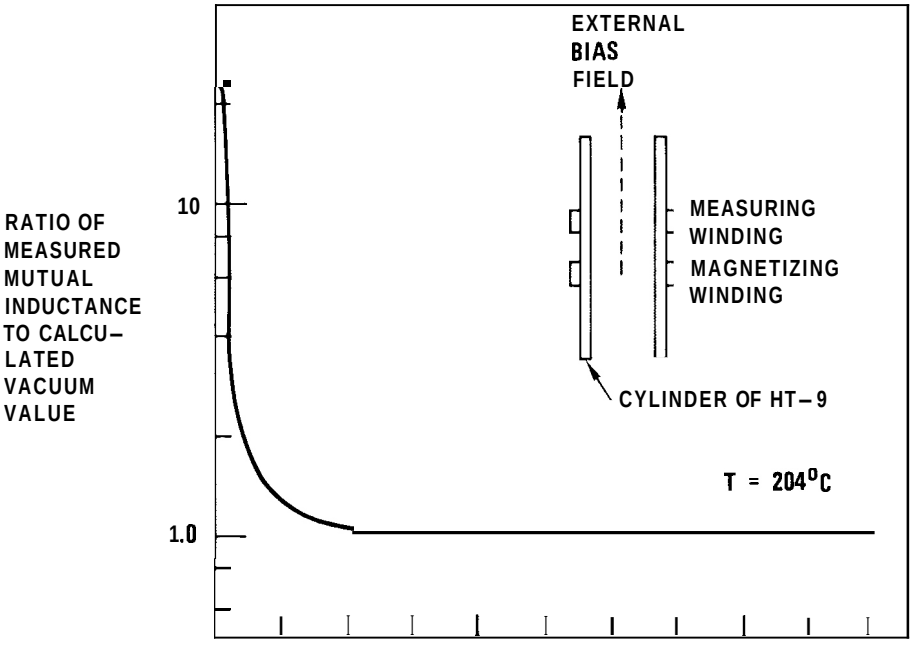

Fig. *1.2.4.* Ratio of Measured Mutual Inductance of Two Coils Wound Around HT9 to Calculated Mutual Inductance for Same Coils in Vacuum at 204°C as a Function of Bias Field, up to an Assumed Toroidal Field of 3T.

walls would be to cause local plus and minus variations of the magnetic field. In fact, it has been suggested that careful placement of ferromagnetic material in a tokamak could result in a dramatic reduction in the field ripple caused by the return legs of the toroidal field coils.[18]

A number of other effects of ferromagnetic walls, such as the perturbations in plasma shaping fields, time constants for induced eddy currents and losses associated with cyclic operation of magnetic material have been quantified, and should not result in significant design constraints. Body forces arising from asymmetric first wall/blanket design, such as may be caused by apertures or abutments, may give rise to local surface pressures of less than 1 MPa, which in turn could cause stress in the wall material of about 10 MPa in a typical power reactor design.

1.2.4.5 Conclusions

It is clear that additional data must be obtained concerning magnetic properties, mechanical behavior (particularly fatigue flaw growth), irradiation effects on properties (particularly the synergistic effects of displacement damage and helium gas production), fabrication and compatibility. The effect of both thermal and irradiation environments on DBTT shift and other fracture properties must be fully characterized. Further, more sophisticated analysis concerning the impact of ferromagnetic materials on design must be performed. However, the results to date indicate that martensitic steels may have excellent potential as candidate fusion reactor materials.

1.2.5 References

1. R. T. King, G. M. Goodwin, R. L. Heestand, J. H. Devan, and H. C. McCurdy, "Alternate Structural Materials for Liquid Metal Fast Breeder Reactors," *Symposium on Structural Material for Service at Elevated Temperatures in Nuclear Power Generation,* A. O. Schaefer, Ed., Houston, Texas, November 1975, ASME, New York, p. 375.
2. J. E. Chafey and J. B. Wattier, "Estimation of Allowable Design Stress Values for 12 Cr-1Mo-0.3V Steel," General Atomic Report GA-A14610, February 1978.

3. J. C. Spanner, Ed., *Nuclear Systems Materials Handbook, Vol. 1, Design Data,* TID 26666, Handford Engineering Development Laboratory (1976).
4. *Metallic Materials and Elements for Aerospace Vehicle Structure,* HIL-HBKC-5B, Sections 5.3.3 and 5.4.3, USAF (1975).
5. R. E. Gold, D. E. Harrod, R. L. Ammon, R. W. Buckman, Jr. and R. S. Svedberg, "Technical Assessment of Vanadium Base Alloys for Fusion Reactor Applications," Final Report No. COO-4540-1, Westinghouse Electric Corp., April 1978, p. 112.
6. J. W. Davis and G. L. Kulcinski, "Assessment of Titanium for Use in the 1st Wall/Blanket Structure of Fusion Power Reactors," EPRI ER 386, McDonnell Douglas Astronautics Company, April 1977, p. 10.
7. F. A. Smidt, P. R. Malmberg, J. A. Sprague and J. G. Westmoreland, "Swelling Behavior of Commercial Ferritic Alloys, EM-12 and HT-9, as Assessed by Heavy Ion Bombardment," in *Irradiation Effects on the Microstructure and Properties of Metals,* ASTM STP #611, American Society for Testing and Materials (1976) p. 227.
8. J. C. Spanner, Ed., *Nuclear Systems Materials Handbook, Vol. 1, Design Data,* TID 26666, Handford Engineering Development Laboratory (1976), Section 5.
9. B. A. Chin, E. R. Gilbert, M. M. Paxton and J. L. Straalsund, "A Comparison of the In-Reactor Creep Behavior of Selected Commercial Alloys at a Temperature of 593°C," presented at 9th ASTM International Symposium on Effects of Radiation on Structural Materials, Richland, Washington, July 1978.
10. D. W. Kearney, D. W. Culver, J. A. Dalessandro, S. N. Rosenwasser, D. L. Vrable and C. Wong, "Mechanical and Thermal Design of a Gas-Cooled Fusion Blanket Module," *Proc. of 7th Symposium on Engineering Problems of Fusion Research, Knoxville, Tennessee, October 25-28, Vol. 11,* p. 1483.
11. *Nuclear Systems Materials Handbook, Vol. 1, Design Data,* TID-26666, Handford Engineering Development Laboratory (1976), Book 1, Sections 4 and 5, Book 2, Section 5.
12. P. Soo and J. McAndrew, "Type 303 and Type 316 Stainless Steel Data for High Temperature Design," Westinghouse Report WARD 3045T2C-3.

13. C. R. Brinkman and G. E. Korth, "Strain Fatigue and Tensile Behavior of Inconel 718 from Room Temperature to 650°C," ANCR-1125, August 1973.

14. L. A. James, "Fatigue-Crack Growth in 20% Cold-Worked Type 316 Stainless Steel at Elevated Temperature," Nucl. Tech. 16, 316, October 1972.

15. L. A. James, "Fatigue-Crack Propagation Behavior of Inconel 718," HEDL-TME 75-80, September 1975.

16. J. Z. Briggs and T. D. Parker, *The Super 12% Cr Steels*, Climax Molybdenum Company, New York (1965).

17. W. G. Clarke, Jr., "The Fatigue Crack Growth Rate Properties of Type 403 Stainless Steel in Marine Turbine Environments," *Corrosion Problems in Energy Conversion and Generation*, Electrochemical Society (1974) p. 368.

18. L. R. Turner, S. T. Wang and H. C. Stevens, "Iron Shielding to Decrease Toroidal Field Ripple in a Tokamak Reactor," Third *ANS* Topical Meeting on the Technology of Controlled Nuclear Fusion, May 9-11, 1978, Santa Fe, New Mexico (to be published).

2. TEST MATRICES AND TEST METHODS DEVELOPMENT

An important part of the alloy development effort is the definition of test matrices and development of test methods. The alloy development strategy will proceed through stages requiring tests of generally increasing difficulty and complexity.

1. Scoping tests will be used to make relative judgments between materials and metallurgical conditions and to identify critical properties. Such tests, which will be used where large numbers of variables are involved, must be rapid, simple, and decisive.

2. Developmental tests will be used for optimization of the Prime Candidate Alloys. They will be broader and more extensive than the scoping tests. In-reactor testing will be an important part of this work.

3. Engineering property tests will be devised to provide the broad data base needed for reactor design.

2.1 DESIGN OF MATERIALS IRRADIATION EXPERIMENTS IN THE ORR UTILIZING SPECTRAL TAILORING AND REENCAPSULATION — T. A. Gabriel, K. R. Thoms, and M. L. Grossbeck (ORNL)

2.1.1 ADIP Task

ADIP Task I.A.2, Define Test Matrices and Test Procedures.

2.1.2 Objective

The helium and displacement rates for stainless steel and nickel-base alloys can be controlled in fission reactors by varying the thermal-to-fast neutron flux ratio. The helium production will be dominated by the thermal flux and the fast flux will determine the dpa. In the ORR these rates can be adjusted to match the predicted rates for a fusion reactor first wall. The objective of this work is to determine the amount of variation necessary and to design reactor core pieces that will produce the needed changes. The capsule must also be capable of discharging specimens and being reloaded with radioactive specimens.

2.1.3 Summary

We are designing an experiment to achieve the proper He/dpa ratio to simulate fusion reactor conditions for Paths A and B alloys with the Oak Ridge Research Reactor. The composition and geometry of the shields (core pieces) to tailor the spectrum as well as to determine the times to change core pieces are now being calculated. The conceptual design is now complete, following a major revision.

2.1.4 Progress and Status

The ORR will be used because of its large experimental volume, capability for active instrumentation, and favorable neutron energy spectrum. Since the helium production rate in nickel in a fission reactor is not linear, the neutron spectrum must be tailored during the irradiation to achieve and maintain the correct He/dpa ratio.

The conceptual design of the proposed spectral tailoring experiments has changed significantly during this report period. Because

of the steep axial flux gradient in the ORR core, we have decided to use only 152 mm of the axial test space available, centered about the average axial flux peak. Two capsules will be operated concurrently to provide the four desired test temperatures. One capsule will have test regions of 300 and 400°C while the other will have test regions of 500 and 600°C. Each test region will be an annulus measuring approximately 38 mm OD by 13 mm ID by 70 mm long. Temperatures in each test region will be measured by three Chromel—P vs Alumel thermocouples placed in the central spline. Temperature will be controlled by varying the mixtures of inert gases (helium, neon, and/or argon) in a control gas annulus immediately outside the test region. All test specimens will be immersed in NaK to minimize the temperature gradients.

The design allows for the assembly of the entire capsule except the two bottom end caps before placing the test specimens in the capsule. This design feature was incorporated to simplify the reencapsulation of previously irradiated specimens. A completed capsule assembly will be placed in a shielded carrier and the open bottom end of the capsule will protrude into an opening in the hot cell wall. The test specimens, which will have been previously loaded into a holding fixture, will then be slid into the capsule along with the first end plug. This first end plug will serve as a radiation shield and the entire capsule can be removed from the hot cell area. The plugs will then be welded in place. The capsule and shield carrier will then be uprighted for NaK filling.

A detailed design is being prepared. Design of the in-core section is scheduled to be completed first. Parts will then be fabricated to build a prototype of this section to confirm the temperature control capability of the design.

A gamma heat measuring device has been designed and parts have been fabricated. During the next report period, this device will be assembled and the gamma heat will be measured in the two planned core irradiation positions (E-3 and E-7).

Concurrently with the engineering design, the spectral tailoring calculations are being fine-tuned. Newly revised cross-section data have been received and include data for tantalum and tungsten. Initial calculations using the new data have been completed.

The new results are different from the old results in two important areas: k-effective and neutron flux levels. The new k-effective value obtained is about 4% less than previously calculated for the same location of the shim rods. Because of this, the shim rods must be adjusted outward by 0.10 m in order to obtain a k-effective of 1. This movement of the shim rods causes not only the peak flux position to move by approximately the same amount, but also causes a small change in the magnitude of the flux. Detailed neutronic calculations are now in progress to determine the composition of core pieces 3 and 4, to be used from approximately 5 to 20 dpa. Also, additional calculations will be made to recheck the composition of the first two core pieces.

2.1.5 Conclusions

Both the engineering design and neutronic calculations are in a stage of refinement. Iterations will be made in both as results become available, but the remaining changes are believed to be minor. The capsule design is expected to be completed by June 1979 and fabrication completed in October.

3. PATH A ALLOY DEVELOPMENT — AUSTENITIC STAINLESS STEELS

Path A Alloys are those alloys generally known as austenitic stainless steels. The most common U.S. designations are AISI types 304, 316, 321, and 347. Primary considerations for selecting this class of alloys for further development are:

1. state-of-the-art production and fabrication technology;
2. extensive data on the effects of neutron irradiation on properties, which show the potential of these alloys for MFR applications;
3. compatibility with proposed coolants and breeding fluids;
4. evidence that for MFR conditions (He, dpa, temperatures) the properties are sensitive to composition and microstructure — thus showing potential for further development.

The strategy for development of these alloys has two related objectives:

1. to determine for a reference alloy the effects of irradiation on those properties most important to fusion reactor design;
2. to develop a path A alloy that is optimized for fusion reactor applications.

The first objective will provide a data base for near-term reactor design and, most important, guidance as to which properties limit performance of this type alloy. Work on the reference alloy will provide direction for the actual alloy development efforts of the second objective. Type 316 stainless steel in the 20%-cold-worked condition appears to be the best choice as a reference alloy. It is the present reference cladding and duct alloy in the breeder reactor programs, and there are extensive data on the unirradiated mechanical properties, effects of heat treatment on properties, structure, and phase stability, and the effects of fast neutron irradiation on properties. The present technology of austenitic stainless steels, including understanding of the physical and mechanical properties and irradiation response, is such that alloy development efforts can move to optimization for use in fusion reactor applications. A Prime Candidate Alloy (PCA) (Fe—16% Ni—14% Cr—2% Mo—2% Mn—0.5% Si—0.2% Ti—0.05% C) has been selected by the ADIP task group. Efforts will now focus on optimizing the composition and microstructure of the PCA leading toward the selection of OPT-A1 (Program Plan designation of first optimized path A alloy).

3.1 THE PRECIPITATION RESPONSE OF 20%-COLD-WORKED TYPE 316 STAINLESS STEEL IRRADIATED IN HFIR AT 370–600°C – P. J. Maziasz (ORNL)

3.1.1 ADIP Tasks

ADIP Tasks I.C.1, Microstructural Stability, and I.C.2, Microstructures and Swelling in Austenitic Alloys.

3.1.2 Objective

The objective of this work is to characterize the precipitation response of 20%-cold-worked type 316 stainless steel to irradiation in HFIR to simultaneously produced high levels of displacements and helium. This response is compared with that in thermally aged and fast-reactor-irradiated material to determine the effect of irradiation and in particular the effect of helium. It is also compared with the response of annealed material exposed to the same environments to determine the effect of cold work.

3.1.3 Summary

The precipitation response of 20%-cold-worked type 316 stainless steel was examined after irradiation in HFIR at 380–600°C, after irradiation in EBR-II at 500°C, and after thermal aging at 600 to 750°C. Eta phase precipitation is a major portion of the response during exposure to all environments. It is not normaliy reported in 20%-cold-worked type 316 stainless steel. Qualitatively eta phase, $M_{23}C_6$, Laves, sigma, and chi appear at similar temperatures after HFIR, EBR-II, or thermal exposure. However, relative amounts of phases, size, and distribution differ some among the various environments. Eta phase is the only carbide-type phase observed after irradiation in HFIR from 380 to 550°C. The large cavities associated with it at 380°C contribute significantly to swelling. Precipitate re-solution and re-precipitation of massive particles of sigma, $M_{23}C_6$, and chi are observed after recrystallization in HFIR.

3.1.4 Progress and Status

3.1.4.1 Experimental

The composition (wt %) of the type 316 stainless steel examined in this work is 18 Cr, 13 Ni, 2.6 Mo, 1.9 Mn, 0.8 Si, 0.05 Ti, 0.05 C, 0.013 P, 0.016 S, 0.05 N, balance Fe. The final steps in specimen preparation from rod involved a 50% reduction in area by cold swaging, annealing for 1 h at 1050°C, 20% further reduction, and finally machining into buttonhead tensile specimens. Details of the irradiation experiments have been published.[1–4] Specimens were irradiated in HFIR (High Flux Isotope Reactor) at temperatures of 370–680°C to neutron fluences producing up to 60 dpa and 4100 at. ppm He. Specimens of the same material were aged at 750°C for 1000 h and 600 and 650°C for 10,000 h. A specimen of the same steel, but cross rolled to a 20% reduction in thickness and fabricated into sheet specimens, was examined after irradiation in EBR-II at 500°C to a neutron exposure producing about 9 dpa. The irradiation temperatures in HFIR were calculated from previously determined nuclear heating values, but new measurements by Grossbeck[5] indicate that the temperatures could be as much as 75°C higher than calculated. For continuity with previous work, the samples will be identified by their calculated temperatures, but the temperature difference will be taken into account in the interpretation of the data. Further temperature measurement in HFIR is in progress.

Disks for transmission electron microscopy (TEM) were thinned by a two-step thinning method developed by DuBose and Stiegler.[6] All specimens were examined with either a JEOL 100-C (120 kV) analytical electron microscope or a Hitachi 1000 (1 MV) conventional transmission electron microscope (CTEM). Several low-order zones were obtained from each precipitate particle examined and compared with the literature[7] to identify the crystal structure. Chemical analysis using energy dispersive x-ray analysis in CTEM was performed on precipitate particles extracted on carbon replicas from aged samples of type 316 stainless steel.

3.1.4.2 Results

The most striking result is the unexpected appearance and dominance of a diamond cubic phase with $a_0 \approx 1.07$ nm in 20%-cold-worked type 316 stainless steel irradiated in HFIR below 600°C. The same type of phase is found in both annealed and 20%-cold-worked type 316 stainless steel after thermal aging at 650°C for 10,000 h. Its crystal structure, lattice parameter and composition after thermal aging are similar to "H-phase" found in other steels by H. Hughes[8] and Tither and Clark.[9] However, as discussed later, this phase should be referred to as eta phase. The experimental results for the various samples observed are presented in Table 3.1.1.

Table 3.1.1. Precipitate Phases Present in 20%-Cold-Worked Type 316 Stainless Steel Exposed to Various Environments

Exposure Temperature (°C)[a]	Exposure (dpa)	Exposure (at. ppm He)	Results[b]
		HFIR Irradiation	
380	48	3300	η in g.b., m
460	54	3800	η in g.b., m; Laves in m
550	43	3000	η in m; Laves in m, g.b.; σ
600–610	57-60	3900–4100	100%recrystallized; massive χ, $M_{23}C_6$, σ; $M_{23}C_6$ in m
580-600	1.5	30	$M_{23}C_6$, Laves, σ
580-600	3.3	85	10–15% recrystallized; $M_{23}C_6$, Laves, σ in deformed; η, Laves, σ in recrystallized
		Thermally Aged	
600	10,000 h		$M_{23}C_6$ in g.b., m; η, Laves in m; massive σ
650	10,000 h		<5% recrystallized; $M_{23}C_6$ in g.b., m; η, Laves in m; massive σ
750	1,000 h		∿20% recrystallized; $M_{23}C_6$, Laves, χ in m deformed; $M_{23}C_6$ (?), Laves, χ, σ in recrystallized
		EBR-II Irradiated	
500	9		$M_{23}C_6$ in g.b.; η in m

[a] Calculated temperatures for HFIR irradiation.

[b] g.b. = grain boundary; m = matrix.

Eta phase is the only intergranular phase observed in 20%-cold-worked type 316 stainless steel after irradiation at 380°C, and it appears together with Laves phase at 460°C [see Fig. 3.1.1(a), (b)]. At 380°C (and to a lesser extent at 460°C), large cavities (∿100 nm in diameter) are attached to eta phase precipitate particles. A total cavity swelling $\Delta v/v_0$ of 2.5% is measured, and 1.0% swelling is due to the large cavities.[3] Discontinuous grain boundary precipitation of eta phase is observed at 380 and 460°C. At 550°C, intragranular eta and Laves phases are observed, and large isolated sigma phase particles are observed at the grain boundaries along with larger than average cavities (40 nm in diameter at grain boundary, 21 nm in the matrix).

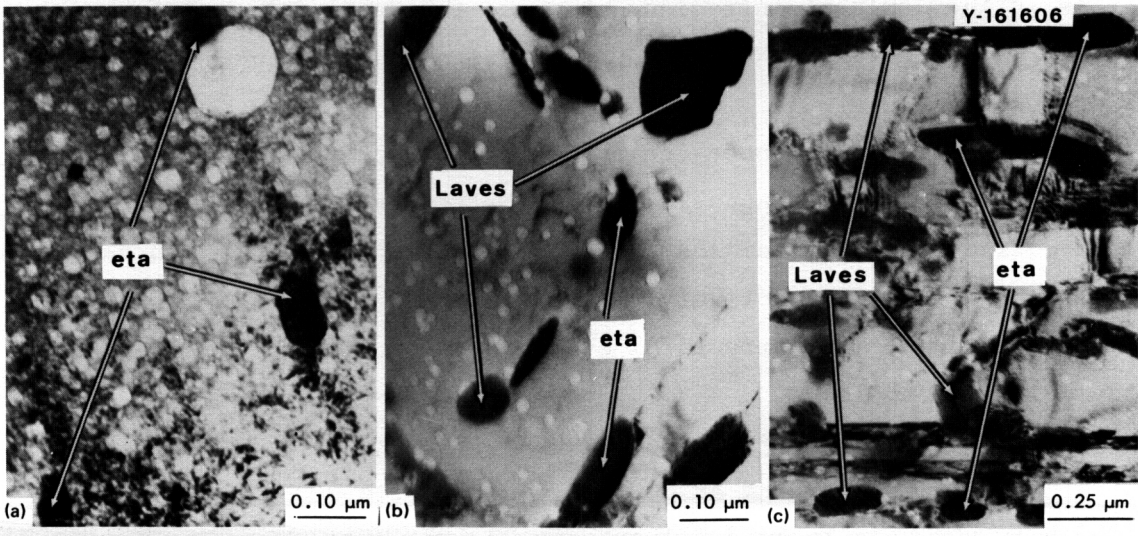

Fig. 3.1.1. Microstructure of 20%-Cold-Worked Type 316 Stainless Steel Irradiated in HFIR to 42–60 dpa and 3000–4100 at. ppm He at (a) 380°C, (b) 460°C, and (c) 550°C.

At 600°C, after irradiation to 60 dpa in HFIR, 20%-cold-worked tyoe 316 stainless steel is compaletely recrystallized. Two samples were observed at these conditions – one contained massive sigma phase and $M_{23}C_6$ (∿5 μm), while the other showed massive sigma and chi phases with smaller $M_{23}C_6$ particles (0.2–0.5 μm) (see Table 3.1.1). The precipitation is quite coarse, but optical metallography indicates the distribution of coarse phases to be reasonably uniform on a

macroscopic scale. After 1.5 dpa at about 600°C, no recrystallization is observed, but partial recrystallization does occur at 3.3 dpa. Laves, some eta, and large sigma phase particles are observed in the recrystallized portion of the material; the unrecrystallized portions of each sample contain $M_{23}C_6$, Laves, and sigma phase particles (see Table 3.1.1). The $M_{23}C_6$, eta, and Laves phase precipitate particles are smaller (100–300 nm) and more finely distributed than the coarse precipitate particles observed after high-fluence irradiation (Fig. 3.1.2). Laves and eta phases are conspicuously absent after high fluence and complete recrystallization.

Gamms prime is not observed in any of the 20%-cold-worked type 316 stainless steel samples irradiated in HFIR, particularly at 380°C where it might be expected from fast reactor irradiation.[••] Indeed, gamma prime is the dominant intragranular phase in annealed type 316 stainless steel irradiated in HFIR at 370°C to neutron fluences producing about 9 dpa.

There is concern about the formation of magnetic phases like ferrite. Billington[11] measured magnetic susceptibility on the TEM disks of 20%-cold-worked type 316 stainless steel irradiated in HFIR at 550 and 600°C to 42 and 60 dpa, respectively. No significant magnetic material was indicated and no microstructural evidence of ferrite formation could be found in any sample.

The precipitation response of 20%-cold-worked type 316 stainless steel after thermal aging at 600 and 650°C for 10,000 h and 750°C for 1000 h is shown in Table 3.1.1 and Fig. 3.1.3. Eta phase is found in significant amounts mixed with $M_{23}C_6$ at 600 and 650°C and is morphologically indistinguishable from $M_{23}C_6$. It is not observed at 750°C. Eta phase is also found in annealed type 316 stainless steel aged 10,000 h at 650°C, and its composition along with $M_{23}C_6$ was determined by quantitative energy dispersive x-ray analysis on individual precipitate particles extracted on a carbon replica. Eta phase contains (wt %) 6 Si, 31 Mo, 29 Cr, 13 Fe, 21 Ni, and ~0 Mn; $M_{23}C_6$ is <1 Si, 16 Mo, 64 Cr, 13 Fe, 5 Ni, <0.5 Mn. The eta phase and $M_{23}C_6$ compositions in 20%-cold-worked type 316 stainless steel after the same aging treatment are similar to those reported above.

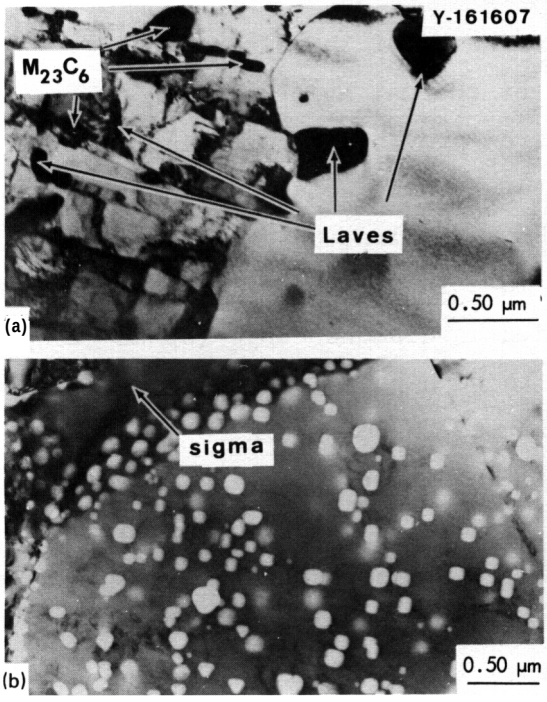

Fig. 3.1.2. Microstructure of 20%-Cold-Worked Type 316 Stainless Steel Irradiated in HFIR at about 600°C to (a) 3.3 dpa and 85 at. ppm He (partially recrystallized) and (b) 60 dpa and 4070 at. ppm He (completely recrystallized).

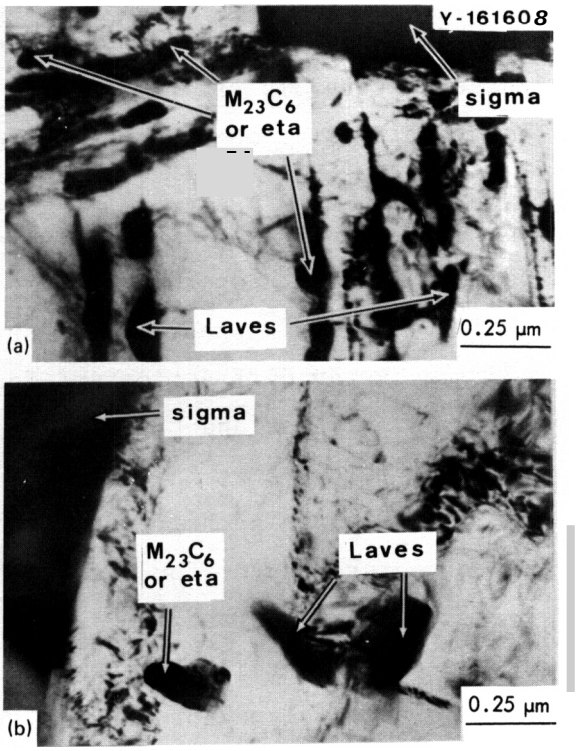

Fig. 3.1.3. Microstructure of 20%-Cold-Worked Type 316 Stainless Steel, Thermally Aged at (a) 600°C for 10,000 h and (b) 650°C for 10,000 h.

Laves phase, $M_{23}C_6$, and massive sigma phase particles are observed in all thermally aged samples. Chi phase is observed only after 1000 h at 750°C. As shown in Fig. 3.1.3, the precipitate density decreases and the size coarsens with increasing temperature. The relative amount of carbide to intermetallic Laves phase tends to decrease as the temperature increases. Slight (<5 vol %) recrystallization is observed at 650°C after 10,000 h and considerable recrystallization (~20%) is observed after 1000 h at 750°C.

Finally, 20%-cold-worked type 316 stainless steel has been examined after EBR-II irradiation at 500°C to neutron fluences producing 9 dpa. Small blocky eta phase particles are observed intragranularly, with $M_{23}C_6$ particles at the grain boundaries.

3.1.4.3 Discussion

The widespread appearance and dominance of the diamond cubic phase in type 316 stainless steel after thermal aging or HFIR or fast reactor irradiation were unexpected from previous reports in the literature.[3,4,10,12–16] However, after thermal aging, a similar phase has been observed in other steels. Hughes[8] first observed a phase he termed "H phase" together with $M_{23}C_6$ in a 12 Cr-4 Ni–0.1 C steel (3% Mn, 3% Si, 1% V). "H phase" was identified as diamond cubic (space group $Fd3m$) by x-ray diffraction and found to be high in silicon by chemical analysis. Tither and Clark[9] also observed "H phase" in 18 Cr–15 Ni–0.03 C steel (4.5 wt % Si, 1 wt % Mn), but incorrectly identified it as fcc ($Fm3m$) when their published x-ray data indicated diamond cubic. The structure factor for diamond cubic ($Fd3m$) crystal structure predicts systematic absences of (200), (420), etc.[7] Tither and Clark analyzed "H phase" to contain (in atomic percent) 11 Si, 8 Fe, 44 Cr, and 37 Ni, but did not analyze for carbon. They assumed it was $M_{23}Si_6$, while Hughes had assumed an MSi_x compound with $X > 1$. Hughes, however, did not directly analyze the "H phase" for carbon either. It is unclear whether it is a carbide or a silicide. This phase should not be confused with a class of carbon- or nitrogen-containing compounds having a hexagonal close-packed structure ($c/a = 4.9$), also termed H phase.[17]

The appearance of a diamond cubic "H phase" makes suspect the observations of "M_6C," also diamond cubic, in other work[4] on type 316 stainless steel. A review of eta phase by Stadlemaier[17] indicates that an eta-carbide structure proposed by Westgren[18] could well encompass $M_3M'_3X$, $M_6M'_6X$ (X is C, N, or O), or $M_2M'_3Si$-type phases with lattice parameters ranging from 1.07 to 1.22 nm, depending upon phase composition. The composition and stoichiometry of the phase in turn depend on the composition of the matrix.[17–20] Both "H phase" and "M_6C" fit into the general classification of eta phase, which would be a safe designation until carbon (and/or nitrogen) can be measured to further specify stoichiometry and composition.

The data in the literature[12,13] on 20%-cold-worked type 316 stainless steel show that during thermal aging cold work accelerates the

formation of $M_{23}C_6$, sigma, and chi phases in time relative to annealed material, but not in temperature. After fast reactor irradiation, behavior similar to thermal aging is observed for $M_{23}C_6$, sigma, and chi, but Laves phase formation is shifted to lower temperature in cold-worked relative to annealed material.[10,14–16] A rod-shaped, hexagonal ($c/a = 0.6$), phosphorus-containing phase is observed above 500°C and below 625°C in annealed type 316 stainless steel but not in 20%-cold-worked type 316 stainless steel after fast reactor irradiation.[10,14–16,21–23] Gamma-prime (nominally Ni_3Si) is observed in both annealed and 20%-cold-worked type 316 stainless steel below 480 to 525°C in fast reactors.[10,24] The results reported here on thermally aged or EBR-11-irradiated material are generally consistent with the literature, except that $M_{23}C_6$ and eta phase are found where normally only $M_{23}C_6$ had been reported.

The temperatures at which $M_{23}C_6$, eta, Laves, sigma, and chi phases form during HFIR irradiation are similar to those observed during thermal aging if the calculated irradiation temperatures are adjusted upwards by about 75°C. There are, however, differences in the particle density, size, and relative amounts of the various phases. Figures 3.1.1(c) and 3.1.3(b) indicate that at comparable temperatures the total precipitate particle density is greater after HFIR irradiation than after thermal aging. The carbide appears to be a mix of $M_{23}C_6$ and eta phase after thermal aging but nearly all eta phase after HFIR irradiation up to 550°C (calculated). The trend of decreasing amount of $M_{23}C_6$ and/or eta phase relative to Laves with increasing temperature is the same for both HFIR-irradiated and thermally aged material.

HFIR-irradiated material that has recrystallized contains massive sigma and chi particles much larger than those observed after thermal aging, but the presence of massive $M_{23}C_6$ particles is an anomaly relative to thermal aging. Annealed type 316 stainless steel irradiated in HFIR at 600°C contains only Laves and sigma phases.[4] The re-solution of precipitates following recrystallization is not usually observed in other environments,[12–14] and the absence of Laves is conspicuous. However, the finely distributed phases present before recrystallization (see Table 3.1.1) should result in a different matrix composition than in annealed material. The low dislocation density after recrystallization

presents a new sink structure in the matrix as well, and it is quite possible that prior phases could become unstable with the new matrix conditions. The displacement cascades and enhanced point defect concentrations could also obviously contribute to precipitate re-solution, as well as changes in matrix composition. This type of behavior is disconcerting if preirradiation thermomechanical treatments produce precipitate phases that could become unstable during irradiation.

Comparing HFIR- with EBR-II-irradiated 20%-cold-worked type 316 stainless steel indicates that the carbides and Laves phase form at similar temperature if the calculated temperatures in HFIR are adjusted as mentioned above. Comparing the data on the EBR-II-irradiated material at 500°C (reported in Table 3.1.i) with the literature data, it is possible that the carbide or "carbosilicide" phases reported[10,14-16] are really a mixture of $M_{23}C_6$ and eta phase. In that case, the relative amount of $M_{23}C_6$ and eta phase changes from a mixture of the two during EBR-II irradiation to exclusively eta phase after HFIR irradiation at 550°C (calculated) and below.

The behavior with respect to gamma-prime (Ni_3Si) formation also changes. After HFIR irradiation at 380°C (calculated) and *48* dpa, no gamma prime is observed. Gamma prime would be expected to form in 20%-cold-worked type 316 stainless steel according to fast reactor data,[10,24] even with +75°C adjustment in HFIR irradiation temperatures. The formation of eta phase, with is also high in nickel and silicon, may preclude formation of gamma prime. Indeed, annealed type 316 stainless steel irradiated in HFIR at 370°C (calculated) at about 9 dpa precipitates copious gamma prime intragranularly and no eta phase.

Finally, Porter and Wood[25] observed ferrite formation in 20%-cold-worked type 316 stainless steel irradiated in EBR-II at 550°C to about 4×10^{26} n/m^2 and attribute its formation to depletion of nickel from the matrix. The differences in the precipitation produced in HFIR and in EBR-II indicate that the microchemical evolution of the matrix should not be expected to be the same. The fact that no ferrite is observed after HFIR irradiation clearly supports this. The inclusion of significantly higher simultaneous helium in the damage products for HFIR relative to EBR-II is coincident with these changes in behavior. The

results presented above indicate that helium must be considered as influencing all components of the microstructure, including precipitation.

3.1.5 Conclusions

1. Eta phase is an unexpected and dominant portion of the precipitation response of 20%-cold-worked type 316 stainless steel to thermal aging and EBR-II or HFIR irradiation. It is associated with large cavities after HFIR irradiation at 380°C (calculated).

2. Qualitatively, $M_{23}C_6$, eta, Laves, chi, and sigma phases appear at similar temperatures for HFIR irradiation, EBR-II irradiation, or thermal aging. There are, however, differences in density, particle size, and relative amounts of the various phases.

3. Re-solution of fine precipitate particles of $M_{23}C_6$, eta, and Laves and re-precipitation of massive $M_{23}C_6$, sigma, and chi phase particles follow recrystallization at 600°C (calculated) and above in HFIR.

Measurements need to be made to determine the composition of eta phase formed in HFIR, especially whether or not it contains carbon. This information can then guide both major and minor alloying changes to try and eliminate uncontrolled phase instability.

3.1.6 References

1. F. W. Wiffen and E. E. Bloom, "Effect of High Helium Content on Stainless Steel Swelling," *Nucl. Technol.* 25: 113–23 (January 1975).
2. E. E. Bloom and F. W. Wiffen, "The Effects of Large Concentrations of Helium on the Mechanical Properties of Stainless Steel," *J. Nucl. Mater.* 58(2): 171–84 (November 1975).
3. P. J. Maziasz, F. W. Wiffen, and E. E. Bloom, "Swelling and Microstructure Changes in Type 316 Stainless Steel Irradiated Under Simulated CTR Conditions," *Radiation Effects and Tritium Technology for Fusion Reactors,* CONF-750989, Vol. I, pp. 259–88 (March 1976).
4. P. J. Maziasz, "Precipitation Response of Austenitic Stainless Steel to Simulated Fusion Reactor Irradiation," paper presented at AIME Meeting, Denver, Colorado, February 26–March 2, 1978, to be published in the proceedings of symposium on Metal Physics of Stainless Steel.

5. Private communication, M. L. Grossbeck, ORNL.
6. C.K.H. DuBose and J. O. Stiegler, *Semiautomatic Preparation of Specimens for Transmission Electron Microscopy,* ORNL-4066 (February 1967).
7. K. W. Andrews, D. J. Dyson, and S. R. Koewn, *Interpretation of Electron Diffraction Patterns,* 2nd ed., Adam Hilger, Ltd., London, 1971.
8. H. Hughes, *Nature* 183: 1543 (1959).
9. S. J. Tither and B. R. Clark, *Met. Sci. J. 4:* 118 (1970).
10. H. R. Brager and F. A. Garner, *J. Nucl. Mater.* 73: 9 (1978).
11. D. S. Billington, Oak Ridge National Laboratory, unpublished data.
12. B. Weiss and R. Stickler, *Metall. Trans.* 3: 851 (1972).
13. J. E. Spruiell et al., *Metall. Trans.* 4: 1533 (1973).
14. E. E. Bloom and J. O. Stiegler, "Effect of Irradiation on the Microstructure and Creep-Rupture Properties of Type 316 Stainless Steel," pp. 360-80 in *Effects of Radiation on Substructures and Mechanical Properties of Metals and Alloys, Am. Soc. Test. Mater. Spec. Tech. Publ.* 529, American Society for Testing and Materials, Philadelphia, September 1973.
15. H. R. Brager, *J. Nucl. Mater.* 57: 103 (1975).
16. J. I. Bramman et al., "Void Swelling and Microstructural Changes in Fuel Pin Cladding and Unstressed Specimens Irradiated in DFR," pp. 479-505 in *Radiation Effects in Breeder Reactor Structural Materials,* The Metallurgical Society of AIME, New York, 1977.
17. H. H. Stadelmaier, *Developments in the Structural Chemistry of Alloy Phases,* Plenum Press, 1969, p. 141.
18. A. Westgren, *Jernkont. Ann.* 117: 1 (1933).
19. J. M. Leitnaker, R. L. Klueh, and W. R. Laing, "The Composition of Eta Carbide Phase in 2 1/4 Cr-1 Mo Steel," *Metall. Trans.* 6A: 1949-55 (October 1975).
20. J. M. Leitnaker, G. A. Potter, D. J. Bradley, J. C. Franklin, and W. R. Laing, "The Composition of Eta Carbide in Hastelloy N After Aging 10,000 hr at 815°C," *MetaZZ. Trans.* 9A: 397-400 (March 1978).
21. H. R. Brager and J. L. Straalsund, *J. Nucl. Mater.* 46: 134 (1973).
22. P. J. Barton et al., *J. Nucl. Mater.* 67: 181 (1977).

23. J. Bentley, to be published in *Journal* of *Nuclear Materials* in the proceedings of a Workshop on Solute Segregation and Phase Instability, November 1–3, 1978, Gatlinburg, Tenn.
24. C. Cawthorne and C. Brown, *J. Nucl. Mater. 66:* 201 (1977).
25. D. L. Porter and E. L. Wood, to be published in *Journal* of *Nuclear Materials* in the proceedings of a Workshop on Solute Segregation and Phase Instability, November 1–3, 1978, Gatlinburg, Tenn.

3.2 MICROSTRUCTURAL CHARACTERIZATION OF AS-RECEIVED PRIME CANDIDATE ALLOY AND EXAMINATION OF MICROSTRUCTURAL, SENSITIVITY TO FABRICATION AND PROCESSING VARIABLES — P. J. Maziasz and T. K. Roche (ORNL)

3.2.1 ADIP Task

ADIP Tasks I.A.5, Fabrication Analysis; and I.D.1, Materials Stockpile for DMFE Programs.

3.2.2 Objective

The objective of this work was to examine the microstructure of the as-received Path A PCA to determine how to develop various particle sizes and distributions of TiC. Initial results prompted our investigation of the fabrication variable sensitivity of the microstructural response, to determine fabrication routes that avoid macro- and microscopic inhomogeneity of titanium concentration and TiC distribution.

3.2.3 Summary

Several finished product forms of the Path A Prime Candidate Alloy have been received from Teledyne Allvac and examined to characterize its homogeneity with respect to dissolved titanium and TiC. Inhomogeneities were found in material removed at an intermediate stage of fabrication and worse in finished plate. Several fabrication experiments were conducted on the intermediate material, both as received and after homogenization at 1200°C for 24 h. Some sensitivity to cooling rate after homogenization was found in the TiC distribution and the resulting amount of recrystallization, but the greatest microstructural sensitivity was found when unhomogenized and homogenized material were compared. Severe macro and micro inhomogeneity develops during the fabrication sequences when the material is not properly homogenized initially. Cold work followed by recrystallization causes many more stringers than hot working. The final product form, in particular the 13-mm-thick plate, had reasonably uniform grain size but inhomogeneous distributions of coarse TiC particles from grain to grain. Some clusters of grains had many particles and about 1 wt % Ti, while other groups of grains had no TiC and about 0.35 wt % Ti. The as-received 13-mm plate had

clearly unacceptable homogeneity and must be homogenized before pre-irradiation treatments to vary microstructure. Fabrication processes need to be developed so that gross inhomogeneity in titanium and TiC does not hamper alloy development and microstructural variation.

3.2.4 Progress and Status

Titanium- or niobium-modified austenitic steels are considered stabilized' only after a heat treatment at 870 to 900°C to precipitate MC-type carbide. This is supposed to prevent formation of $M_{23}C_6$, eta, and other phases that can degrade properties. This production of a uniform, fine precipitate of MC-type carbide is also one of the principles for protection against the effects of helium.[2,3] The ADIP Program hopes to employ it in optimizing austenitic stainless steels for fusion applications. The freedom to pursue preirradiation microstructural design depends on composition and the microstructure produced during the preceding fabrication sequences. Severe microstructural and chemical heterogeneity introduced into the structure by fabrication can eliminate or impair this freedom.

Stringering of the carbide precipitate during hot-forming has been observed by others,[4-6] and the consequences of such inhomogeneity have been considered in detail by Braski and Leitnaker.[6] Homogeneity problems due to titanium carbide and nitride have also been recently observed[7] in an alloy similar to ours. The resultant phase stability of a modified austenitic steel during either thermal aging or irradiation depends intimately on the uniformity and distribution of MC-type precipitates.[6-9]

3.2.4.1 Update on Procurement

Plate and bar products processed from a 1.4-Mg (3000-lb) heat of Path A Prime Candidate Alloy by Teledyne Allvac have been received. Results of the vendor's chemical analysis of the finished products are presented in Table 3.2.1. Details of the processing of this material were given previously.[**] The 13-mm-thick (1/2-in.) plate, 13-mm-diam (1/2-in.) bar, and 33-mm-diam (15/16-in.) bar were ultrasonically inspected by the vendor and determined to be of good quality with respect to internal flaws.

Table 3.2.1. Vendor's Chemical Analysis and ORNL Analysis of Products from 1.4-Mg (3000-lb) Heat of Path A Prime Candidate Alloy[a]

Element	Content, wt %				
	0.1-m-diam (4-in.) Bar	33-mm-diam (1 5/16-in.) Bar	13-mm-diam (1/2-in.) Bar	13-mm (1/2-in.) Plate	
				Vendor	ORNL
Ni	16.59	16.63	16.55	15.91	16.2
Cr	14.27	14.31	14.33	13.98	14.0
Mo	1.96	1.95	1.97	1.93	2.3
Ti	0.32	0.31	0.22	0.30	0.24
Mn	1.62	1.83	1.78	1.66	1.8
Si	0.53	0.52	0.51	0.50	0.42
C	0.046	0.048	0.043	0.046	0.047
N	0.008	0.008	0.008	0.008	0.0088
Al	0.05	0.05	0.05	0.05	0.03
As	<0.01	<0.01	<0.01	<0.01	0.01
B	0.001	0.001	0.001	<0.001	0.0005
co	0.04	0.04	0.04	0.04	0.02
Nb	0.02	0.02	0.02	0.02	<0.05
cu	0.02	0.02	0.02	0.02	0.05
P	0.014	0.014	0.015	0.014	0.0087
S	0.002	0.002	0.001	0.001	0.0027
Ta	0.01	0.01	<0.01	0.01	<0.001
V	0.04	0.04	0.04	0.04	0.02
Zr	<0.03	0.02	0.02	0.02	<0.0003

[a] Vendor's analysis unless otherwise indicated. Balance iron.

A 13-mm-thick (1/2-in.) slice of 0.13-m (5-in.) round cornered square (RCS) bar was also obtained from the vendor. (This is an intermediate product form in the fabrication sequence.) Production of the RCS bar had included homogenization for 24 h at 1150°C of the 0.30-m-diam (12-in.) VAR ingot and hot rolling in the temperature range 1150 to 925°C to 0.13 m RCS bar, then annealing at 1038°C for 1 h followed by air cooling. The slice was taken from near center of the bar, corresponding to near center of the original ingot. A flow chart of the fabrication sequence is shown in Fig. 3.2.1.

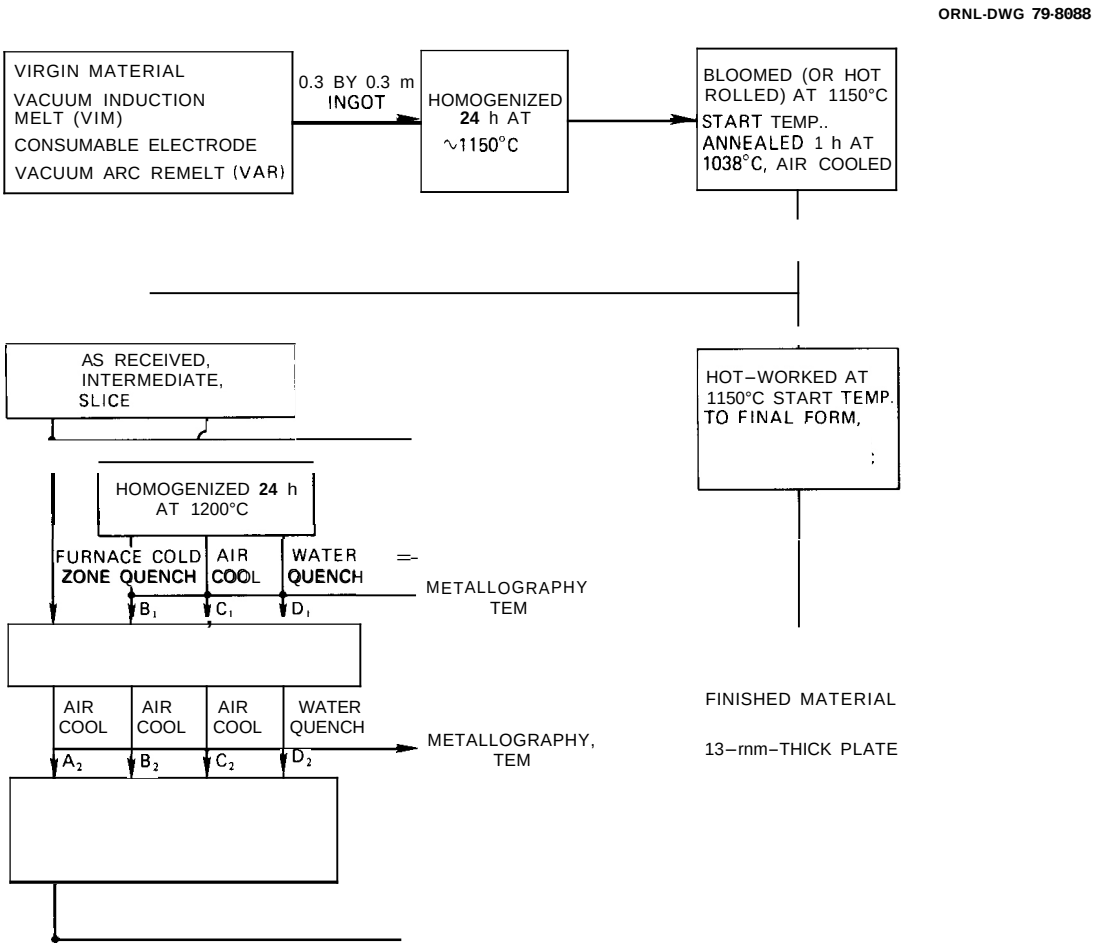

3.2.4.2 Experimental Procedure

Examination of the alloy consisted primarily of metallography, transmission electron microscopy (TEM), and energy dispersive x-ray analytical electron microscopy (EDX/AEM). The as-received finished product forms were examined by the above techniques. Bulk quantitative chemical analyses have been performed, and the results are shown in Table **3.2.1.** The intermediate product form was investigated to check the homogeneity at that step and to compare its microstructure with that present in the final product form. Initial results prompted a homogenization treatment investigation. Since the final product form from the vendor must be further fabricated for specimen stock, several experimental fabrication sequences were examined to determine the

microstructural sensitivity to fabrication variables. The experimental fabrication sequences are summarized in Fig. 3.2.1. Metallographic and TEM-AEM check points are indicated.

3.2.4.3 Results and Discussion on Intermediate Product, RCS Bar

This material was examined to check the homogeneity after homogenization and blooming (see Fig. 3.2.1). The metallographic and TEM microstructures of as-received material are shown in Fig. 3.2.2 and 3.2.3, respectively. These figures show two levels of inhomogeneity in this material. Figure 3.2.2(a) shows differences in grain size and recrystallization following the 1 h at 1038°C anneal given after blooming, and Fig. 3.2.2(b) indicates that there are patches of TiC associated with the small-grained or unrecrystallized regions as well

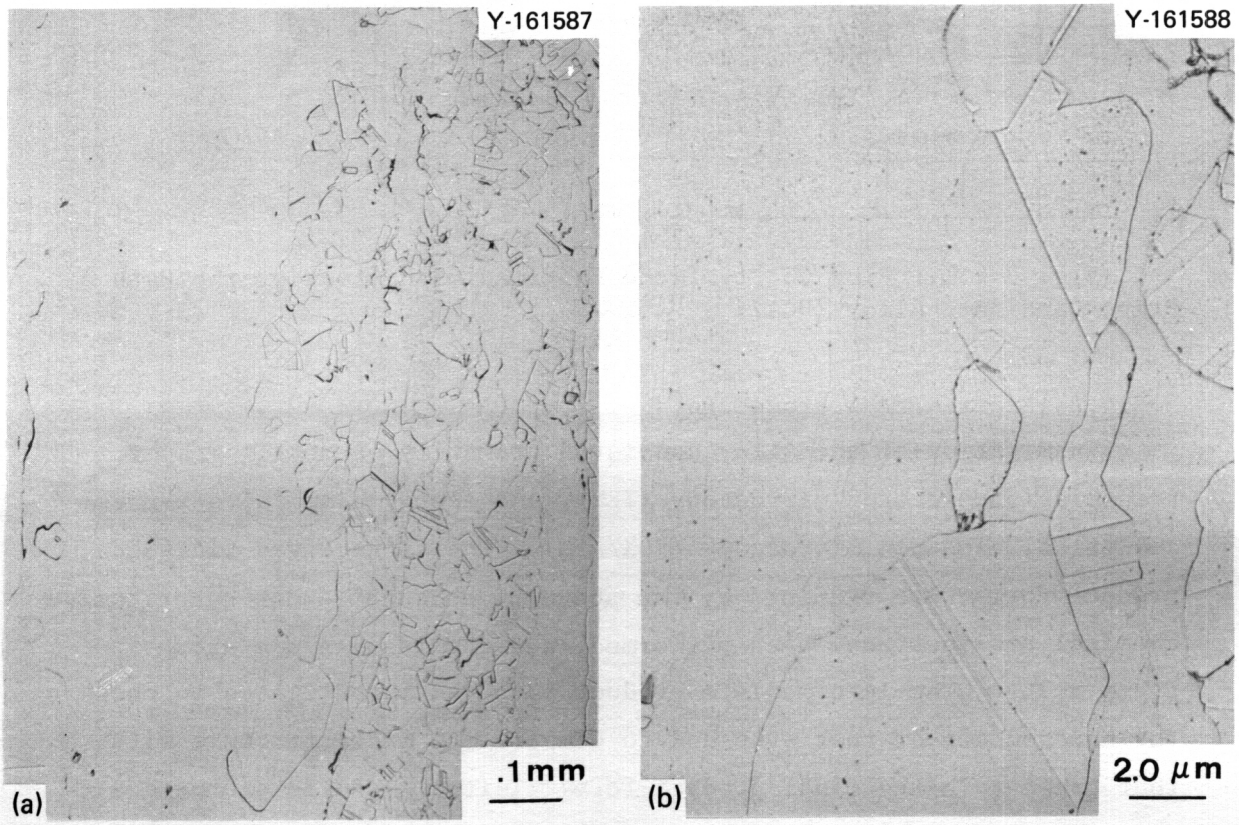

Fig. 3.2.2. As-Received Intermediate RCS Bar. (a) Low magnification showing recrystallized regions with reasonably uniform grain size and unrecrystallized regions. (b) Higher magnification, showing segregation of TiC particles beginning in some areas.

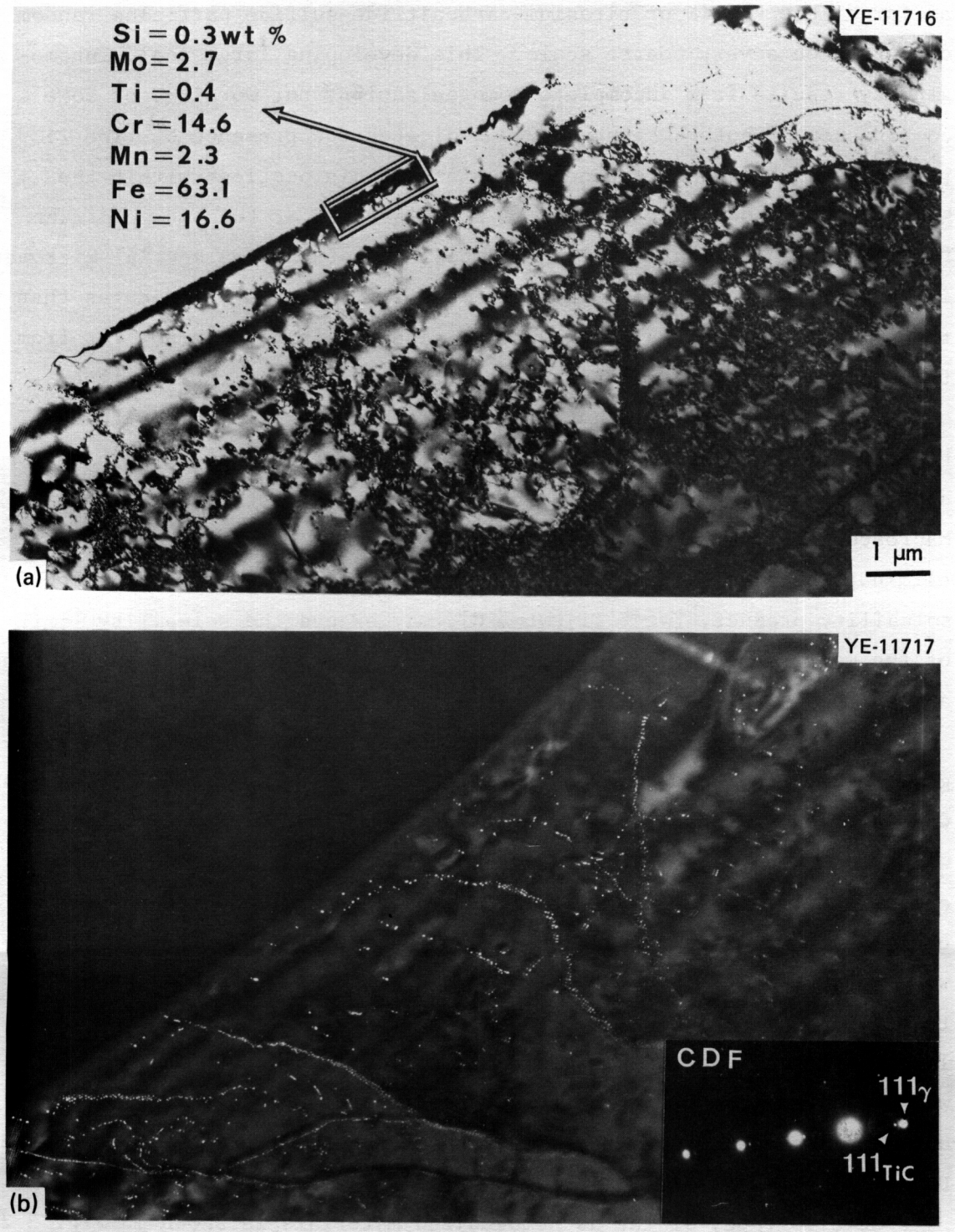

Fig. 3.2.3. The TEM Microstructure of the As-Received Intermediate RCS Bar. (a) Bright field, showing dislocation substructure, also normalized microanalysis of a typical area that includes TiC precipitate. Beam direction close to (011). (b) Dark field with TiC (111) reflection to show fine TiC particles.

as large, blocky TiN or titanium-carbonitride-sulfide particles randomly dispersed on a very coarse scale. This developing large-scale inhomogeneity results from incomplete homogenization, hot working, or some combination of both. Figure 3.2.3 indicates the presence of fine TiC particles clustered at subboundaries and on dislocations within the grain. This shows that the TiC is not dissolved at this stage of the fabrication. Examination of the composition of an area several micrometers in length and about 0.5 μm in width [see Fig. 3.2.3(a)] indicates that the average composition of the matrix plus precipitate is not far from the average composition reported by the vendor. This type of fine-scale inhomogeneity would not be too difficult to eliminate with a heat treatment capable of dissolving TiC because the interparticle spacing is small compared with the diffusion distance of titanium. Macroscopic stringers observed in Fig. 3.2.2 are more difficult to eliminate because in addition to longer diffusion distances, the local solubility product, [wt % Ti][wt % C], may exceed the solubility limit of the matrix, resulting in some TiC in equilibrium with the surrounding austenite.[6]

We tried to homogenize this as-received material and then investigate the microstructure response to fabrication variables. The material was annealed in argon for 1 h at 1150, 1200, 1250, or 1300°C and then water quenched. Fine TiC dissolved at all temperatures, and a homogenization treatment of 24 h at 1200°C was selected. Specimens were cooled either in the furnace cold zone (Path B), in air (Path C), or by water quenching (Path D) after the homogenization. (Path A was as received.) Attention will be focused on Paths C and D, and the base line is Path A. In the discussion to follow, subscripts (see Fig. 3.2.1) will be added to the path letters to designate successive treatments after these paths; the materials at this stage are thus A_1, B_1, C_1, and D_1.

Metallography of the as homogenized materials is shown in Fig. 3.2.4 and TEM microstructures of C_1 and D_1 are shown in Fig. 3.2.5. Both results indicate that most of the TiC, both fine and macro stringers, has dissolved. Occasional coarse, blocky TiN and/or titanium-carbonitride-sulfide particles are still present. Also, Fig. 3.2.5(b) show6 occasional

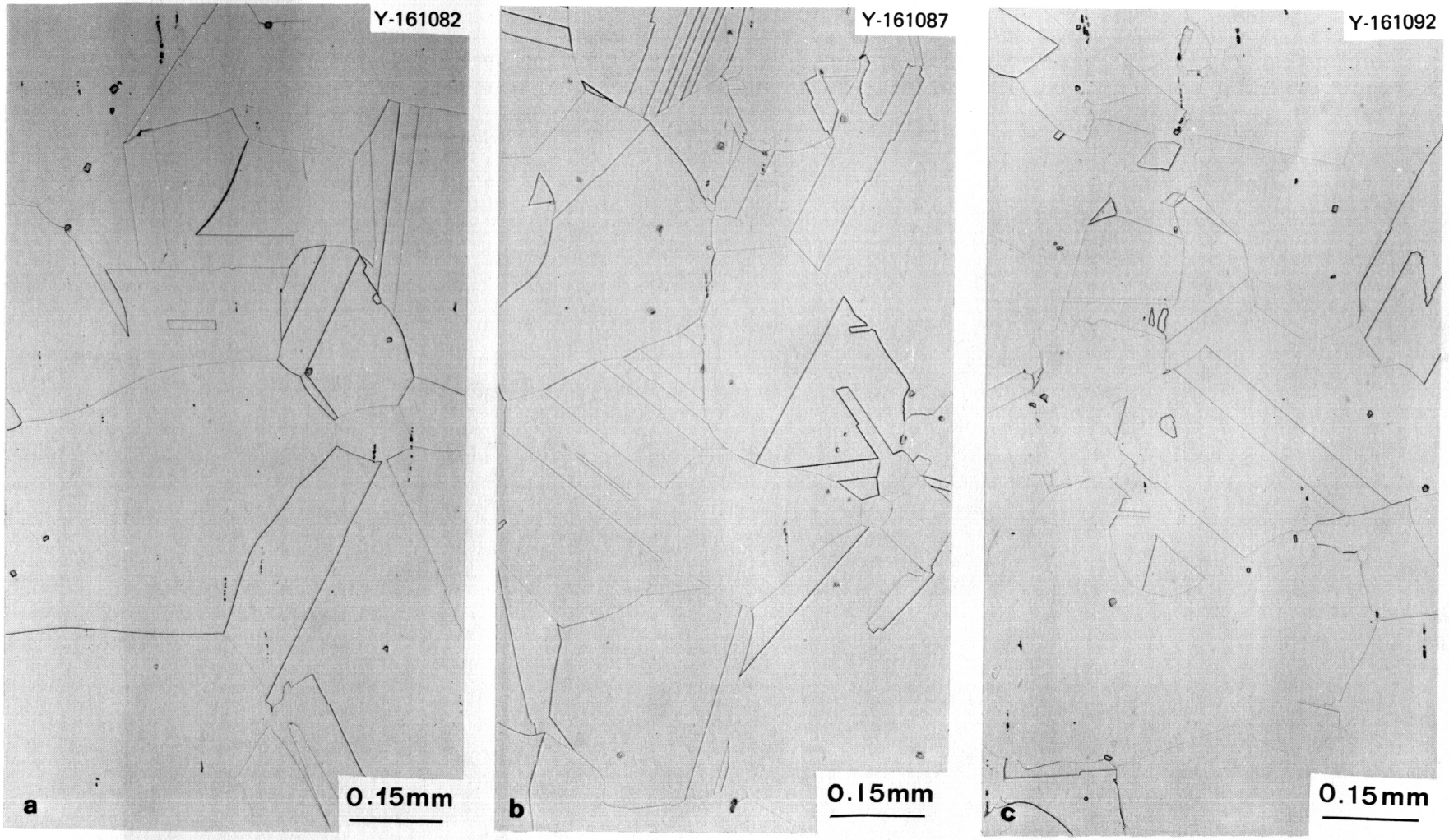

Fig. 3.2.4. Metallography of As-Received Intermediate RCS Bar After Homogenization at 1200°C for 24 h Followed by Three Cooling Methods. (a) Path B_1, quenched in the furnace cold zone. (b) Path C_1, air cooled. (c) Path D_1, water quenched.

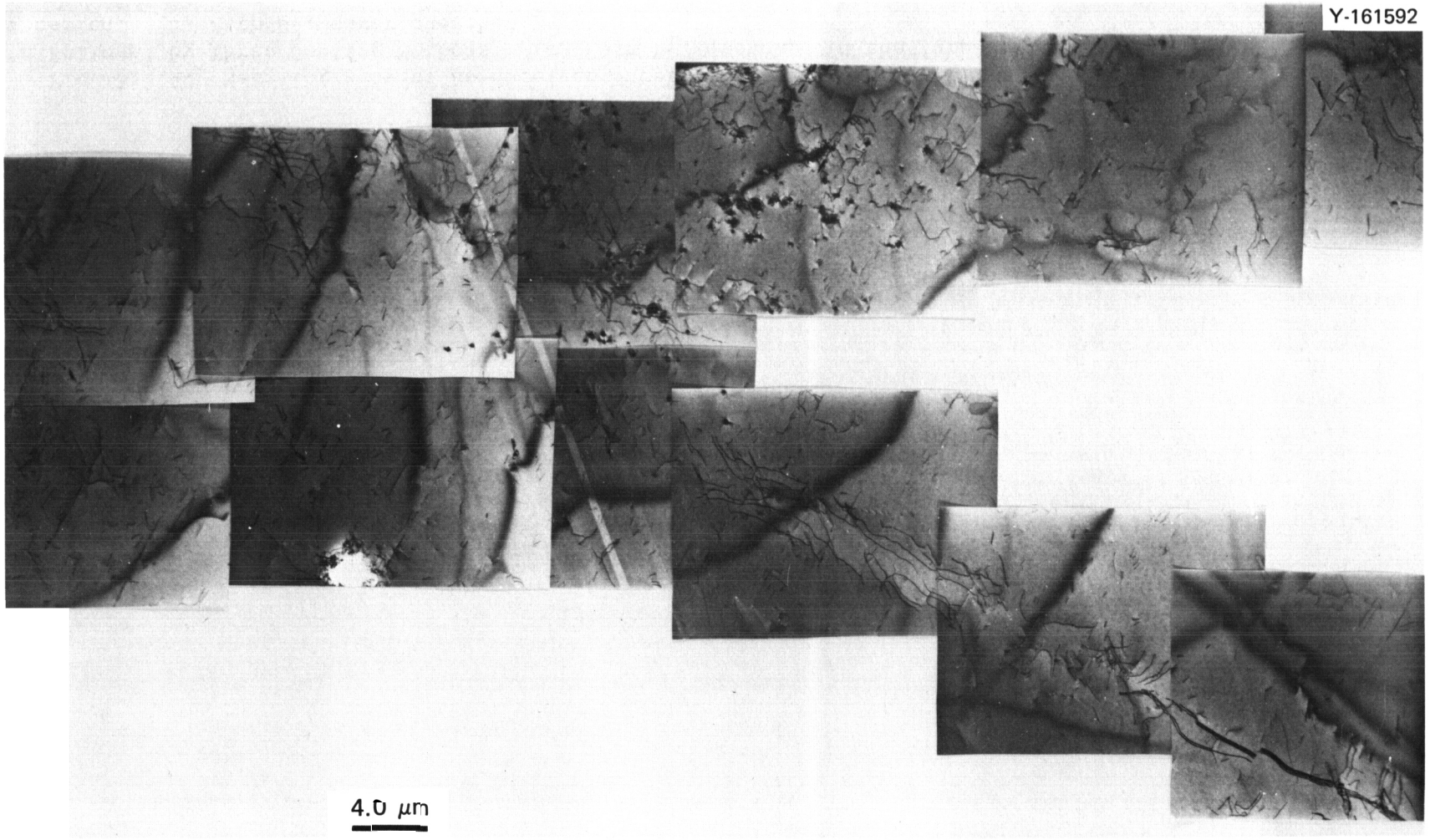

Fig. 3.2.5. The TEM Microstructure of the As-Received Intermediate RCS Bar After Homogenization at 1200°C for 24 h and then Water Quenching (Path D_1). The air-cooled material (Path C_1) is similar.

small TiC particles that indicate that some small areas may still be inhomogeneous with respect to TiC and/or titanium distribution. However, both macroscopically and microscopically, the situation is dramatically improved over the as-received material shown in Figs. 3.2.2 and 3.2.3. There appears to be no dramatic differences immediately after homogenization in the samples that were water quenched (Path D) compared with the air-cooled samples (Path C).

The metallography of Paths A_2, C_2, and D_2 following hot rolling at 1050°C and annealing for 15 min at 1050°C are shown in Fig. 3.2.6, and corresponding TEMs are shown in Figs. 3.2.7 and 3.2.8. These results indicate that Path A_2 has fully recrystallized but Paths C_2 and D_2 have not. Both have a significant portion of unrecrystallized material, but Path C_2 has more than Path D_2. The area fraction of recrystallization in Path C_2 appears to be about 50%. For unrecrystallized material to exist after 15 min at 1050°C is anomalous compared with standard type 316 stainless steel, which can recrystallize in minutes at about 800°C. The TEM microstructures (Figs. 3.2.7 and 3.2.8) clearly indicate gross differences in dislocation and TiC structure for the three paths. None of the samples showed gross stringering of TiC; however, paths A_2 and D_2 show microscopic inhomogeneity of TiC distribution. Path A_2 showed complete recrystallization [Fig. 3.2.6(a)] and little or no fine TiC precipitation within the grains. Paths C_2 and D_2 both show regions of fine TiC associated with the dislocations, Fig. 3.2.9. Such an association is commonly observed between dislocations and fine TiC particles[8,9,11] and is a consequence of dislocations aiding nucleation[12] and the particles in turn trapping the dislocations.[13,14] This association of the fine TiC and dislocations correlates with the unrecrystallized portions of the microstructure shown in Fig. 3.2.6(a). This also indicates that the reason for the anomalous recrystallization behavior is the dislocation trapping by finely dispersed TiC.

A comparison of recrystallized regions for points C_2 and D_2 (Fig. 3.2.8) indicates that TiC particles in these regions differ considerably in size and spacial distribution. Fine TiC is present in recrystallized grains in the C_2 sample, which was air-cooled, and coarser

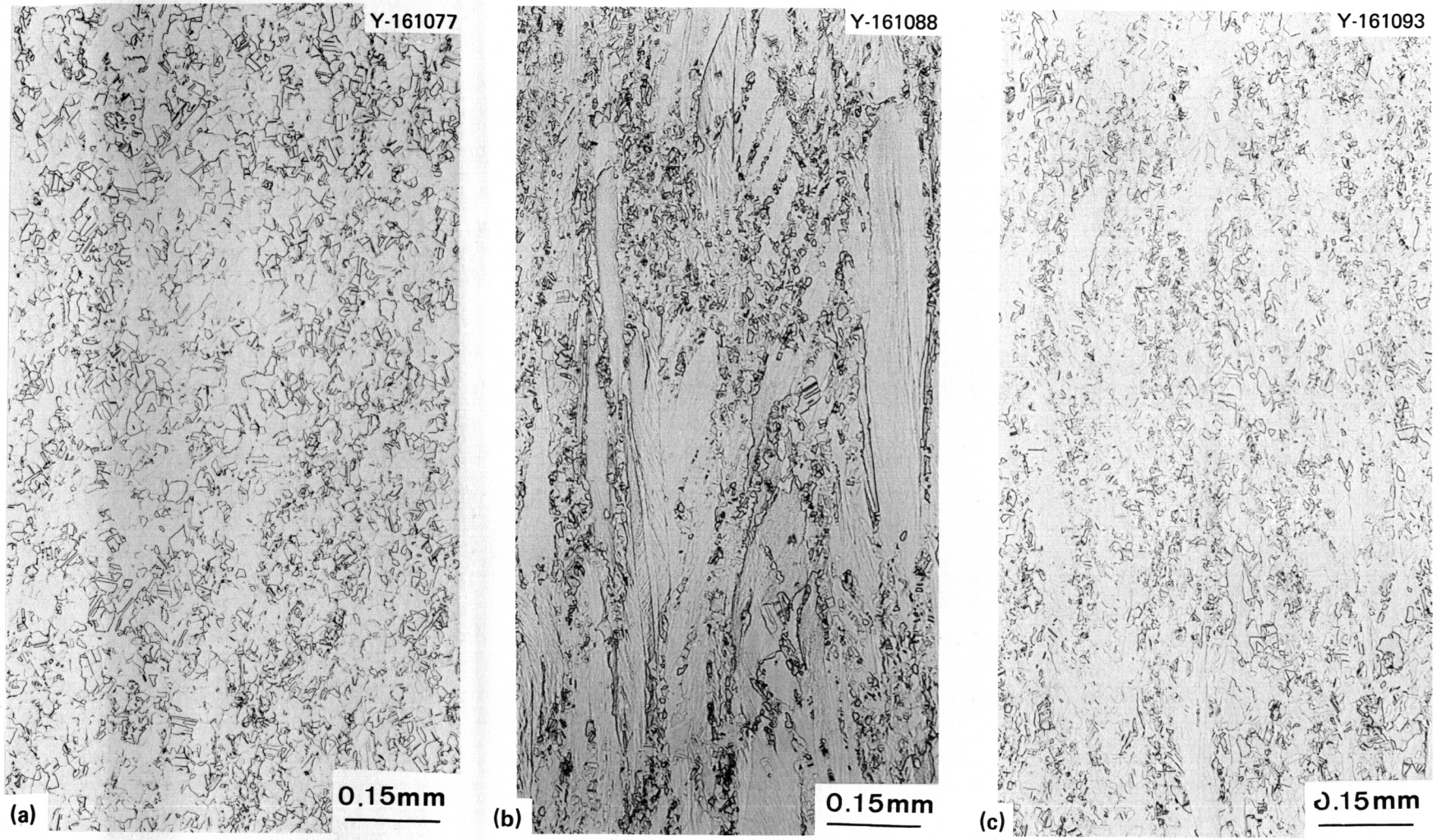

Fig. 3.2.6. Metallography of the As-Received Intermediate RCS Bar After Hot Working and Annealing for 15 min at 1050°C. (a) A_2. (b) C_2. (c) D_2. Note the differences in recrystallization from sample to sample.

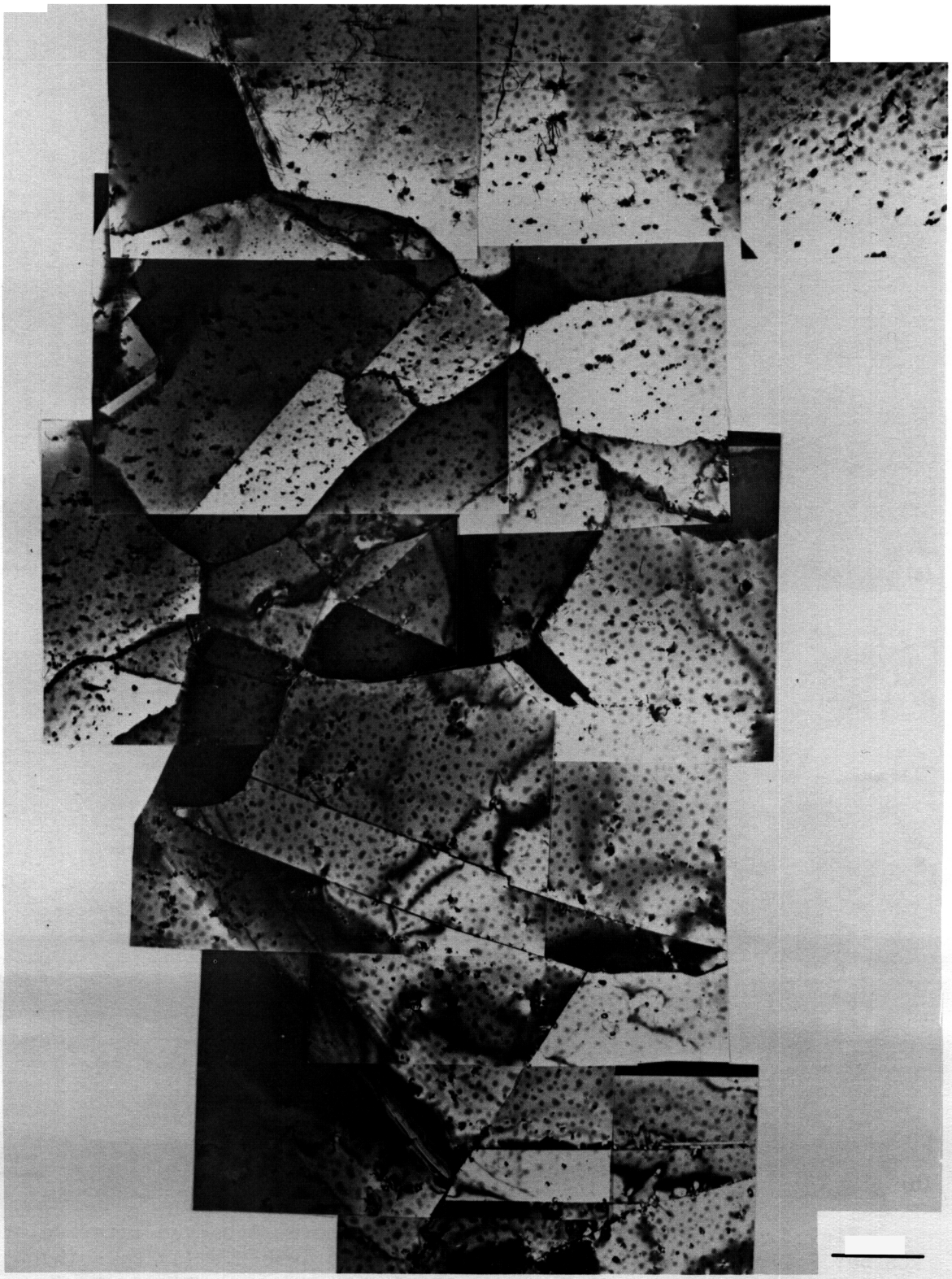

Fig. 3.2.7. The TEM Microstructure of the As-Receive[illegible]

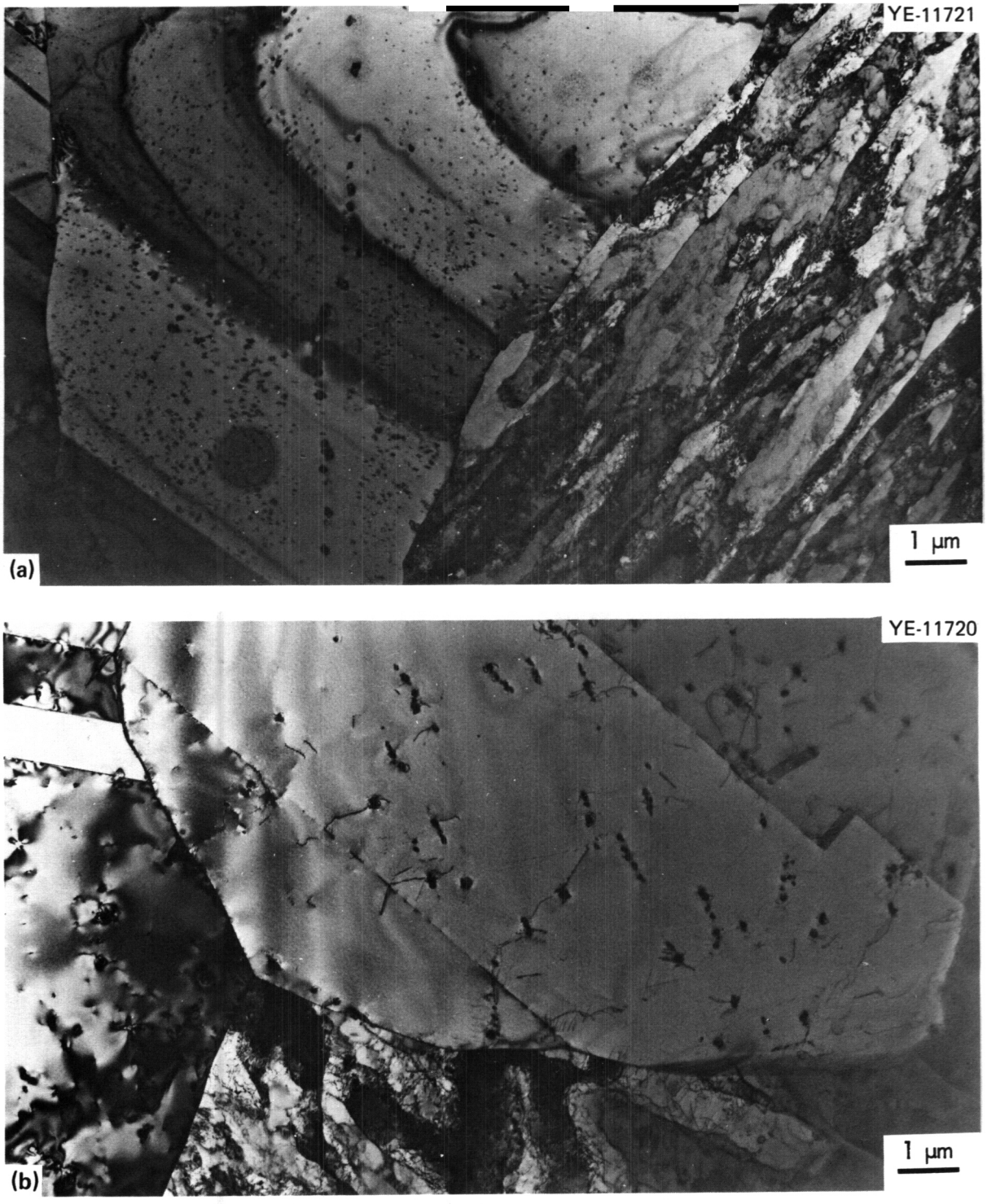

Fig. 3.2.8. The TEM Microstructure of the As-Received Intermediate RCS Bar Following Hot-Rolling and Annealing at 1050°C. (a) C_2. (b) D_2. Note the difference in TiC distribution in the recrystallized portions of (a) and (b).

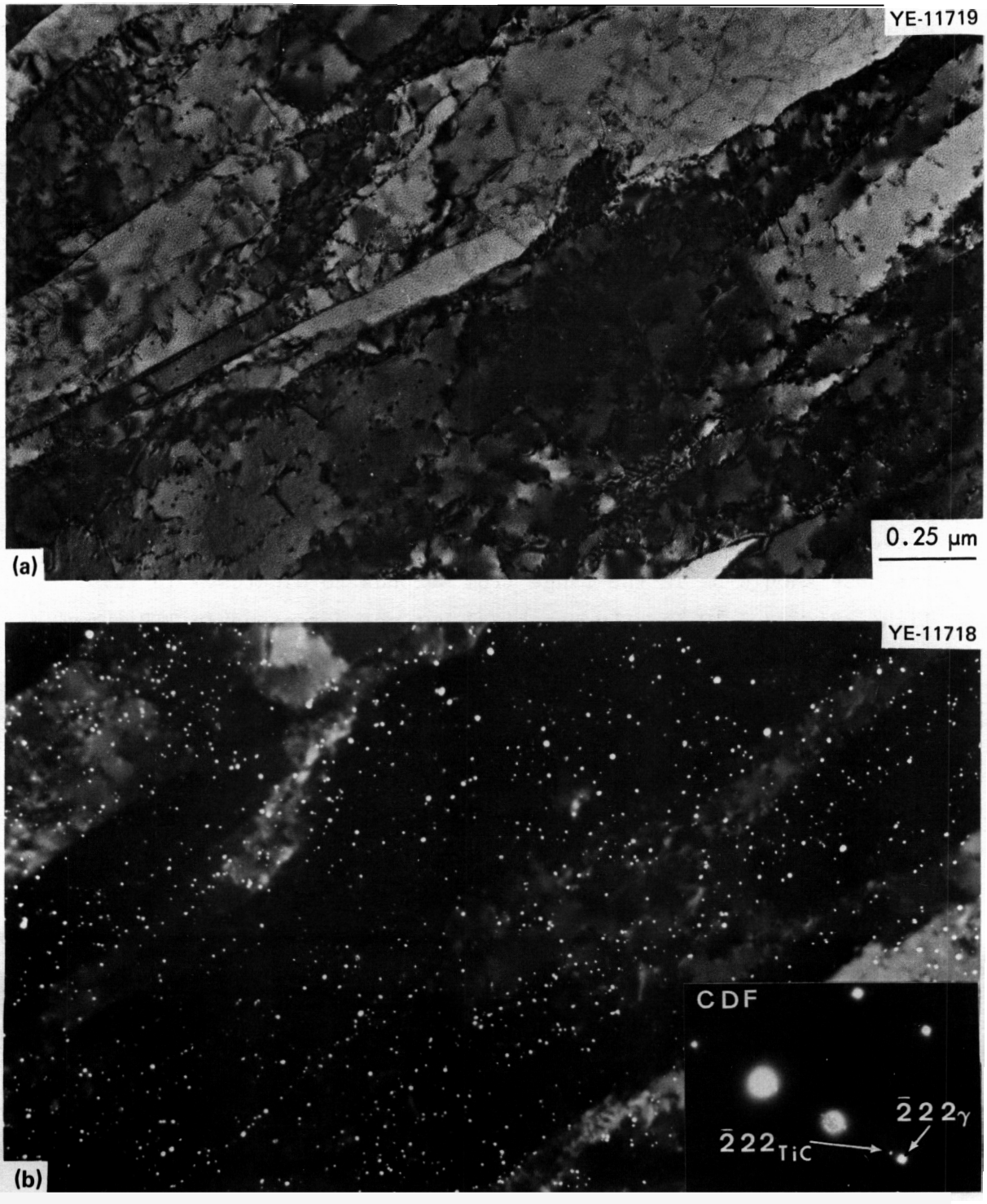

Fig. **3.2.9.** The TEM Microstructure of the As-Received Intermediate RCS Bar, C_2. (a) Bright field of typical unrecrystallized region. (b) Dark field of fine TiC using the indicated precipitate reflection. Beam direction is close to [123].

stringered TiC appears in the recrystallized grains of the water-quenched Path D_2 samples. The TiC size and distribution in the recrystallized regions are sensitive to cooling rate.

The presence of more recrystallization in D_2 is easily reconciled with the increased amount of fine TiC in C_2. The question is, why did the difference in cooling rate result in the difference in amount of fine TiC? The recrystallization observed in C_2 and D_2 is the sum of that present after hot-working plus any additional recrystallization that occurred during the 15-min anneal at 1050°C (see Fig. 3.2.1). Grot and Spruiell' have done some work on TiC formation in titanium-modified type 316 stainless steel, but data on the actual time-temperature-precipitation (TTP) curve for a homogeneous, solution-treated alloy does not exist. General data[1,8] indicate that the nose of a TiC formation curve should be betwen 700 and 900°C, and that the shortest time at the nose should be in the range from seconds to minutes. In this light, Fig. 3.2.10 is a hypothetical but not unreasonable TTP curve with reasonable continuous cooling curves for water quenching and air cooling superimposed for discussion. Such a nose certainly depends on pretreatment as well.[8] Water quenching should miss the nose of the curve, but air cooling may intersect the curve. The TTP curve generally represents detection of observable TiC particles, which means that nucleation and some growth must have occurred. Even if the C_1 appears solution treated, it is reasonable to assume that considerably more nucleation has occurred than in D_1. Nucleation and growth are certainly slower at 1050°C than at the nose of the curve, since the curve bends as shown in Fig. 3.2.10. Nucleation and growth will have to occur during hot rolling at 1050 to about 925°C. The head start with respect to nucleation and hence fine TiC formation in C_2 could correlate with the larger amount of fine TiC and lesser amount of recrystallization observed in C_2 than in D_2. Nucleation and growth of TiC will also occur during rolling at 1050°C to about 925°C, but this represents a dynamic situation and may affect the fine TiC and recrystallization.

Compare A_2 (see Fig. 3.2.7) with Paths C_2 and D_2 (see Fig. 3.2.8). As noted earlier, A_2 showed about 100% recrystallization with reasonably uniform grain size metallographically after hot working and annealing

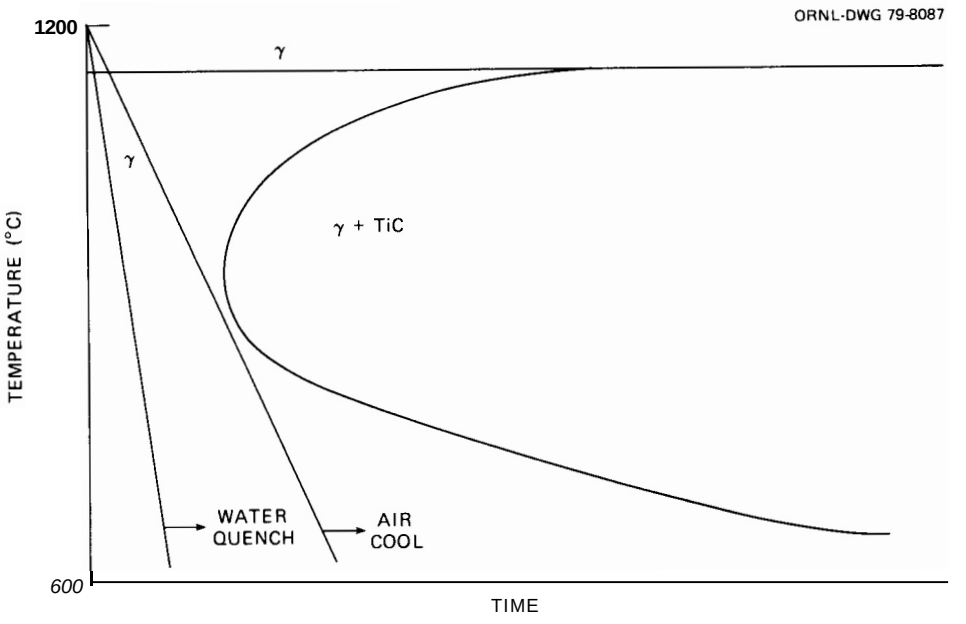

Fig. 3.2.10. A Hypothetical Time–Temperature–Precipitation (TTP) Curve with Generalized Relative Continuous Cooling Curves from Water Quenching and Air Cooling Superimposed.

at 1050°C and no fine TiC microscopically in TEM. This is surprising because fine TiC particles were observed on dislocations and particularly along subboundaries within the grains of the as–received material. This material was not rehomogenized and never saw a temperature higher than 1050°C. Preliminary observations showed that TiC could dissolve at 1150°C but not below, certainly not at 1050°C. After hot working at 1050°C and annealing at 1050°C, Path A has nonuniform, coarse TiC distributions, not only within each grain, but from grain to grain as well. In fact, some grains have almost no TiC particles. Obviously the TiC distribution has coarsened some during the hot working and annealing of the as–received Path A material, and, judging from the lack of fine TiC, most of the TiC seems to have precipitated. The lack of fine TiC is the obvious reason for the complete recrystallization. The question is how did the TiC distribution coarsen? The intragranular structure indicates micro–inhomogeneity of titanium (and carbon), and the grain–to–grain differences indicate that macro–inhomogeneity with respect to titanium is developing. Several possibilities for coarsening are an Oswald–type ripening, in which small

particles dissolve and large particles grow at their expense, or the coalescence of fine particles into larger ones. Both possibilities have their drawbacks. It is hard to imagine even small particles of a stable phase like TiC redissolving, but certainly TiC becomes less stable relative to austenite as the temperature increases simply because at a high enough temperature, TiC dissolves. Coalescence of precipitate particles is also difficult to visualize because it would require the particles to move through the rigid matrix. However, strain energy would certainly be minimized if many small strain centers (as TiC particles are observed to be by strain contrast in TEM) are collected into several larger clusters. Furthermore, hot-working corresponds to high-temperature plastic flow at whatever stress such flow requires, and if the matrix immediately surrounding the particles is moving, certainly the particle moves with it.

Whatever the case, the failure to homogenize Path A has led to a totally different structure with respect to TiC and results in considerably more recrystallization and inhomogeneity with respect to titanium (and carbon) distribution.

Finally, Fig. 3.2.11 shows metallography of Paths A_3, C_3, and D_3 after cold rolling to roughly a 50% reduction in thickness and then annealing in hydrogen for a few minutes at 1050°C. Both C_3 and D_3 have a uniform fine-grained structure, which indicates recrystallization with very little grain growth. On the other hand, A_3 has developed a non-uniform duplex grain size structure with macroscopic stringers of TiC in the fine-grained bands. Clearly gross heterogeneity has developed from the microscopic inhomogeneity observed for A_2 in Figs. 3.2.6 and 3.2.7. Apparently at A_2 all the TiC had precipitated. Clearly, no TiC could have dissolved during cold rolling or during the anneal at 1050°C. Spacial rearrangement of the TiC somehow occurred during the cold working and recrystallization step. Although not understood, it seems that particle motion and coalescence must be considered a possibility. It is also obvious that fabrication of improperly homogenized material simply worsens the situation.

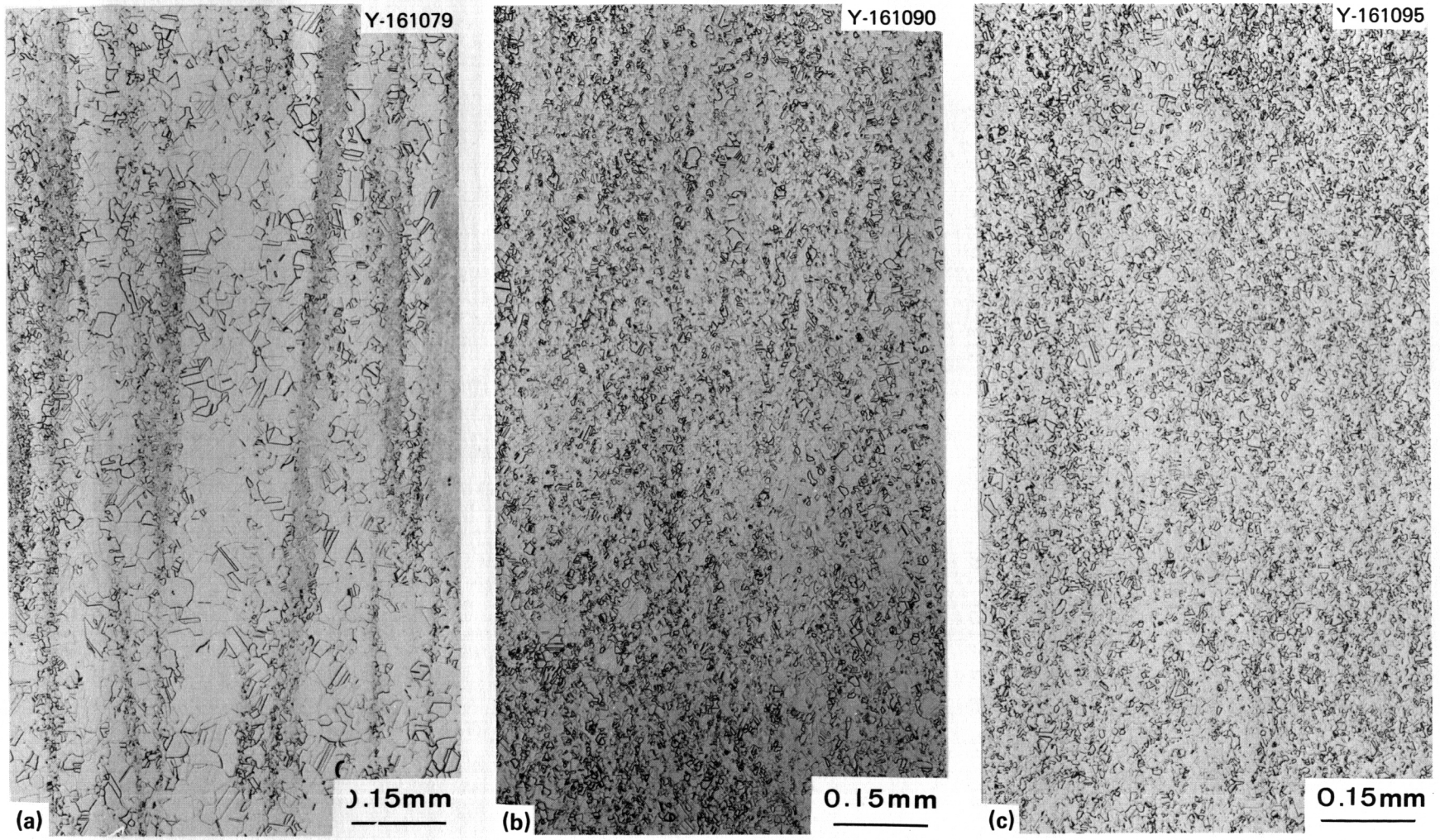

Fig. 3.2.11. Metallography of the As-Received, Intermediate RCS Bar After About 50% Cold Rolling and Annealing for About 5 min at 1050°C. (a) A_3. Note the gross stringering and duplex grain size that has developed. (b) C_3. (c) D_3.

3.2.4.4 Results and Discussion on 13-mm-Thick Plate Stock

Metallography of 13-mm-thick (1/2-in.) plate stock is presented in Fig. 3.2.12 and TEM in Fig. 3.2.13. The grain size is reasonably uniform, and some TiC stringers are observable. The TiC particles are coarse and some grains have many particles, uniformly spaced, while other grains have no observable particles [compare Fig. 3.2.11(a) and (b)]. Figure 3.2.14 and Table 3.2.2 show that the concentration of titanium is roughly 0.35 wt % in an area without TiC precipitation and about 1.0 wt % in an area containing TiC precipitate. The concentrations of the alloying elements Cr, Ni, Si, Fe, and Mn are quite uniform when compared on the same scale. The molybdenum concentration is higher in the area with TiC, which is consistent with work by

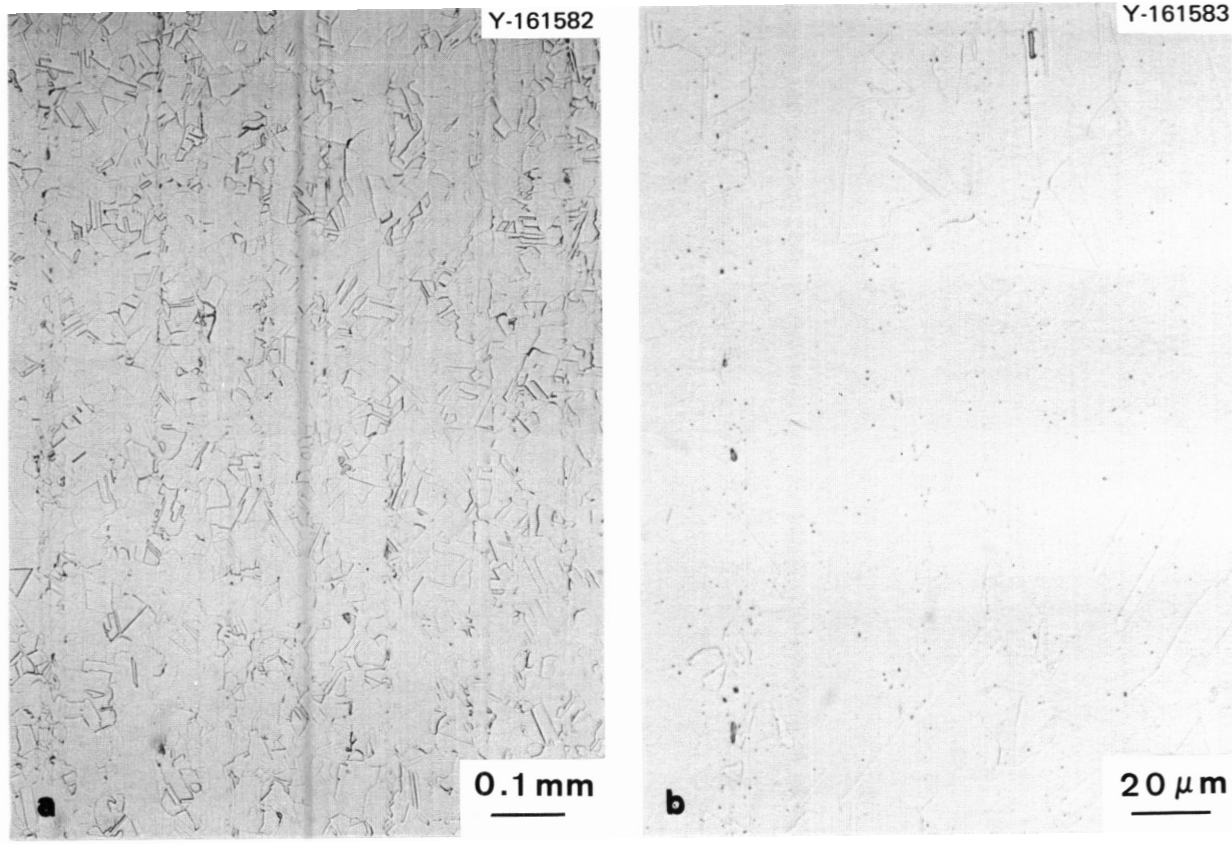

Fig. 3.2.12. Metallography of the As-Received Finished 13-mm-Thick Plate Stock of Path A, PCA. (a) Low magnification shows uniformity in grain size. (b) At high magnification some coarser TiC is not uniformly distributed.

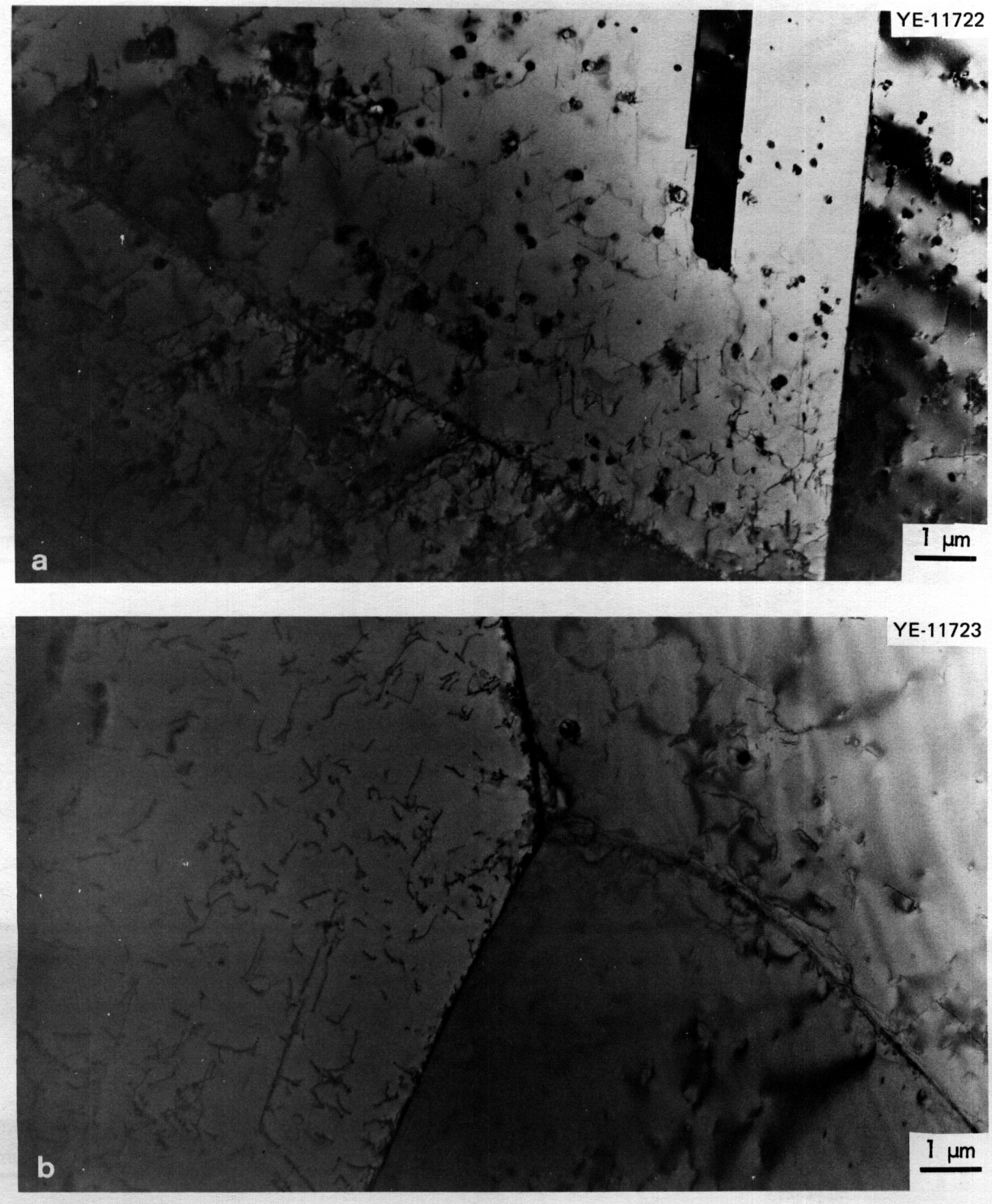

Fig. 3.2.13. The TEM Microstructure of the As-Received Finished 13-mm-Thick Plate Stock of Path A PCA. Inhomogeneity in this sample with respect to TiC and hence titanium concentration is shown by typical areas (a) containing coarse TiC and (b) without TiC.

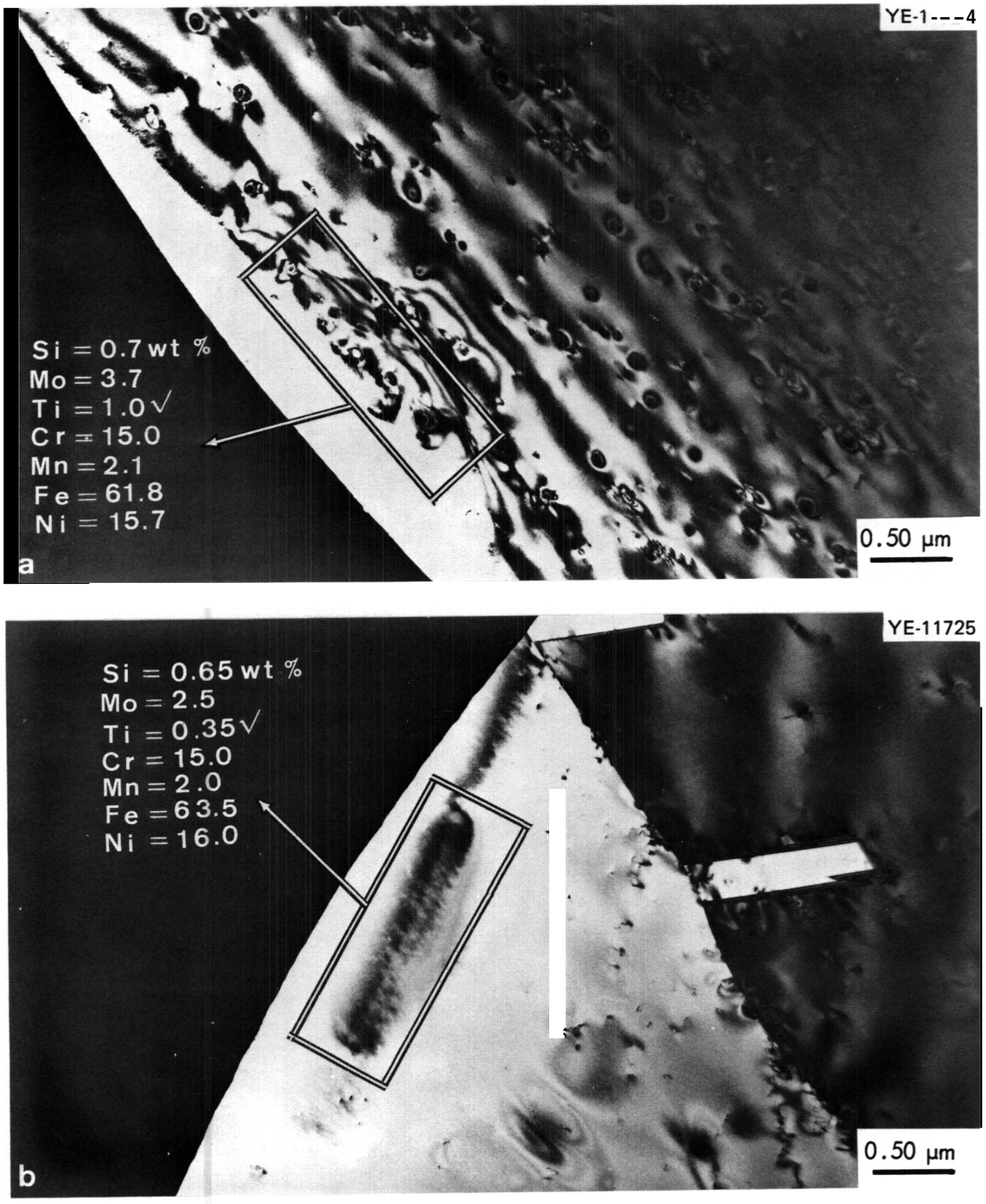

Fig. 3.2.14. Normalized Microanalysis *of* the Sample in Fig. 3.2.12 Using Energy-Dispersive X-Ray Analysis. (a) An area containing TiC particles. (b) *An* area without TiC particles. Note the large difference in titanium concentration.

Table 3.2.2. Normalized Microchemical Analysis of As-Received Path A PCA

Element	Content, wt %			
	0.13-mm Intermediate Bar[a]	13-mm Finished Plate		
		Two TiC Areas		No TiC Area
Si	0.32 ± 0.01	1.14	0.70	0.65
Mo	2.68 ± 0.07	2.84	3.7	2.5
Ti	0.30 ± 0.08	0.90	1.0	0.35
Cr	15.0 ± 1.0	15.70	15.0	15.0
Mn	2.5 ± 0.3	2.0	2.1	2.0
Fe	63.2 ± 0.4	61.62	61.8	63.5
Ni	16.0 ± 0.7	15.80	15.70	16.0

[a]Maximum error in counting statistics is 10% of each reported value. The statistical variations reported here represent area-to-area variations.

Kenik,[15] which shows that, although the metal atoms in TiC are predominantly titanium, they can be enriched in Mo, Nb, and Zr. The composition is otherwise in reasonable agreement with the bulk analyses reported in Table 3.2.1.

The plate stock shows a similar TiC distribution to experimental fabrication sequence A. The plate stock has coarser TiC particles and more spacial inhomogeneity than sequence A. The finished material was hot-worked at 1150°C, which was shown earlier to be capable of dissolving fine TiC, and the sequence A was hot-worked at 1050°C (see Fig. 3.2.1). Both, however, have in common the fact that they were not completely homogenized, as determined for the as-received intermediate bar. The experimental fabrication sequences showed that the lack of proper homogenization was primarily responsible for the increasing heterogeneity with increasing fabrication in sequence A. The same reasoning seems to apply to the as-received plate stock. Figure 3.2.15 shows a microstructure of the Fast Reactor Alloy Development Program Alloy D-9, which is similar in composition to ours, developed during neutron

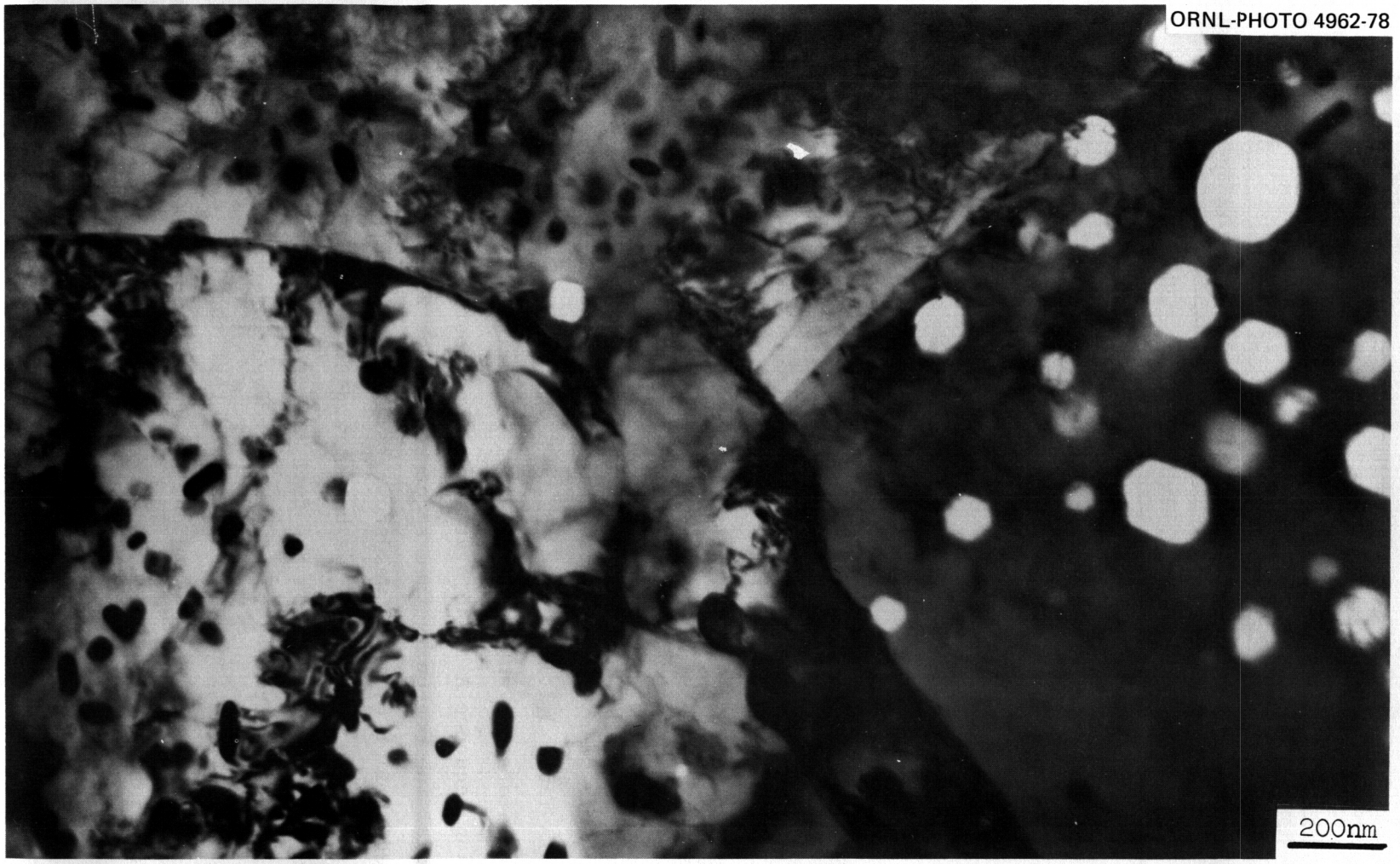

Fig. 3.2.15. Cold-Worked D-9, a Titanium-Modified Austenitic Stainless Steel Being Investigated by the Fast Breeder Reactor Alloy Development Program. Irradiated in EBR-II at 593°C to about 18 dpa and subsequently ion bombarded at 675°C to 165 dpa. Note gross grain-to-grain differences in void swelling and precipitation. Data from E. H. Lee, P. S. Sklad, and A. R. Rowcliffe, ORNL.

irradiation at about 600°C to about 18 dpa in EBR-II and subsequent ion irradiation at 675°C to about 165 dpa. Swelling and precipitation differ greatly from grain to grain, but that doesn't seem unreasonable if the irradiation started with gross titanium heterogeneities like those observed above. Optimum TiC distribution will not only protect from helium effects such as swelling and embrittlement, but should also be responsible for phase stability, if properly maintained. As important as TiC is to the microstructure, and microstructural control is to irradiation resistance, inhomogeneity in the as-received plate stock of Path A Prime Candidate Alloy is clearly unacceptable and must be corrected. Investigations of homogenizing have begun in order to solve this problem. One difficulty may be that the areas containing 1.0 wt % Ti have exceeded the local solubility product [wt % Ti][wt % C] at the homogenization temperature and that some TiC will therefore be in equilibrium with that austenite. Bulk diffusion on a gross scale will be necessary in order to remove titanium from areas of high concentration so that more TiC can dissolve. Clearly such problems should be avoided, and it seems that proper fabrication techniques with the goal of homogeneity can be achieved. More work will be required to establish the optimum procedure, but it seems that proper care to homogenize at temperatures of 1200°C or higher is desirable early in the sequence and possibly several times during fabrication. The hot-working temperature range should probably not be capable of both dissolving TiC at the high end (such as at 1150°C) and precipitation at the low end (around 925°C). It may be better to hot work at 1200 to 1050°C, where the TiC may stay in solution, or at 1050 to 925°C, where once precipitated, it will not redissolve. Use of the lower working temperature range would probably need rehomogenization after a given amount of fabrication.

Given identical homogenization treatments and hot working sequences, air cooling seems to be better than water quenching with respect to microhomogeneity of fine TiC formation.

3.2.5 Conclusions and Future Work

1. At an intermediate step in the fabrication, the Path A Prime Candidate Alloy was examined and found to be inhomogeneous with respect to stringers of TiC in unrecrystallized regions, as well as containing fine TiC.

2. Homogenization was examined at 1150, 1200, 1250, and 1300°C. At all temperatures fine TiC dissolved, but 1200°C was selected to try to obtain a more uniform distribution of titanium.

3. Homogenization followed by hot work at 1050°C produced a stable fine precipitate of TiC that resisted complete recrystallization even after 15 min at 1050°C. Air cooling led to a better fine distribution of TiC in recrystallized regions and less recrystallization overall than water quenching after homogenization.

4. Fabrication and a failure to homogenize clearly produced a structure with macro- and microinhomogeneity.

5. The as-received 13-mm plate stock of Path A Prime Candidate Alloy is clearly inhomogeneous on the scale of several grains. Some grains contain 1.0 wt % Ti and considerable TiC, while others without TiC have about 0.35 wt % Ti. This inhomogeneity must be corrected before developing desired microstructures for irradiation.

Fabrication of reactive-metal-modified austenitic stainless steels is far more difficult and requires more care than fabrication of standard austenitic steels. It is not, however, impossible. Sensitivity of the microstructure component TiC to variables such as homogenization temperature, hot-working temperature, and cooling rate following homogenization has been established. In order to exercise proper microstructural control and variation before irradiation, attention must be given to fabrication of an alloy with those capabilities. To specify a composition or microstructure without being able to produce it defeats the purpose of alloy development from the beginning.

Future work will include trying to homogenize the as-received finished material, safe fabrication into specimen material, and obtaining data for TTP curves for solution-annealed and 20%-cold-worked material to observe particle sizes and distributions of TiC for preirradiation microstructural variation.

3.2.6 References

1. *Metals Handbook,* 8th ed., Vol. 1, American Society for Metals, Metals Park, Ohio, 1961, p. 414.
2. P. J. Maziasz and E. E. Bloom, "Comparison of Titanium-Modified and Standard Type 316 Stainless Steel Irradiated in HFIR – Swelling and Microstructure," *ADIP Quart. Prog. Rep. January–March 1978,* DOE/ET-0058/1, pp. 40-53.
3. P. J. Maziasz and E. E. Bloom, "Mechanical Properties of Type 316 and Titanium-Modified Type 316 Stainless Steel Irradiated in HFIR," *ADIP Quart. Prog. Rep. January–March 1978,* DOE/ET-0058/1, pp. 54–62.
4. R. A. Grange, "Microstructural Alterations in Iron and Steel During Hot Working," *Proc. 9th Sagamore* Army *Materials Research Conf. (Raquette Lake, N.Y., Aug. 28–31, 1962),* Syracuse University Press, Syracuse, N.Y., 1964.
5. N. W. Woldman, *Metal Process Engineering,* Reinhold, New York, 1948, pp. 82–87.
6. D. N. Braski and J. M. Leitnaker, *Production* of *Homogeneous Titanium-Hastelloy N Alloys,* ORNL/TM-5697 (February 1977). *Metall. Trans.* 10A: 427 (1979).
7. A. F. Rowcliffe and J. M. Leitnaker, "Microstructural Studies on the Fabrication of a Large Heat of D9C1," in preparation.
8. A. S. Grot and J. E. Spruiell, "Microstructural Stability of Titanium-Modified Type 316 and Type 321 Stainless Steel," *Metall. Trans.* 6A: 2023 (1975).
9. J. M. Leitnaker and J. Bentley, "Precipitate Phases in Type 321 Stainless Steel After Aging 17 Years at 600°C," *Metall. Trans.* 8A: 1605–13 (1977).
10. T. K. Roche, "Status of Path A Prime Candidate Alloy Procurement and Fabrication," *ADIP Quart. Prog. Rep. October–December 1978,* DOE/ET-0058/4, p. 40.
11. J. M. Silcock and A. W. Denham, "Precipitation of NaCl-Type Carbides in Austenite and Their Behaviour in the Neighbourhood of Grain Boundaries," pp. 59-64 in *The Mechanism* of *Phase Transformations in Crystalline Solids* (Proc. Int. Symposium Univ. Manchester, July 3–5, 1968), Monograph and Report Series 33, The Institute of Metals, London, 1969.

12. D. Turnbull, *Impurities and Imperfections,* American Society for Metals, Metals Park, Ohio, 1955.

13. E. Orowan, "Theory of Yield Without Particle Shear," *Symposium on Internal Stress in Metals,* Institute of Metals, London, 1948, p. 451.

14. N. F. Mott and F.R.N. Nabarro, *Report on Conf. on Strength of Solids,* Physical Society, London, *1948,* p. 1.

15. Private communication, E. A. Kenik, Oak Ridge National Laboratory, May 1979.

4. PATH B ALLOY DEVELOPMENT — HIGHER STRENGTH Fe–Ni–Cr ALLOYS

Path B alloys are the Fe–Ni–Cr "superalloys" in which tensile, creep–rupture, and fatigue strength levels higher than attainable in the austenitic stainless steels are achieved by precipitation of one or more phases. Many alloys in this class exhibit low swelling in fast–reactor irradiations. The technology for use of path B alloys in neutron radiation environments is not as advanced as for path A alloys. A basis to select a specific alloy type for further development is lacking. Accordingly, the ADIP task group has selected five base research alloys that are representative of the basic systems of path B alloys and deserve consideration for fusion reactor applications. The systems under investigation include γ' strengthened–molybdenum modified, Y'strengthened–niobium–modified, $\gamma'\gamma''$ strengthened, and a high–nickel precipitation–strengthened alloy (~75% Ni).

Near–term activities are focused on evaluating the effects of a fusion reactor neutron spectrum on key mechanical and physical properties. Damage created by the fusion reactor neutron spectrum is approximated by fission reactor irradiation. Data are presently being obtained on a limited number of commercial alloys on which scoping studies were initiated two to three years ago. The emphasis will shift to base research alloys as they become available. For those properties that are either inadequate or degraded to an unacceptable level, the influence of composition and microstructure on the response will be examined. The research program will be oriented toward determination of mechanisms responsible for the observed property changes and the effects of metallurgical variables on the response. The objective is to develop a basis for selection of the path B prime candidate alloy(s).

4.1 THE FRACTURE MODE OF NIMONIC PE-16 FOLLOWING IRRADIATION IN HFIR — F. W. Wiffen (ORNL)

4.1.1 ADIP Task

ADIP Task I.B.14, Tensile Properties of High Strength—High Temperature Fe-Ni-Cr Alloys.

4.1.2 Objectives

Nimonic PE-16 was chosen as a representative precipitation-strengthened Path B alloy for investigation of the effect of HFIR irradiation on physical and mechanical properties. The HFIR experiments were initiated to investigate the response to irradiation producing helium levels representative of fusion reactor service simultaneously with production of displacement damage. Experiments in this series have been irradiated to neutron fluences producing 2 to 28 dpa and helium contents of 120 to 5700 at. ppm. Specimens irradiated at temperatures between 55 and 700°C are being examined to determine tensile properties and fracture mode. The results will be correlated with transmission electron microscopy of the microstructures produced by the irradiation.

4.1.3 Summary

Examination of a series of irradiated and tensile tested PE-16 specimens showed that grain boundary separation was the predominant fracture mode over a wide range of conditions. For irradiation and test at 300°C the transition from a ductile shear fracture to mainly grain boundary separation occurred at a fluence producing approximately 1000 at. ppm He. At 600 and 700°C all observed fractures were intergranular, even at as low as 350 at. ppm He. Although most failures were by grain separation, total elongations up to 10%were observed, usually accompanied by slip steps on the boundaries or limited areas of dimples characteristic of ductile tearing. Exposed boundaries showed evidence of the underlying precipitate structure, with boundaries at 300°C relatively clean, and the coarseness of the precipitate increasing with increasing irradiation temperature.

4.1.4 Progress and Status

This is a continuation of reporting on the results of a series of HFIR irradiation experiments containing tensile-swelling samples of Nimonic PE-16. These experiments have spanned the irradiation temperatures of 55 to 700°C, and achieved displacement levels of 2.2 to 28 dpa and irradiation-produced helium contents of 120 to 5700 at. ppm. Complete examination of the experiments will include immersion density, tensile tests, fractography, and microstructural examination.

Scanning electron microscopy has been completed on a series of tensile-tested specimens irradiated in the solution treated and aged condition (4 h at 1080°C followed by 16 h at 700°C). Table 4.1.1 summarizes the irradiation conditions and tensile ductility for the fractography specimens.

Table 4.1.1. Irradiation Conditions and Ductility for Selected Fractographic Samples. All samples irradiated in the solution treated and aged condition in the HFIR peripheral target position

Irradiation and Test Temperature (°C)	Neutron Fluence, >0.1 MeV (n/m^2)	Displacement Damage (dpa)	Helium Content (at. ppm)	Elongation, %	
				Uniform	Total
300	0.96×10^{26}	7.3	866	0.3	2.7
300	1.11	8.7	1210	0.14	0.49
300	2.0	15.2	2580	0.0	0.0
600	2.05	15.2	2590	0.43	0.46
700	0.56	4.2	350	4.6	9.6
700	1.83	13.7	2210	0.1	0.1

Tensile tests at 300 or 400°C for samples irradiated at the same temperature as the test showed a transition in fracture mode with fluence. Figure 4.1.1 shows a series of fractures of specimens irradiated and tested at 300°C. In Fig. 4.1.1(a), where the irradiation-produced helium content was 866 at. ppm, the fracture was by transgranular shear, with some areas showing ductile dimples and some areas nearly

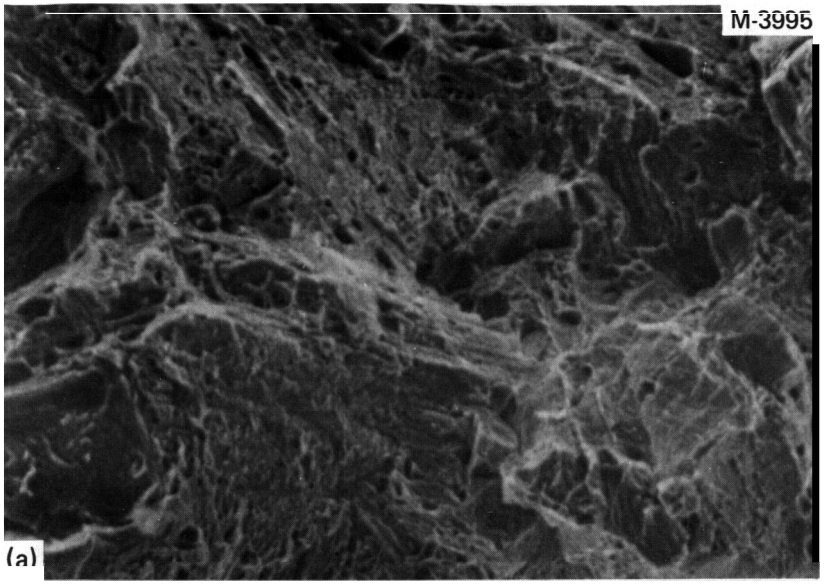

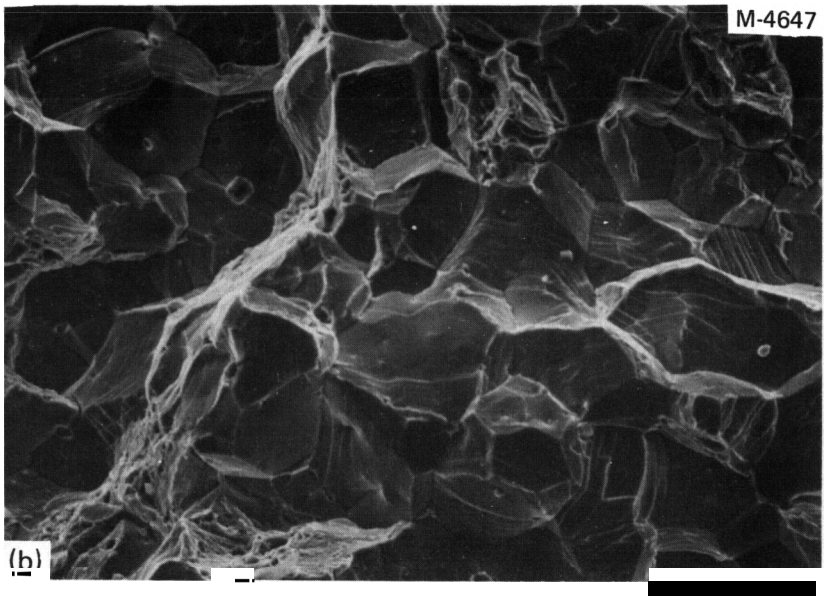

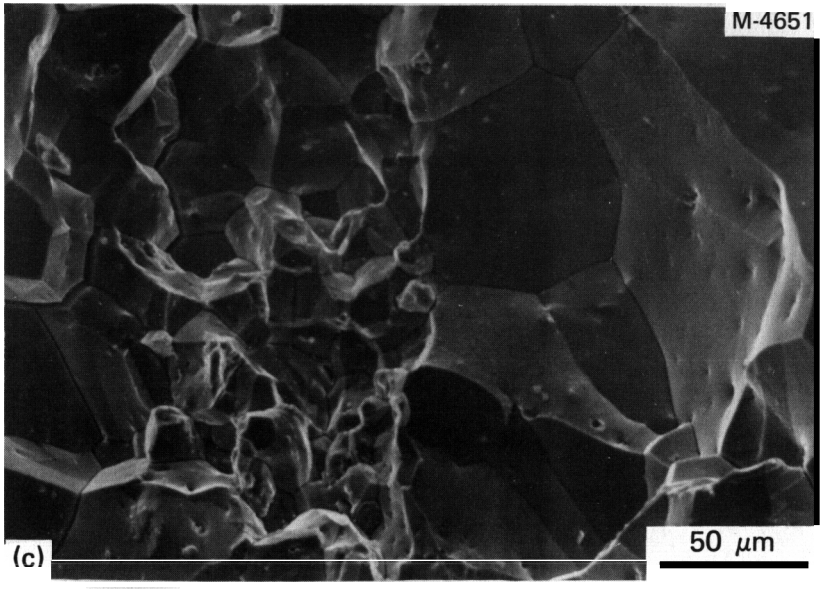

Fig. 4.1.1. Fracture Surfaces of Samples of Nimonic PE-16 Irradiated and Tested at 300°C. (a) Helium content 866 at. ppm, total elongation 2.7%. (b) 1210 at. ppm He, total elongation 0.49%. (c) 2580 at. ppm He, total elongation 0.0%.

planar. Planar areas showed slip steps and may be grain boundary surfaces. Irradiation producing a higher helium content, 1210 at. ppm, led to a fracture that was approximately 80% grain boundary separation and 20% ductile dimpled area. Numerous slip steps were visible on the exposed grain boundaries, Fig. 4.1.1(b). At a still higher helium content, 2580 at. ppm, the fracture surface was almost exclusively grain boundary separation [Fig. 4.1.1(c)].

Similar results were seen on fracture surfaces of specimens irradiated and tested at 400°C. In a sample containing 707 at. ppm He areas showing ductile dimples were predominant, but a number of grain boundaries were also exposed by the fracture. With a helium content of 1230 at. ppm failure was mainly by grain boundary separation, revealing smooth, clean boundaries. All samples examined after irradiation and testing at 600 or 700°C had fractured predominantly by grain separation, in some cases after total elongation of up to 10%. All exposed grain boundaries also showed a second level of structure related to second-phase precipitation. (Confirmatory electron microscopy has not yet been completed.)

The progressive development of the secondary features on grain boundaries is shown in Fig. 4.1.2, where the "precipitate" structure is coarser at the higher fluence. This secondary structure on the grain boundaries was a result of the elevated-temperature irradiation, and not of the test temperature and environment. A specimen irradiated at about 55°C to a fluence producing 355 at. ppm He was also tensile tested at 700°C. Failure was by grain separation, but the exposed grain boundaries did not show the precipitate structure of the specimens irradiated at high temperatures.

The dependence of the grain boundary precipitate phase on the irradiation temperature is shown for irradiation temperatures of 300, 600, and 700°C in Fig. 4.1.3. It is significant that, although these structures were quite different, all failed by grain separation.

4.1.5 Future Work

Additional tensile tests, fractography, metallography, and transmission electron microscopy are under way and will be described in future quarterly reports.

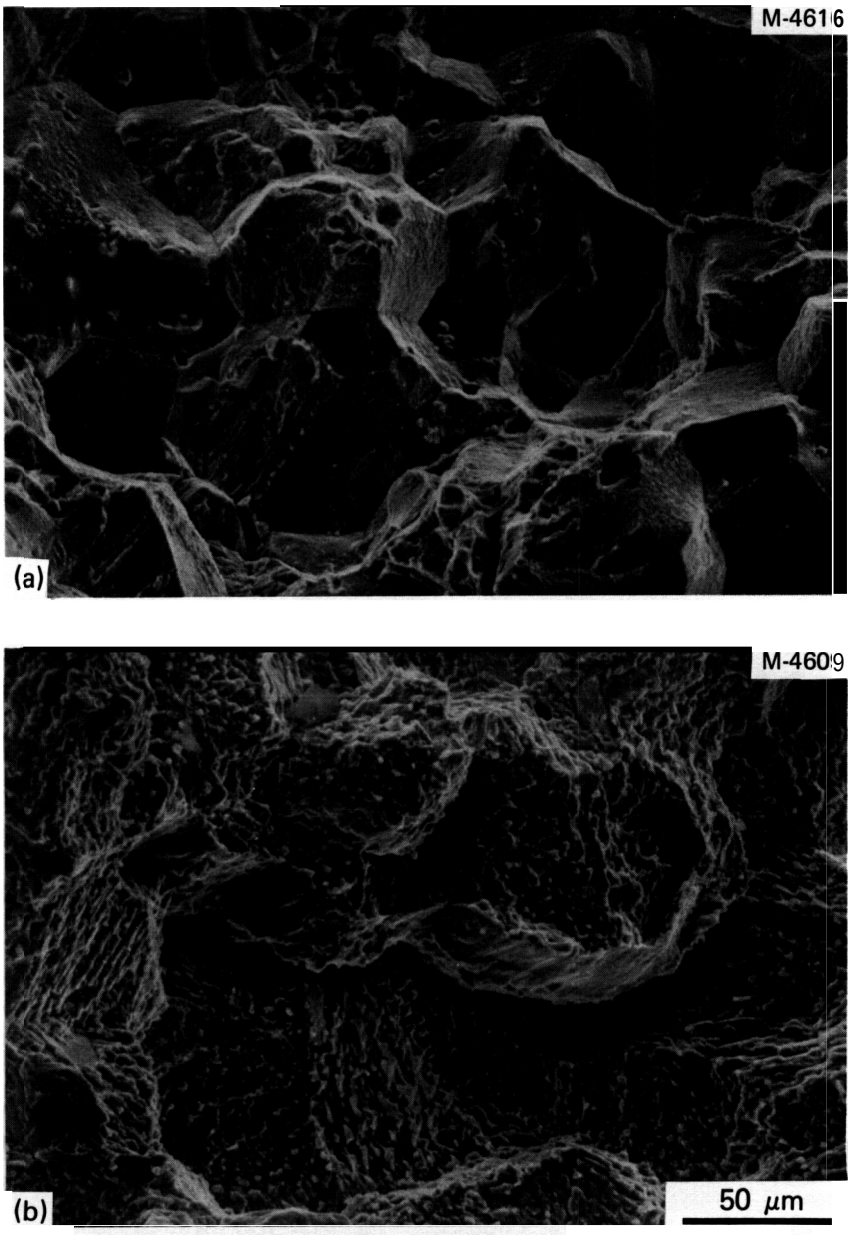

Fig. 4.1.2. Fracture Surfaces of Samples of Nimonic PE-16 Irradiated and Tested at 700°C. (a) 350 at. ppm He, total elongation 9.6%. (b) 2210 at. ppm He, total elongation 0.1%.

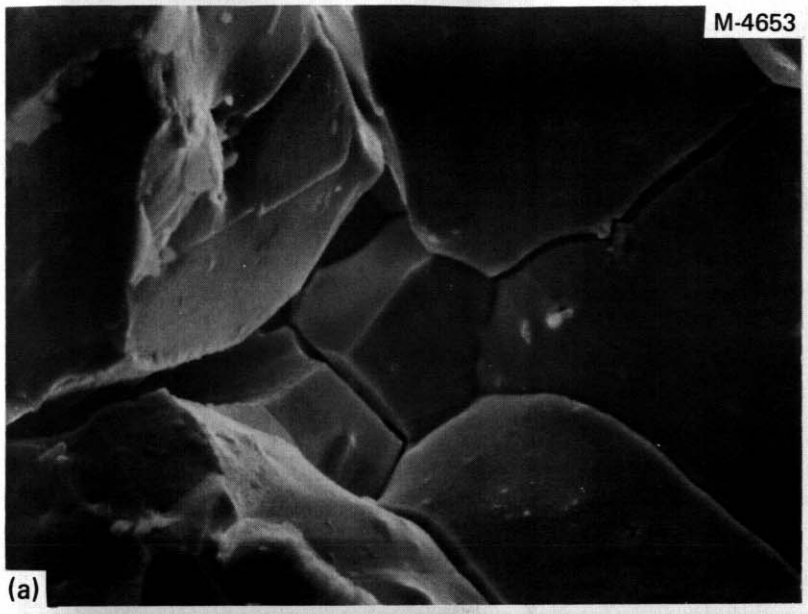

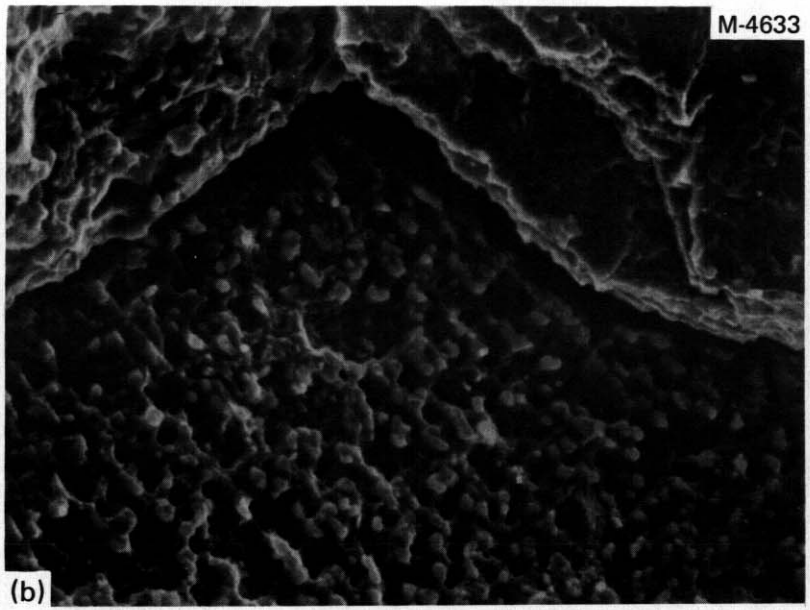

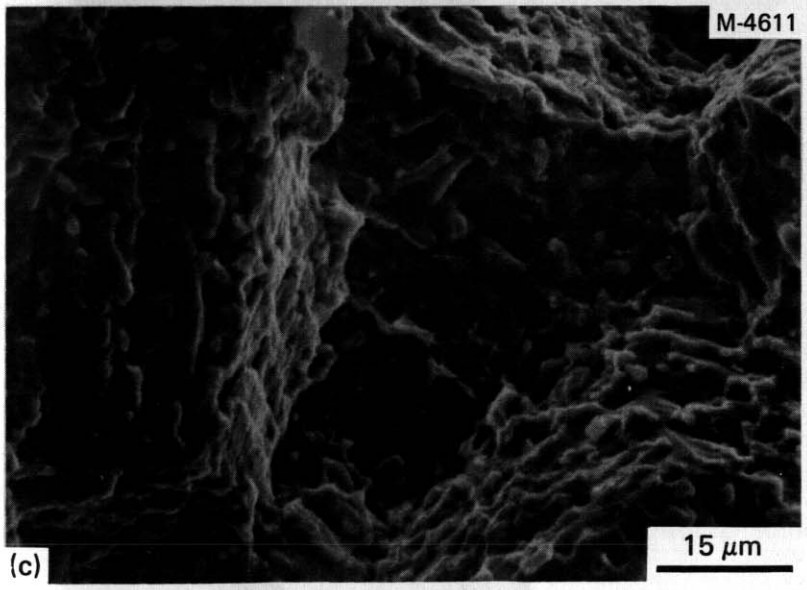

Fig. 4.1.3. Fracture Surfaces of Nimonic PE-16 Irradiated in the HFIR. (a) Irradiated and tested at 300°C, 2580 at. ppm He, 0.0% total tensile elongation. (b) Irradiated and tested at 600°C, 2590 at. ppm He, 0.46% elongation. (c) Irradiated and tested at 700°C, 2210 at. ppm He, 0.1% elongation.

4.2 STATUS OF PATH B BASE RESEARCH ALLOY PROCUREMENT AND FABRICATION — T. K. Roche (ORNL)

4.2.1 ADIP Task

ADIP Task I.D.1, Materials Stockpile for MFE Programs.

4.2.2 Objectives

The objective of this activity is to procure and fabricate the five Path B Base Research Alloys, which will provide a starting point for development of high-strength precipitation-strengthened alloys with properties specifically tailored for fusion applications.

4.2.3 Summary

Two 140-kg heats of each of five high-nickel alloys were double vacuum melted and hot rolled into bar stock. Some of each alloy has been extruded into round and sheet bar. Part of the sheet bar of each alloy has been processed to 1.27 and 0.61-mm (0.050 and 0.024-in.) sheet.

4.2.4 Progress and Status

As reported previously,' approximately 185 kg (400 lb) of 0.1-m (4-in.) round-cornered square bar of each of the five Path B Base Research Alloys was produced by Teledyne Allvac. A small quantity of each alloy was subsequently extruded to 32-mm-diam (1 1/4 in.) round bar and 20-mm-thick (0.8-in.) sheet bar at ORNL. During the present report period sheet stock 1.27 and 0.61 mm (0.050 and 0.024 in.) thick of the five alloys was processed to provide material for corrosion testing and microstructural characterization, respectively. The vendor's chemical analyses of the alloy heats involved in this work are shown in Table 4.2.1. Details of sheet processing are described below.

Rolling billets were cut from the 20-mm-thick (0.8-in.) hot-extruded sheet bar of each alloy. Alloys B-1, -2, -3, and -4 were hot rolled at 1100°C (2012°F) from 20 to 2.5 mm (0.8 to 0.1 in.) thick, then annealed at the same temperature for 15 min and air cooled.

Table 4.2.1. Vendor's Chemical Analyses of Path B Base Research Alloys

Element	Content, wt %, in Each Alloy (Heat)				
	B-1 (5-271-1)	B-2 (J-268-2)	B-3 (5-267-1)	B-4 (J-264-1)	B-6 (J-262-1)
Ni	24.14	39.47	29.61	40.00	74.73
Cr	9.94	11.71	12.36	11.80	15.20
Fe	Bal	Bal	Bal	Bal	4.86
Mb	1.03	2.98	0.02	0.02	0.02
Nb	0.02	0.04	2.01	2.90	0.98
Ti	3.05	1.40	1.93	1.63	2.28
Al	1.59	1.38	0.50	0.31	1.35
Mn	1.01	0.08	0.92	0.14	0.19
Si	0.32	0.28	0.27	0.27	0.25
C	0.032	0.032	0.026	0.026	0.02
W	0.02	0.02	0.02	0.02	0.02
co	0.01	0.01	0.01	0.01	0.01
cu	<0.01	<0.01	<0.01	<0.01	<0.01
P	0.006	0.004	0.01	0.01	0.009
Ta	0.01	0.01	0.01	0.02	0.01
Zr	0.05	0.06	0.03	0.03	0.04
V	0.02	0.02	0.02	0.02	0.02
S	*0.004*	0.003	0.003	0.001	0.001
0	0.0009	0.0023	0.0011	0.0021	0.0011
N	0.0011	0.0028	0.0026	0.0021	0.0007
B	0.002	0.002	0.003	0.004	0.002
As	<0.01	<0.01	<0.01	<0.01	<0.01

After descaling, the alloys were cold rolled to 1.27 mm (0.050 in.) thick, annealed about 15 min at 1050°C (1922°F) in hydrogen, wire brushed, and pickled, and finally a portion of each alloy was further cold rolled to 0.61 mm (0.024 in.) thick. Alloy B-6 was processed in essentially the same manner except that two intermediate anneals in

hydrogen were used during cold rolling, one at a thickness of 2.16 mm (0.085 in.), and the other at a thickness of 1.22 mm (0.048 in.).

The results of metallographic examination of the alloys following the hydrogen anneal and pickling treatment at a sheet thickness of 1.27 mm (0.050 in.) [alloy B-6 was at a thickness of 2.16 mm (0.085 in.)] can be seen in Figs. 4.2.1 through 4.2.5. Alloy B-3 contained a relatively large amount of second phase (Fig. 4.2.3).

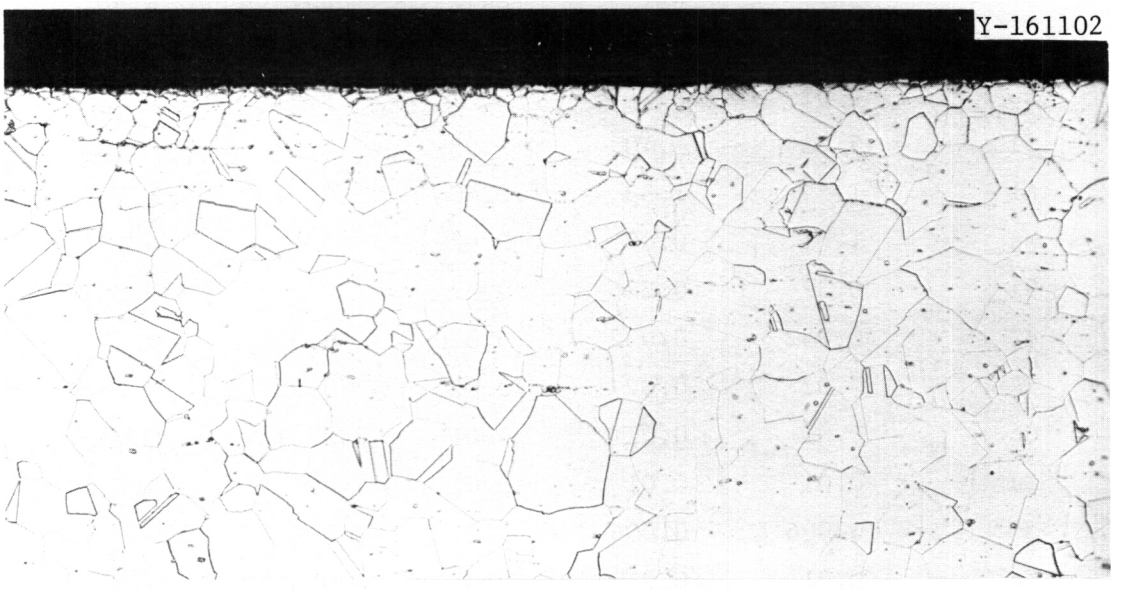

Fig. 4.2.1. Alloy B-1. Cold rolled 2.5 to 1.3 mm (0.1–0.50 in.) thick. Annealed 15 min at 1050°C in H_2. Pickled in H_2O–HNO_3–HF. 100×.

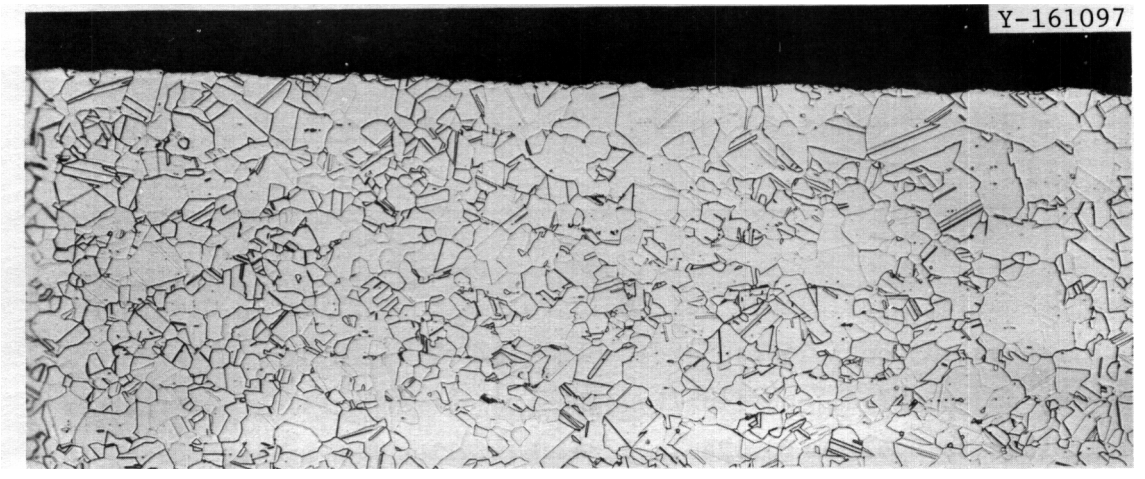

Fig. 4.2.2. Alloy B-2. Cold rolled 2.5 to 1.3 mm (0.1–0.050 in.) thick. Annealed 15 min at 1050°C in H_2. Pickled in H_2O–HNO_3–HF. 100×.

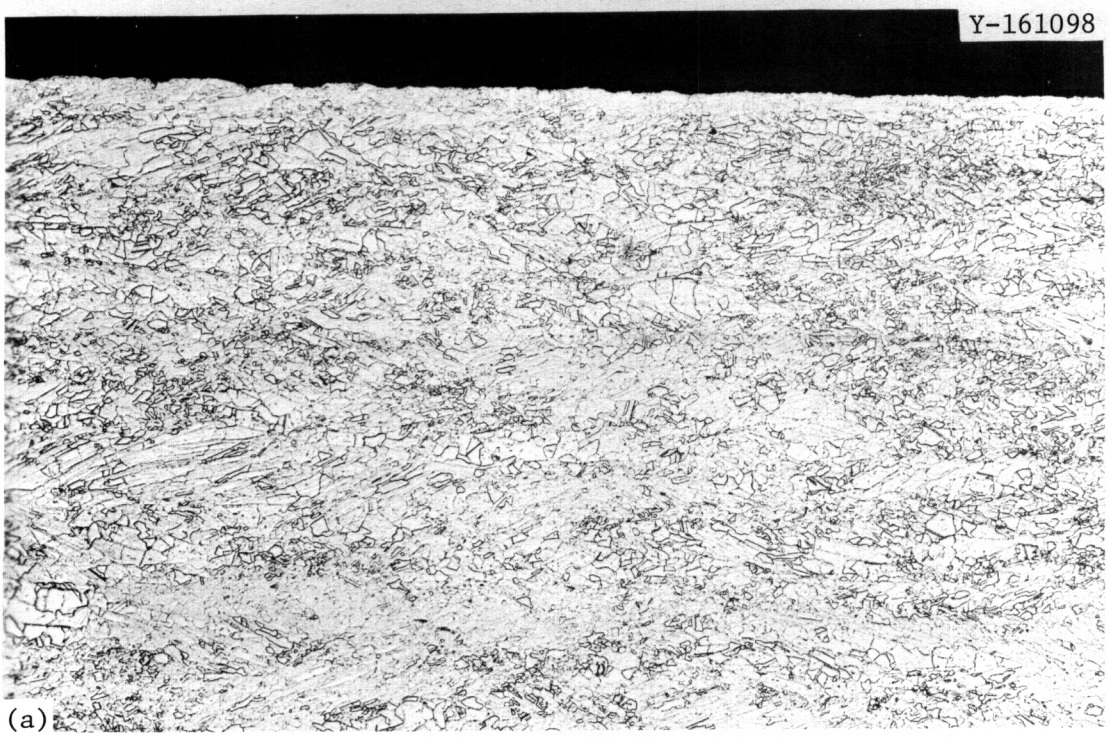

(a)

(b)

Fig. 4.2.3. Alloy B-3. Cold rolled 2.5 to 1.3 mm (0.1—0.050 in.) thick. Annealed 15 min at 1050°C in H_2. Pickled in H_2O-HNO_3-HF. (a) 100×. (b) 500×.

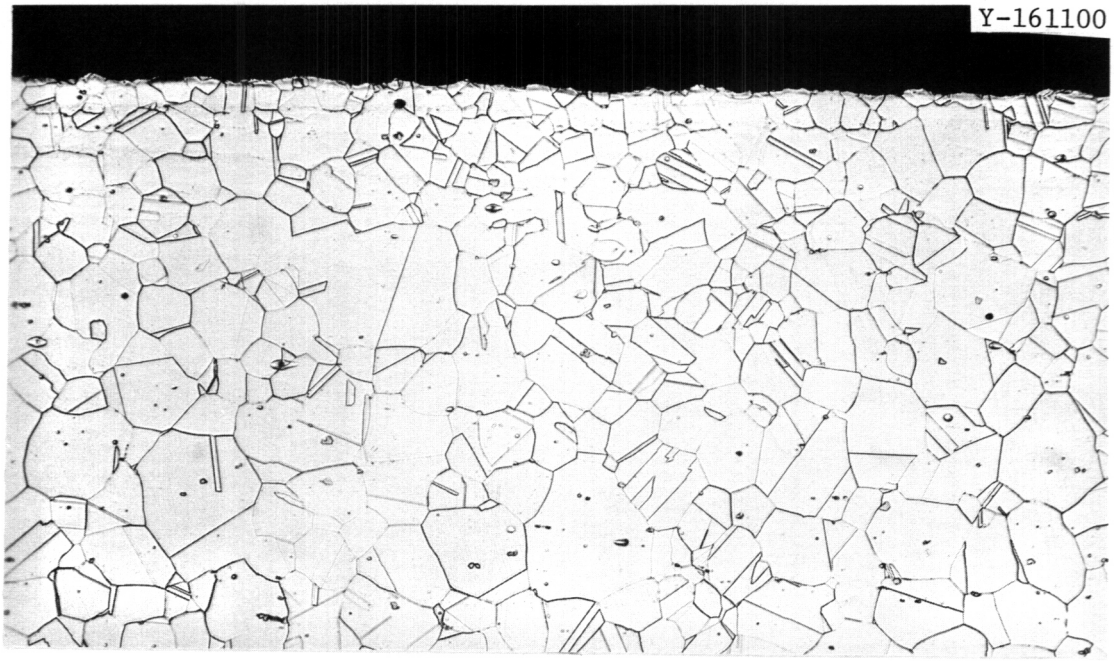

Fig. 4.2.4. Alloy E-4. Cold rolled 2.5 to 1.3 mm (0.1—0.050 in.) thick. Annealed 15 min at 1050°C in H_2. Pickled in H_2O–HNO_3–HF. 100×.

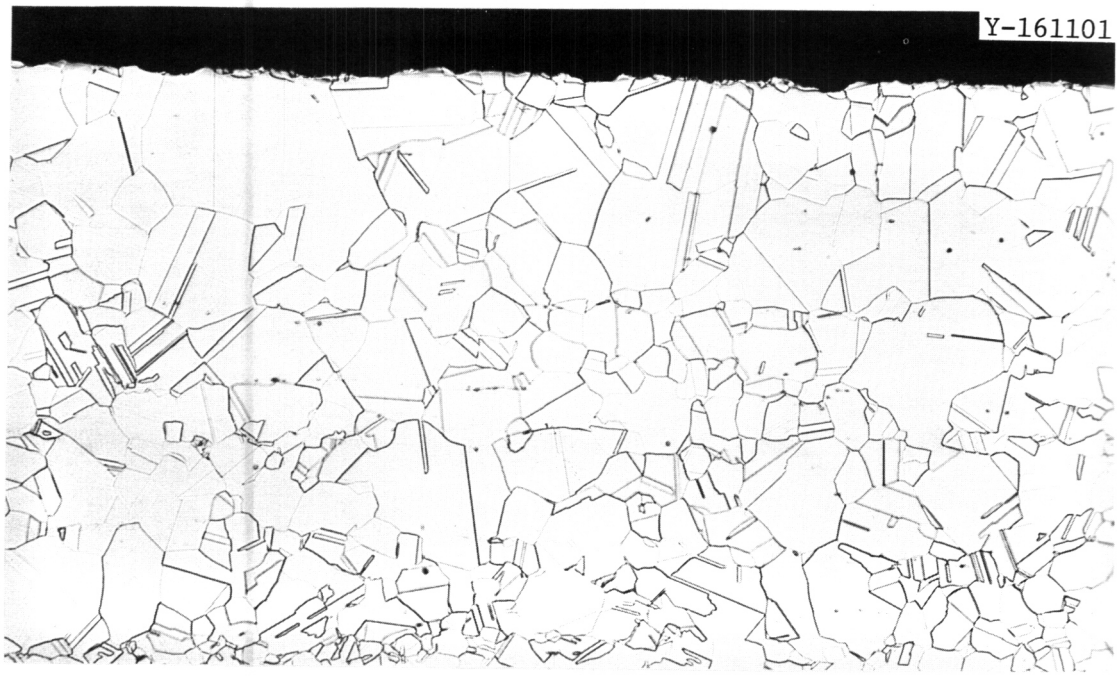

Fig. 4.2.5. Alloy B-6. Cold rolled 2.84 to 2.16 mm (0.112—0.085 in.) thick. Annealed 15 min at 1050°C in H2. Pickled in H_2O–HNO_3–HF. 100×.

4.2.5 Reference

1. T. K. Roche, "Status of Path B Base Research Alloy Procurement and Fabrication," *ADIP Program Quart. Prog. Rep.* **October-December 1978,** DOE/ET-0058/4, pp. 57-58.

5. PATH C ALLOY DEVELOPMENT — REACTIVE AND REFRACTORY ALLOYS

Two distinct and separate subgroups fall under the broad classification of path C alloys. These subgroups are conveniently classified as "reactive metal alloys" and "refractory metal alloys." Analyses of the properties required for performarice of materials in high-flux regions of fusion reactors and assessments of the known and extrapolated properties have identified titanium alloys of the reactive metal alloys and vanadium and niobium alloys of the refractory metal alloys as having the most promise for fusion reactor applications. For both the reactive and refractory alloys, there is an extreme lack of data that are relevant and necessary for selection of specific alloy types for development (i.e., solid solution, precipitation strengthened, single or multiphase). In the case of titanium alloys, the most critical deficiency is the lack of data on the response of these alloys to high-fluence neutron radiation. For vanadium and niobium alloys, while the effects of radiation on mechanical behavior are not adequately known, perhaps the most alarming deficiency is the near total lack of base-line information on the effects of cyclic (fatigue) loading on mechanical performance. Precisely because of these deficiencies in the data base and overall metallurgical experience, these alloys are still in a "scoping study" phase of their evaluation as candidates for fusion reactor first-wall materials.

The ADIP task group has selected four titanium alloys, three vanadium alloys, and two niobium alloys for the scoping phase of the development program. Titanium alloys are generally classified according to the relative amounts of α (hcp) and β (bcc) phases that they contain. The titanium alloys selected represent the three alloys (types α plus β, α rich, and β rich). Vanadium and niobium alloys are not in commercial use as are the other alloy systems in the program. Selection of the scoping alloys was based primarily on results of previous programs on vanadium cladding development for LMFBRs and high-temperature alloys for space power systems. The three vanadium alloys are V—20% Ti, V—15% Cr—5%Ti, and Vanstar 7. The binary has relatively good fabricability, and appears to be swelling resistant in fast-reactor irradiations but

is rather weak. The ternary V—15% Cr—5% Ti and precipitation-strengthened Vanstar 7 alloys are significantly stronger. The Nb—1% Zr binary alloy is included as a reference material, since a significant amount of data exists for this alloy irradiated in fast reactors. The alloy Nb—5% Mo—1%Zr is much stronger than the binary and can be developed for applications near 800°C.

Near-term activities on path C alloys will focus on obtaining data on the unirradiated mechanical properties, corrosion, and compatibility, and the effects of irradiation on physical and mechanical properties. Fission reactor irradiation with and without helium preinjection, high-energy neutron sources, and charged-particle irradiations will be used in the development of techniques to approximate the effects of the fusion reactor neutron spectrum (He/dpa production). The objective is to develop sufficient understanding of the behavior of path C alloy systems (Ti, V, and Nb alloys) to allow selection of path C base research alloys. The effects of composition and microstructure on alloy performance will then be investigated in the base research alloys.

5.1 THE MICROSTRUCTURES OF TITANIUM SCOPING ALLOYS FOLLOWING LOW-FLUENCE NEUTRON IRRADIATION AT 450°C —

J. A. Sprague and F. A. Smidt, Jr. (Naval Research Laboratory)

5.1.1 ADIP Task

I.C.4. Microstructures and Swelling in Reactive/Refractory Alloys (Path C).

5.1.2 Objective

The objective of this study was to examine the microstructures of the titanium scoping alloys Ti-6Al-4V (beta anneal), Ti-38-6-44, and Ti-15-333 following low-fluence neutron irradiation to obtain preliminary indications of the phase stabilities of these alloys in an irradiation environment.

5.1.3 Summary

The titanium scoping alloys Ti-6Al-4V (beta annealed), Ti-38-6-44, and Ti-15-333 were examined by transmission electron microscopy (TEM) following irradiation in EBR-II to a fluence of 3.4×10^{21} neutrons/cm^2, $E > 0.1$ MeV, equivalent to 2.1 displacements per atom (dpa), at a temperature of 450°C. The principal microstructural changes observed in the Ti-6Al-4V were the formation of small dislocation loops and some nearly planar features identified as beta-phase precipitates in the alpha grains of the alloy. The Ti-38-6-44 and Ti-15-333, both of which are metastable beta alloys containing alpha-phase precipitates, both precipitated additional alpha phase during irradiation. The precipitation in the metastable beta alloys was consistent with that which occurs in these alloys during long thermal aging at the irradiation temperature, although the irradiation probably enhanced the transformation kinetics. The precipitation of fine beta phase in the Ti-6Al-4V, however, appeared to be an irradiation-induced effect, since the known thermal phase diagram for the alloy indicates that the preirradiation alpha phase should be stable at the irradiation temperature.

5.1.4.1 Background

Titanium alloys are among the several classes of materials currently being considered for fusion reactor first-wall and blanket applications. Although titanium alloys have been extensively studied, mostly in connection with aerospace applications, little is known about their respones to neutron irradiation. The first step in gathering the necessary irradiation damage data on Ti-alloys for the fusion materials program is the investigation of a series of scoping alloys,' which include the three major alloy types: near-alpha (also called super-alpha), alpha plus beta, and near-beta alloys. The first opportunity to examine these alloys after neutron irradiation has been provided by the stress-relaxation experiment previously reported by Nygren.[2] The microstructures of unstressed control specimens from this experiment have been studied by TEM in a joint effort among McDonnell-Douglas, HEDL, and NRL. In the progress report €or the previous quarter, Sastry, et. al,[3] reported on the structures of the alpha plus beta alloy Ti-6Al-4V in the mill-annealed and duplex-annealed conditions and the near-alpha alloy Ti-5621S, while the present authors reported on the other near-alpha scoping alloy, Ti-6242S.[4] In the NRL portion of the work during the present reporting period, neutron-irradiated specimens of Ti-6Al-4V (beta-annealed), Ti-38-6-44, and Ti-15-333 were examined, and unirradiated specimens of beta-annealed Ti-6Al-4V and Ti-38-6-44 were further studied to aid the interpretation of irradiation-induced microstructural changes.

5.1.4.2 Experimental Procedures

The nominal compositions (weight percent) of the alloys examined in the present study were: Ti-6%Al-4%V; Ti-3%Al-8%V-6%Cr-4%Mo-4%Zr; and Ti-15%V-3%Cr-3%Al-3%Sn. The preirradiation heat treatments given to these alloys have been described by Davis, et. al,[1] and Nygren,' but will be repeated here for ease of reference. The beta-anneal of Ti-6Al-4V was 1040°C/30 min plus A.C. plus 730°C/2 hour. The Ti-38-6-44 and Ti-15-333 were both solution treated and aged, the Ti-38-6-44 schedule being 815°C/30 min plus "rapid cool" plus 620°C/4 hour, and the Ti-15-333

schedule being 760°C/30 min plus A.C. plus 510°C/16 hours. The alloys were irradiated in EBR-II in the form of small beams, 1-mm thick. The irradiation conditions quoted previously by the present authors[4] were preliminary numbers, which have now been updated. More complete calculations' have yielded a neutron fluence of 3.4 x 10^{21} n/cm^2, E > 0.1 MeV, a damage level of 2.1 dpa, and an irradiation temperature of 450°C. Following irradiation, TEM specimens were prepared at HEDL by chemically milling the beams to thicknesses of approximately 0.2 mm in a solution of 65% HNO_3, 18% HF, and 17% H_2O at 0°C, and punching 3-mm disks.' The specimens were then shipped to NRL for final preparation and TEM examination. Final thinning was performed in a dual-jet electropolisher using a solution of 300 ml methyl alcohol, 175 ml n-butyl alcohol, and 15 ml perchloric acid at a temperature of -60°C. The specimens were examined in a JEM-200A electron microscope operating at 200 kV.

5.1.4.3 Results and Discussions

5.1.4.3.1 **Ti-6Al-4V,** Beta-Annealed. The preirradiation microstructure of the beta-annealed **Ti-6Al-4V,** shown in Fig. 5.1.1 (a), consisted primarily of acicular Widmanstatten alpha plates with interplatelet beta. The dark bands which appear between the alpha and beta phases in this micrograph are the interface phase, an fcc transition structure which forms during cooling from above the beta transition temperature.[7] After irradiation, as illustrated in Fig. 5.1.1(b), the basic Widmanstatten structure was retained, and dense internal damage structures developed in both the alpha and beta phases. Due to imaging difficulties, caused by the size and shape of the beta-phase plates, only the damage structure in the alpha phase was examined in any detail. The principal postirradiation features of the alpha-phase plates are illustrated in Fig. 5.1.2, a bright field-dark field series from one area of the specimen. The bright field micrograph, Fig. 5.1.2(a), imaged some large beta plates, dislocation loops, and some nearly linear features which appeared to be precipitates. The selected area diffraction of this area, Fig. 5.1.2(b), indicated a systematic $(1\bar{0}10)_\alpha$ diffraction condition, with satellite spots and streaks surrounding the primary reflec-

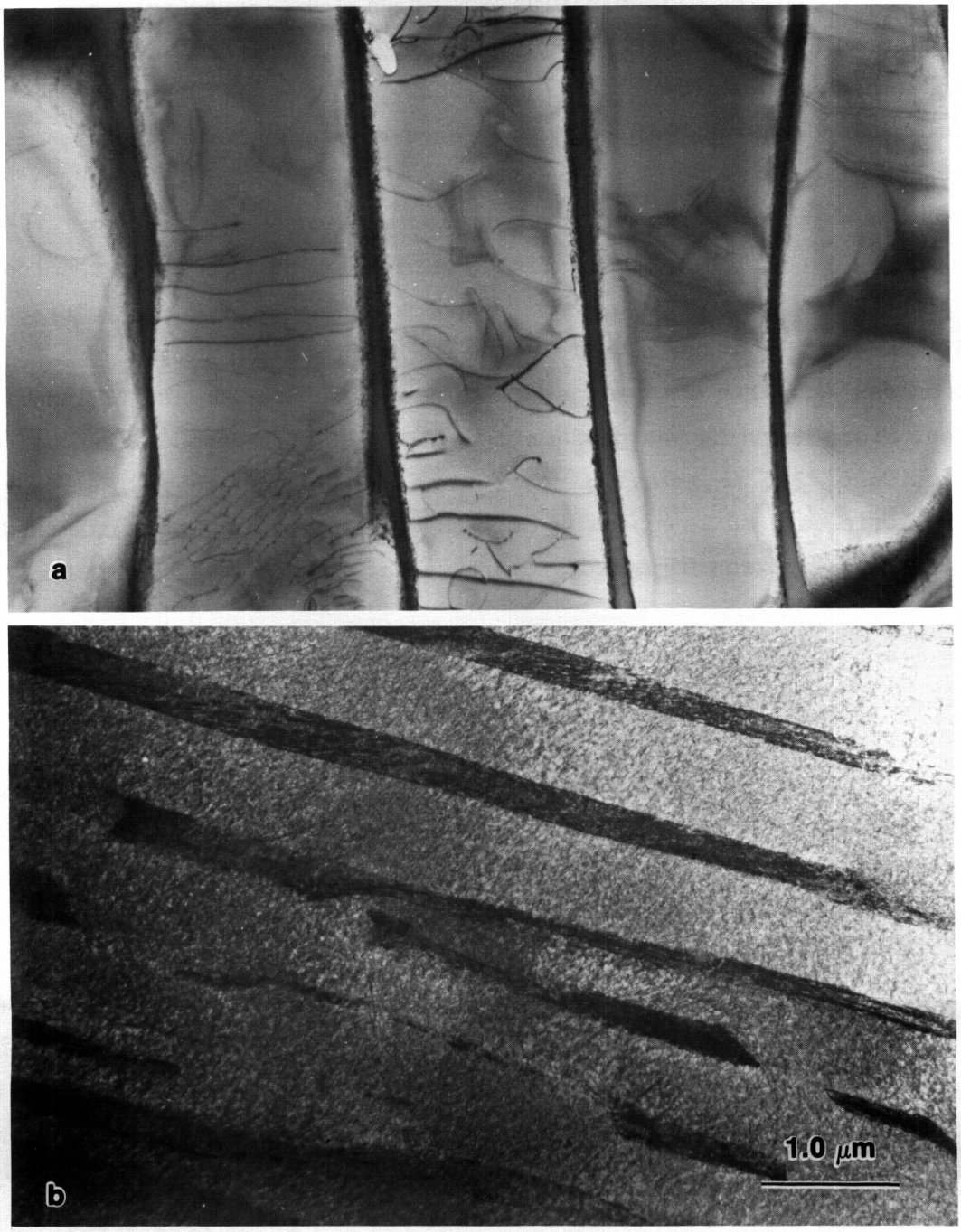

Fig. 5.1.1. Microstructures of beta-annealed Ti-6Al-4V: (a) unirradiated, showing Widmanstätten structure of alpha plates separated by interplatelet beta; (b) irradiated, showing retention of Widmanstätten structure with addition of dense internal damage structures in alpha and beta phases.

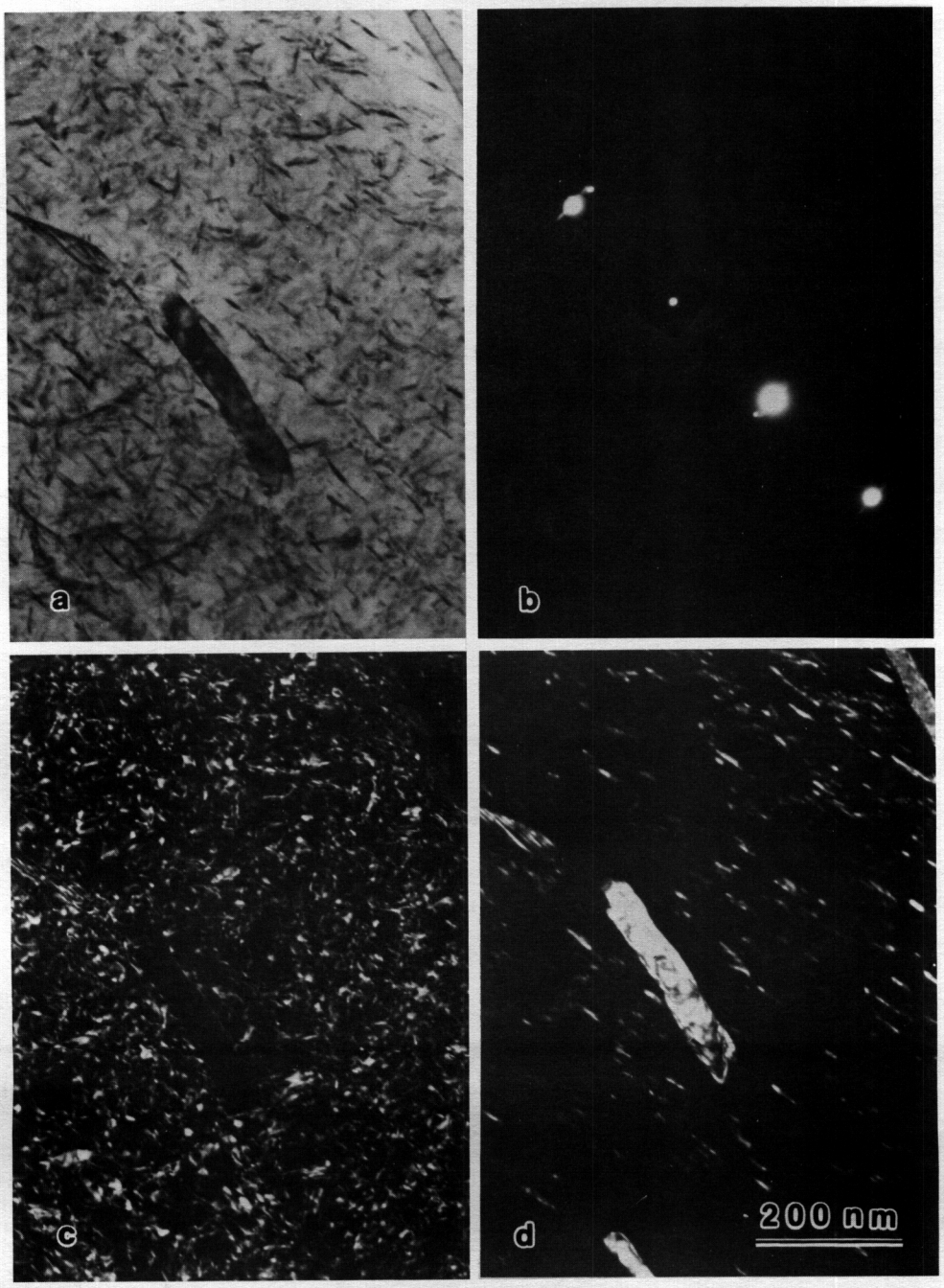

Fig. 5.1.2. Internal damage structure in an alpha grain of irradiated Ti-6Al-4V: (a) bright field image, containing beta plate, dislocation loops and fine beta precipitates; (b) SAD of the area, in a systematic $(10\bar{1}0)_\alpha$ diffraction condition, with $\{110\}_\beta$ satellite spots and streaks; (c) dark field, $(10\bar{1}0)_\alpha$ reflection, showing dislocation loops; (d) dark field, $(110)_\beta$ reflection, showing large beta plate and fine beta precipitates.

tions. The primary $(10\bar{1}0)_\alpha$ dark field image, Fig. 5.1.2(c), imaged the dislocation loops. The dark field micrograph formed with a satellite spot and streak, Fig. 5.1.2(d), imaged the large beta plates and a set of linear features with their long axes perpendicular to the streak.

When imaged under a number of beam directions and diffraction conditions, the linear features shown in Fig. 5.2 were identified as beta-phase precipitates, which agrees with identifications made by Sastry, et. al,[3] and Powell[6] of similar features observed in mill-annealed and duplex-annealed Ti-6Al-4V from the same irradiation experiment. The beta precipitates were approximately planar in form with a habit plane close to $(11\bar{2}0)$ in the parent alpha grains. The orientation of the beta precipitates was the common Burgers orientation relationship[8] produced by the transformation of beta phase to alpha phase on cooling of Ti-6Al-4V below the beta transus temperature.

Three mechanisms were considered for the precipitation of beta phase in alpha grains of Ti-6Al-4V during irradiation: acceleration of the diffusion kinetics of vanadium, allowing a supersaturated alpha matrix to decompose at temperatures at which thermal diffusion would be too slow to cause observable precipitation; irradiation-induced segregation' of vanadium to point defect sinks, increasing the local concenration beyond the phase boundary; irradiation-induced alteration of the relative stability of alpha and beta phases at a given concentration.[10] Regarding the possible existence of a supersaturated alpha phase, Rhodes and Paton,[7] in their explanation of interface phase formation, note that the alpha-beta transformation occurs on cooling through the beta transus temperature by the growth of alpha plates into the beta matrix. If the cooling rate is sufficiently rapid, they state that the alpha phase will form at a critical vanadium content higher than the equilibrium content for this phase. Looking at the Ti-Al-V phase diagram, however, it is difficult to use this argument to explain the precipitation of beta phase at 450°C. The diagrams published by Molchanova[11] indicate that the alpha phase in an alloy containing 6% Al should be stable at temperatures below 600°C for up to 4% V, the total vanadium content of Ti-6Al-4V. The supersaturation of the alpha plate with respect to vanadium concentration therefore does not seem likely.

Irradiation-induced segregation of vanadium, on the other hand, offers a possible explanation for the observed precipitation. Although the association of precipitates with point defect sinks could not be proven in the present study, Sastry et.al,[3] reported that the precipitates in irradiated mill-annealed and duplex-annealed Ti-6Al-4V formed preferentially on dislocation lines and low-angle boundaries. For fcc crystals, it has been shown theoretically' that solute elements which trap self-interstitial atoms will segregate, and possibly precipitate, at point defect sinks during irradiation. In nickel, the segregation and precipitation of silicon, which has a negative lattice misfit, has been observed by Auger analysis of ion-irradiated surfaces.[12] Recognizing that the generalization of results from fcc nickel to hcp titanium may not be valid, vanadium in alpha titanium has misfits of -3% on the a-axis and -6% on the c-axis,[13] so vanadium segregation during irradiation might be expected. It should be noted, however, that aluminum in alpha-titanium has misfits of ∿0% on the c-axis (at low concentrations) and -6% on the a-axis, so that the situation in an alloy containing both elements could be complex. Segregation-induced precipitation of beta phase during irradiation, however, remains a distinct possibility.

The alteration of the alpha-beta phase boundary by irradiation-produced point defects cannot be ruled out as a mechanism for the observed precipitation, but the assessment of this possibility was well beyond the scope of the present study. There is a potential coupling mechanism for this type of phase stability effect, since the thermal alpha to beta transformation is accompanied by a volume contraction of approximately 5%, but a considerable modeling effort would be required to translate this information into a phase diagram. This question, therefore, was left open.

5.1.4.3.2 Ti-38-6-44. The preirradiation microstructure of Ti-38-6-44, as discussed by Davis, et. al,[1] consisted of a beta matrix with large Type-2 alpha precipitates, shown in Fig. 5.1.3(a). Type-2, or "non-Burgers," alpha forms in many metastable beta Ti-alloys, in which it appears to be the more stable form of the alpha phase, forming at

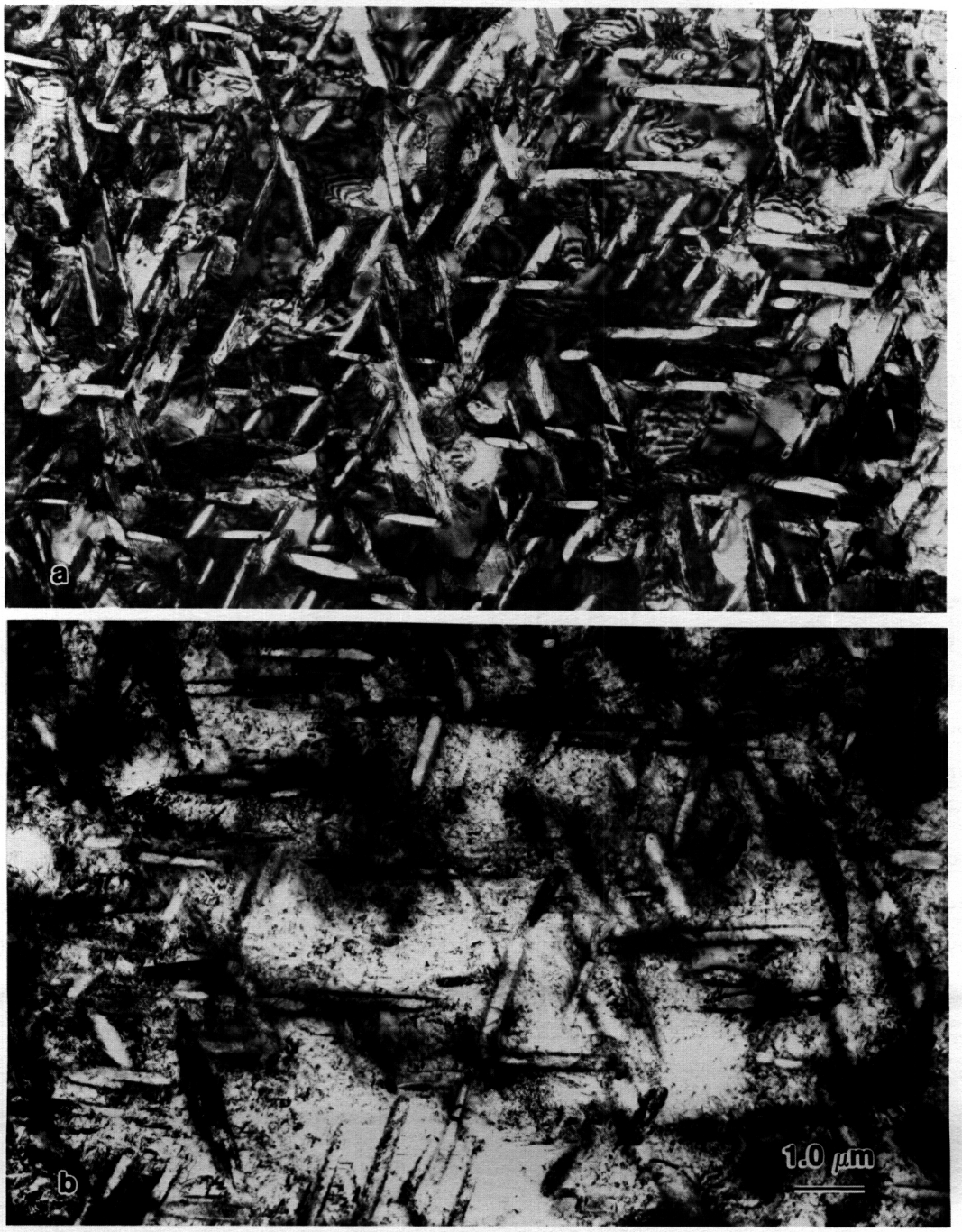

Fig. 5.1.3. Microstructures of Ti-38-6-44: (a) unirradiated, with large Type-2 alpha precipitates in a beta matrix; (b) irradiated, exhibiting some growth of the preirradiation alpha precipitates and additional precipitation of fine Type-2 alpha phase.

higher aging temperatures and longer aging times from the initially-precipitated Type-1 (Burgers orientation) alpha.[14,15] After neutron irradiation at 450°C, the preirradiation alpha precipitate had grown somewhat, and additional fine-scale Type-2 alpha phase had precipitated, as shown in Fig. 5.1.3(b). The precipitation of additional alpha phase during irradiation was very likely the result of the normal thermally-induced phase transformation, altered by irradiation-enhanced diffusion, since a larger volume fraction of alpha phase could be stable at 450°C than at the aging temperature of 620°C.

The size of the fine Type-2 alpha precipitates observed after irradiation at 450°C was consistent with the precipitation reported by Rhodes and Paton[15] after aging this same alloy at 350 and 500°C. Their results suggest, moreover, that the precipitation during irradiation would both increase the yield strength and decrease the ductility of the alloy. For reference, Rhodes and Paton found that an 8-hour age at 540°C produced 160 nm Type-2 alpha precipitates, giving a yield strength of 1133 MPa and a plastic failure strain of 8.9%, while a 28-day age at 350°C produced 15 nm Type-2 precipitates, giving a failure stress of 1379 MPa and no plastic strain. The irradiation-enhanced phase transformation, therefore, could have some serious effects on mechanical properties of this alloy.

5.1.4.3.3 Ti-15-333. This alloy was investigated in the irradiated condition only, results being compared to the microstructure shown by Davis, et. al.[1] At low magnification, as seen in Fig. 5.1.5(a), the irradiated microstructure was similar to those observed for Ti-38-6-44, and the electron diffraction patterns indicated Type-2 alpha precipitates in a beta matrix. The precipitates in the Ti-15-333, however, were somewhat smaller than those observed in Ti-38-6-44. Making a direct comparison of the irradiated microstructure at higher magnification, Fig. 5.1.4(b), with the preirradiation structure shown by Davis, et. al [their Fig. 5.1.4(b)], the primary discernable effect of the irradiation was some growth of the preirradiation precipitates. The high precipitate density in the alloy made it impossible to detect any dislocation loops or other lattice defects. Since little information is

readily available on structure-property relationships in Ti-15-333, it is difficult to speculate on the effect of the observed precipitate growth on mechanical properties. Qualitatively, one might expect less irradiation embrittlement of Ti-15-333 than of Ti-38-6-44 by looking at the microstructural changes, but more experiments would clearly be required to test this hypothesis.

5.1.4.3 Conclusions

Neutron irradiation of Ti-6Al-4V (beta-annealed), Ti-38-6-44, and Ti-15-333 to 2.1 dpa at 450°C produced the following microstructural changes:

- Ti-6Al-4V - formation of dislocation loops and planar beta-phase precipitates in the alpha phase, as well as a damage structure in the beta phase which was not identified;
- Ti-38-6-44 - some growth of the preirradiation Type-2 alpha precipitates and additional precipitation of fine Type-2 alpha in the beta matrix;
- Ti-15-333 - growth of the preirradiation Type-2 alpha precipitates; but qualitatively less change in phase distribution than was observed in Ti-38-6-44.

To summarize these findings and the previous data generated in the joint McDonnell-Douglas, HEDL, and NFU study of the titanium scoping alloys in this irradiation experiment, the near-alpha alloys showed the greatest phase stability during neutron irradiation, with the alpha plus beta and near-beta classes both showing significant redistributions of the pre-irradiation phases. Although some speculation on the impact of these phase redistributions on mechanical properties is possible with these limited data, the more comprehensive ADIP test matrix will be required to assess the suitability of the alloys for the fusion reactor environment.

5.1.5 Future Work

This completes the examination of the as-irradiated titanium scoping alloys from the EBR-II stress relaxation test. Microstructures of the titanium alloys in further irradiation experiments will be examined as they become available.

5.1.6 References

1. J. W. Davis, S. M. L. Sastry, and L. J. Pionke, "Microstructure of Titanium Scoping Alloys Prior to Irradiation," ADIP Quart. Prog. Rep. June 30, 1978, DOE/ET-0058/2, 85-99.
2. R. E. Nygren, "Irradiation Induced Stress Relaxation in Titanium Alloys," ADIP Quart. Prog. Rep. June 30, 1978, DOE/ET-0058/2, 106-116.
3. S. M. L. Sastry, J. E. O'Neal, and J. W. Davis, "Comparison of Titanium Alloy Ti-6Al-4V and Ti-5621S Microstructures After EBR-II Irradiation," ADIP Quart. Prog. Rep. Dec. 31, 1978, DOE/ET-0058/4, 72-84.
4. J. A. Sprague and F. A. Smidt, Jr., "The Microstructure of Ti-6242S Following Low-Fluence Neutron Irradiation at 400°C," ADIP Quart. Prog. Rep. Dec. 31, 1978, DOE/ET-0058/4, 67-71.
5. R. E. Nygren, Hanford Engineering Development Laboratory, private communication.
6. R. W. Powell, Hanford Engineering Development Laboratory, private communication.
7. C. G. Rhodes and N. E. Paton, "Formation Characteristics of the α/β Interface Phase in **Ti-6Al-4V,** Met. Trans. 10A:209-216 (1979).
8. W. G. Burgers, "On the Process of Transition of the Cubic-Body-Centered Modification into the Hexagonal-Close-Packed Modification of Zirconium," Physica I:562-586 (1934).
9. R. A. Johnson and N. Q. Lam, "Solute Segregation in Metals Under Irradiation," Phys. Rev. B13(10):4364-4375 (1976).
10. S. I. Maydet and K. C. Russell, "Precipitate Stability Under Irradiation: Point Defect Effects," J. Nucl. Mater. 64:101 (1977).
11. E. K. Molchanova, Phase Diagrams of Titanium Alloys, transl. by A. Halbreich, N. Kramer, and M. Statler, Daniel Davey and Co., Inc., New York, 1965, pp. 161-167.
12. L. E. Rehn, P. R. Okamoto, D. I. Potter, and H. Wiedersich, "Effect of Solute Misfit and Temperature on Irradiation-Induced Solute Segregation in Binary Ni Alloys," J. Nucl. Mater. 74:242-251 (1978).

13. W. B. Pearson, A Handbook of Lattice Spacings and Structures of Metals and Alloys, Pergamon Press, New York, 1958, pp. 872-877.

14. C. G. Rhodes and J. C. Williams, "The Precipitation of a-Phase in Metastable 6-Phase Ti-Alloys," Met. Trans. 6A:2103-2114 (1975).

15. C. G. Rhodes and N. E. Paton, "The Influence of Microstructure on Mechanical Properties in Ti-3Al-8V-6Cr-4Mo-4Zr (Beta-C)," Met. Trans. 8A:1749-1761.

5.2 COMPARISON OF THE MICROSTRUCTURE OF TITANIUM ALLOYS AFTER IRRADIATION IN EBR-II - S. M. L. Sastry, J. W. Davis, and J. E. O'Neal (McDonnell Douglas)

5.2.1 ADIP Task

Task Number 1-C.4. Microstructure and Swelling in Reactive and Refractory Alloys (Path C)

5.2.2 Objective

To determine the response of titanium alloy microstructures to neutron irradiation.

5.2.3 Summary

Post irradiation annealing studies of Ti-6Al-4V revealed that exposure to temperatures up to 500°C produced no significant changes in the defect microstructure. However, increasing the temperature to 560°C resulted in a rapid annihilation of dislocations and dislocation loops and their coalescence to form larger defects. The beta precipitates observed in the "as irradiated" samples were unaffected by the heat treatment.

Examination of irradiated Ti-6242s revealed the presence of a high density of defect clusters and dislocation loops but no evidence of beta precipitation. The prominant features of the defect structure were prismatic loops, stacking fault tetrahedra and spherically symmetrical defect clusters. Post irradiation annealing studies of Ti-6242s revealed that temperatures >700°C would have to be achieved before there is a rapid annealing of defect and defect clusters similar to that observed in Ti-6Al-4V. Exposure to 750°C resulted in the formation of small beta precipitates in the primary alpha.

Studies of the unirradiated beta alloy Ti-15-3 show that the microstructure essentially consists of a fine distribution of elongated alpha precipiates of varying orientation in a beta matrix. However, after irradiation, there appears to be a break-up of the alpha precipitate with the alpha precipitate tending towards a globular morphology.

5.2.4 Progress and Status

This work is part of a joint study between HEDL, MDAC, and NRL to determine the microstructural response of titanium to irradiation. The TEM specimens used in this study were obtained from a stress relaxation experiment conducted by R. E. Nygren of HEDL.[1] These specimens were irradiated in Row VII of EBR-II to a fluence of $\sim 3.0 \times 10^{21}$ n/cm2 (E_n >0.1 MeV). The temperature during irradiation was maintained at 450°C ± 30. Subsequent damage calculations performed at HEDL indicate that this fluence produced roughly 2.1 dpa's in titanium. This level of damage is higher than previously reported and is based on more recent information.[2]

In the last reporting period the effort at MDAC was directed towards examination of the Ti-6Al-4V and the Ti-5621s (Ti-5%Al-6% Sn-2%Zr-1% Mo-0.25% Si).[3] The Ti-6Al-4V was in the mill annealed and the duplex annealed condition, while the Ti-5621s was evaluated in the duplex condition. Examination of the Ti-6Al-4V revealed a fine precipitate of beta phase along with a high density of dislocation loops and debris. The beta phase was present in both heat treatment conditions of Ti-6Al-4V and was found at low angle grain boundaries and along dislocations which were produced during the heat treatment. They tended to be ellipsoidal in shape, roughly 100-200A° in size and appeared to follow the Burgers relationships. Examination of the Ti-5621S, however, showed no evidence of this precipitate. The primary defect structure consisted essentially of extensive dislocation loops and c+a type of dislocations.

At the conclusion of this reporting period several questions remained unanswered about the nature of the defect structure. For example, at what temperature would the defect loops become annihalated, and what happens to the beta precipitate during heating? In order to resolve these issues, during this reporting period, a series of annealing experiments were performed on the Ti-6Al-4V alloy using the hot stage of the electron microscope. In addition to the annealing studies, examination was also made of the radiation damage in Ti-6242s (Ti-6%Al-2% Sn-4%Zr-2% Mo-0.09% Si) and Ti-15-3 (Ti-15V-3Cr-3Al-3Sn) alloys, The Ti-6242s is a near alpha alloy (composed mostly of alpha) and is similar to Ti-5621s.

The Ti-15-3 is a beta alloy (composed mostly of beta). The Ti-6242s was in the duplex anneal condition while the Ti-15-3 was in the solution treat and age condition. The annealing times, temperatures, and microstructures have been previously published in a study by Davis, Sastry and Pionke.[4]

5.2.4.1 Post Irradiation Annealing Studies of Ti-6Al-4V

The temperature dependence of annealing of the neutron induced defect microstructure was determined by heating thin foils of Ti-6Al-4V in the hot stage of an electron microscope to temperatures ranging from 200-1000°C. Examination of samples during heating revealed that for temperatures up to 500°C and exposure times of up to 10 minutes no significant changes were observed in the defect microstructure other than a limited amount of defect annihilation. Increasing the temperature, however, to 560°C (0.43 T_m) resulted in a rapid annihilation of dislocations and dislocation loops and their coalescence to form larger defects. Figure 5.2.1 shows the duplex annealed Ti-6Al-4V in the "as irradiated" condition (Figure 5.2.1(a)) and the same region after annealing for 10 minutes at 560°C (Figure 5.2.1(b)). Figure 5.2.1(b) reveals that after annealing, the density of the defects is considerably less than the "as irradiated" sample. However, the fine beta precipitates previously observed in the irradiated specimens are still present after annealing, as seen at location "B" of Figures 5.2.1(a) and 5.2.1(b). The fact that the precipitate did not dissolve tends to support the conclusion that it is beta phase, since this temperature is in the two phase region (alpha + beta) and a beta phase should be stable. However, TEM examination of bulk annealed samples will have to be performed before final conclusions can be drawn.

5.2.4.2 Post Irradiation Microstructure of Duplex Annealed Ti-6242s

The irradiation induced defect structure in Ti-6242s is similar to that observed in Ti-5621s[3] and in agreement with the defect structure reported by Sprague and Smidt at NRL.[5] The main feature of the structure is a high density of defect clusters and dislocation loops and no evidence of beta precipitation. Figures 5.2.2(a) and 5.2.2(b) show the defect structure caused by the neutron irradiation, and reveal the presence of

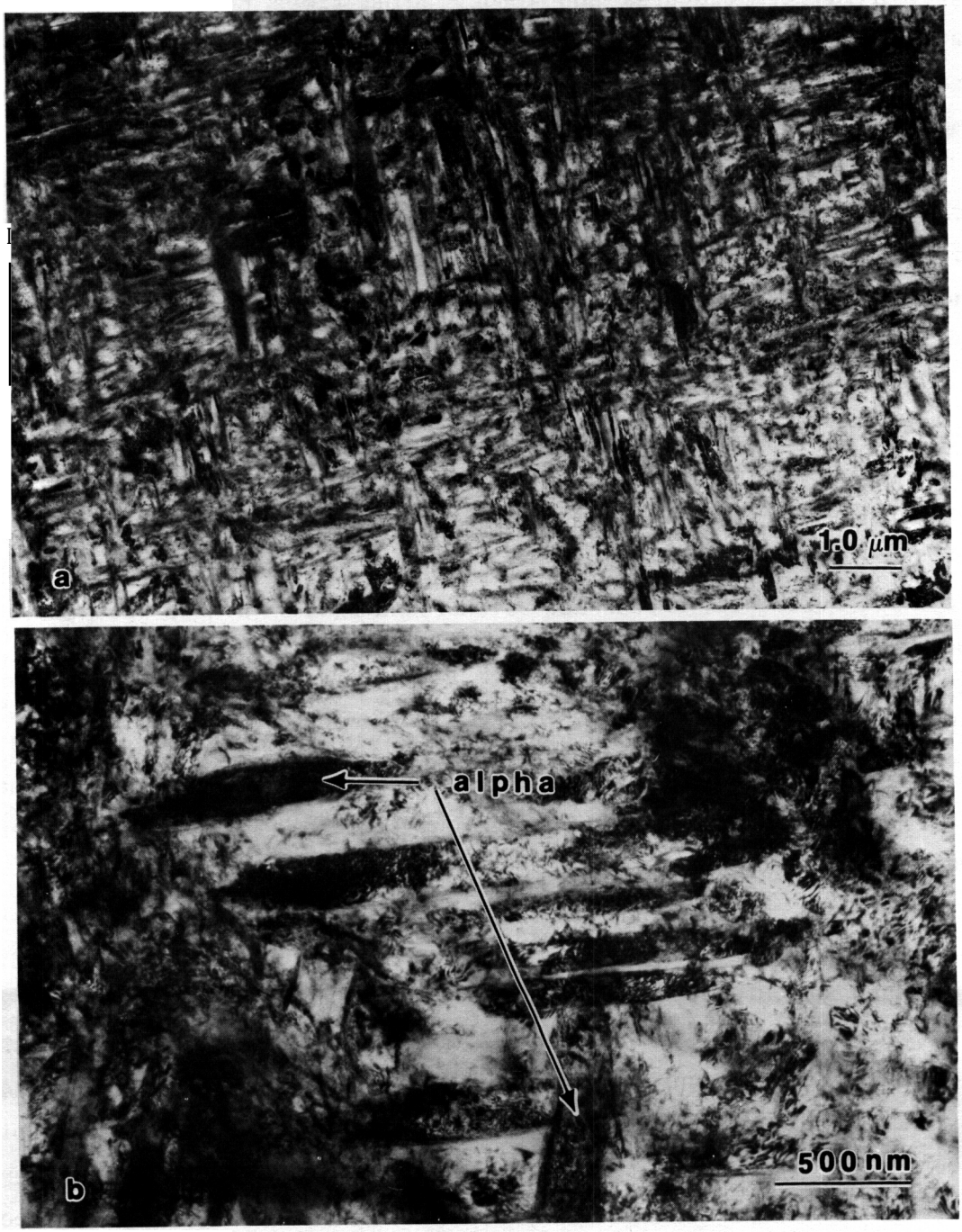

Fig. 5.1.4. Microstructure of irradiated Ti-15-333: (a) low magnification, showing similar structure to Ti-38-6-44, but with smaller precipitates (see Fig. 5.1.3); (b) higher magnification, showing growth of alpha precipitates during irradiation (compare with Fig. 5.1.4(b) of Davis, et. al[1]).

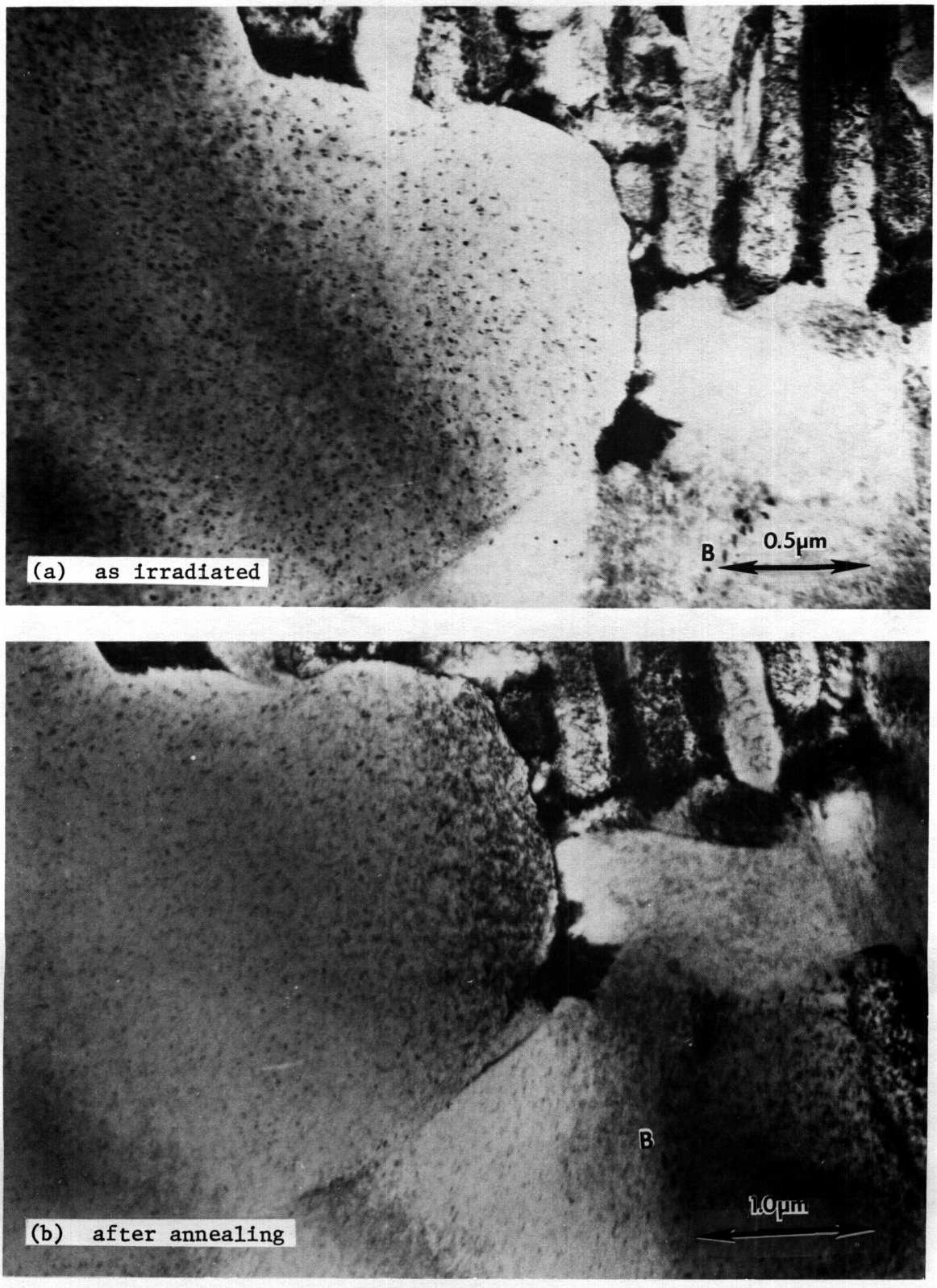

Figure 5.2.1 Microstructure of Duplex Annealed Ti-6Al-4V. (a) irradiated to 2.1 dpa at 450°C. (b) heated for 10 minutes at 560°C after irradiation.

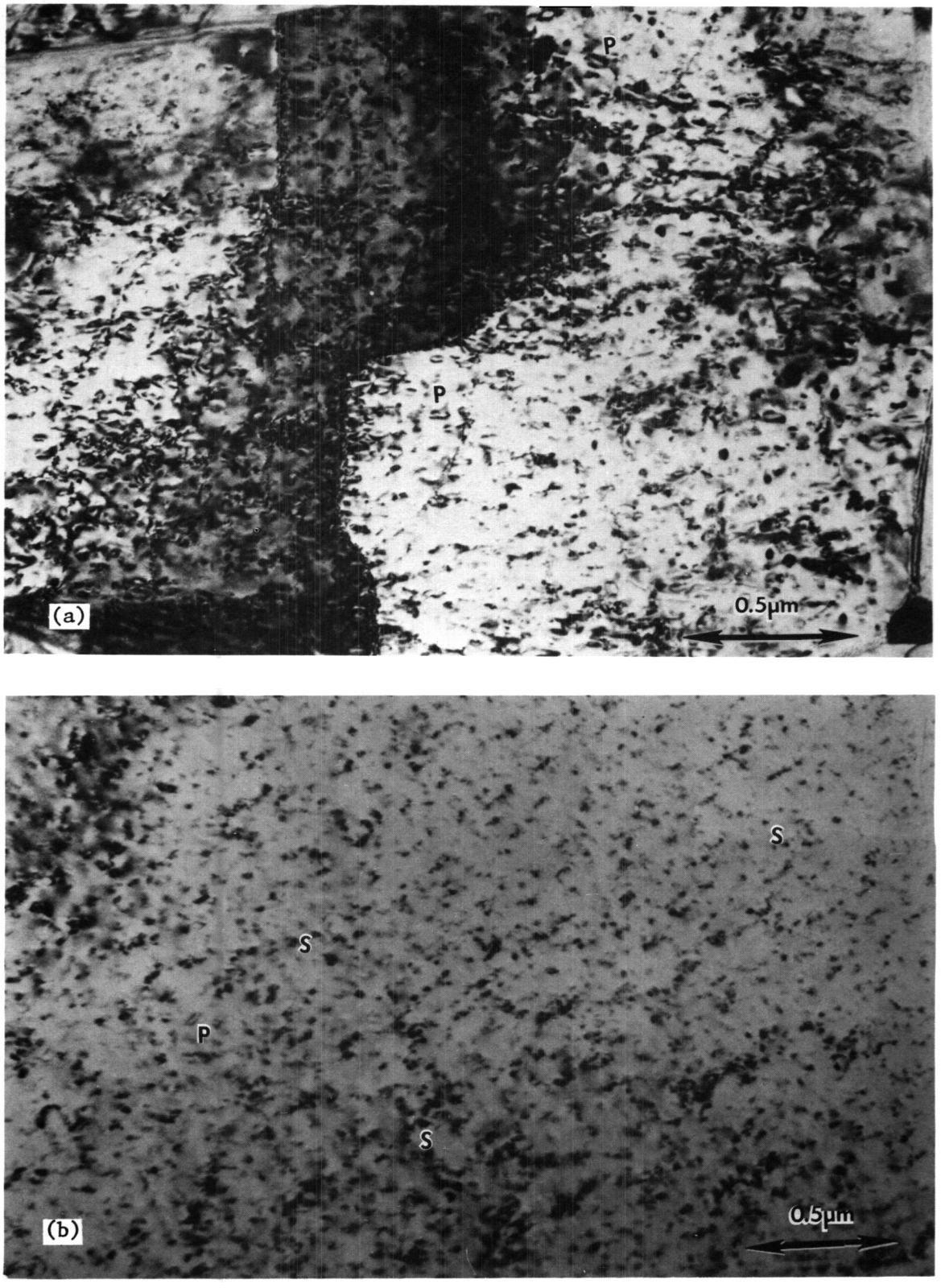

Figure 5.2.2 **Microstructure of Duplex Annealed Ti-6242s after irradiation to 2.1 dpa at 450°C. (a) bright field image. (b) two-beam excitation image.**

prismatic loops (see location "P" in Figures) which exhibit double arc contrast. In addition to the prismatic loops, stacking fault tetrahedra were also found (see location "S" in Figures) and exhibit a "V" shaped appearance. The final prominant feature of this structure are spherically symmetrical defect clusters.

5.2.4.3 Post Irradiation Annealing Studies of Ti-6242s

To determine the response of this structure to temperature, hot stage annealing experiments were also performed on Ti-6242s. The effect of temperature on the annealing of defect structure in Ti-6242s was found to be similar to that observed in Ti-6Al-4V.

Figure 5.2.3(a) shows the effect of annealing for 10 minutes at 525°C (0.42 T_m) while Figure 5.2.3(b) shows the same location after an additional exposure of 10 minutes at 650°C (0.53 T_m). Exposure to 525°C essentially resulted in no significant changes in defect structure and was essentially equivalent to the low temperature (500°C) exposure of Ti-6Al-4V. Increasing the temperature to 650°C produced some annealing of defects and defect clusters but nothing as dramatic as that observed in the 560°C exposure of Ti-6Al-4V. However, when the samples were given an additional 10 minutes at 750°C (0.53 T_m) small precipitates of beta phase were formed in primary alpha and the dislocations and dislocation loops tended to coalesce to larger defects. Figure 5.2.4(a) and 5.2.4(b) are bright and dark field electron micrographs of the beta precipitates observed in the Ti-6242s after the 750°C exposure, Further increases in the annealing temperature resulted in a coarsening of this precipitate.

5.2.4.4 Post Irradiation Microstructure of Solution Treated and Aged Ti-15-3

Figure 5.2.5(a) is an electron micrograph of the unirradiated beta alloy Ti-15-3 while Figure 5.2.5(b) is the alloy after neutron irradiation. The microstructure of the unirradiated specimen (Figure 5.2.5(a)) shows a fine distribution of differently orientated, elongated alpha precipitates in a beta matrix. However, after irradiation there appears to be a break-up of the alpha precipitate with the alpha precipitate

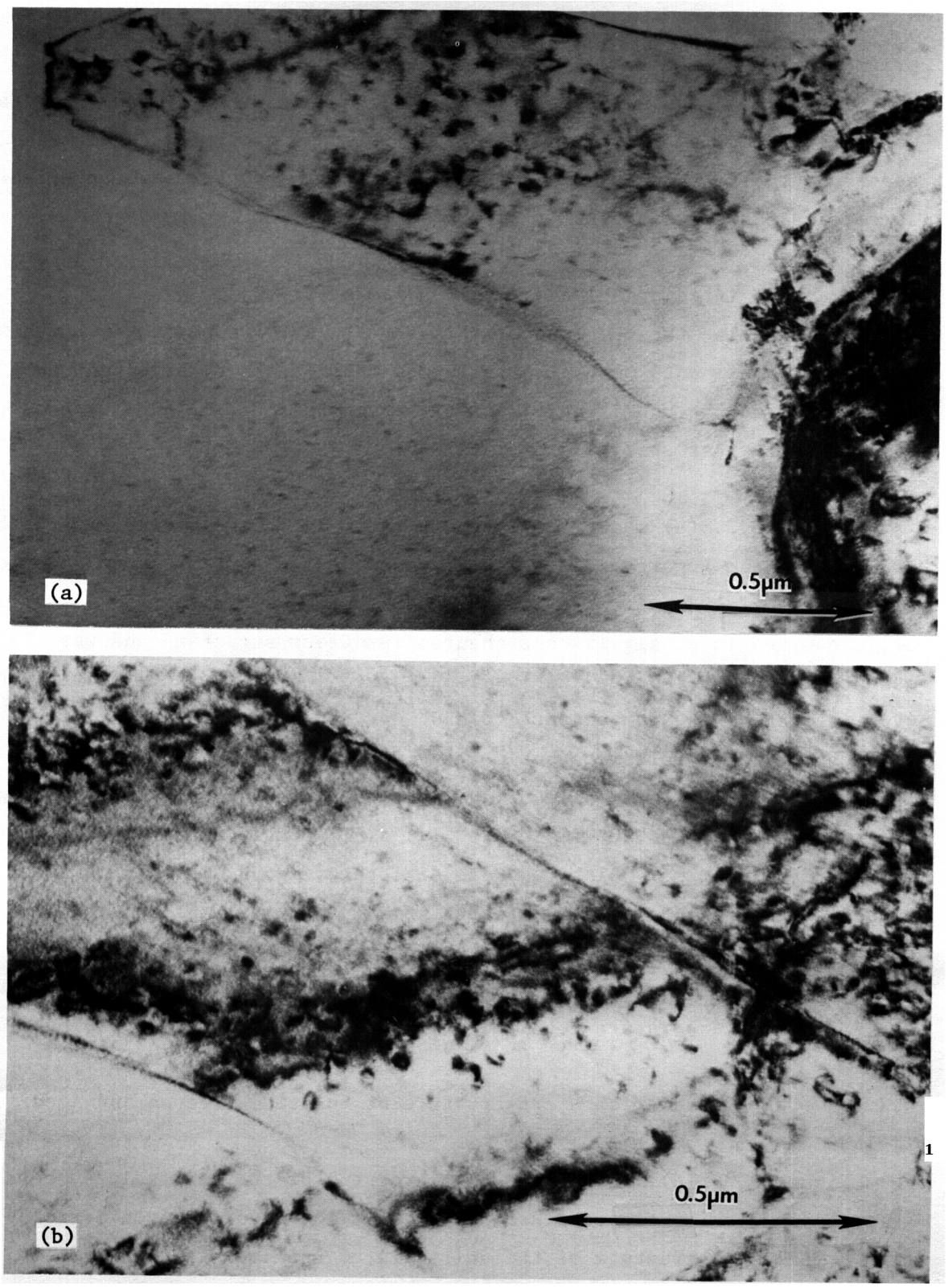

Figure 5.2.3 Microstructure of irradiated Ti–6242s after heating in electron microscope. (a) heated for 10 minutes at 525°C after irradiation. (b) heated for 10 minutes at 525°C and 10 minutes at 650°C after irradiation.

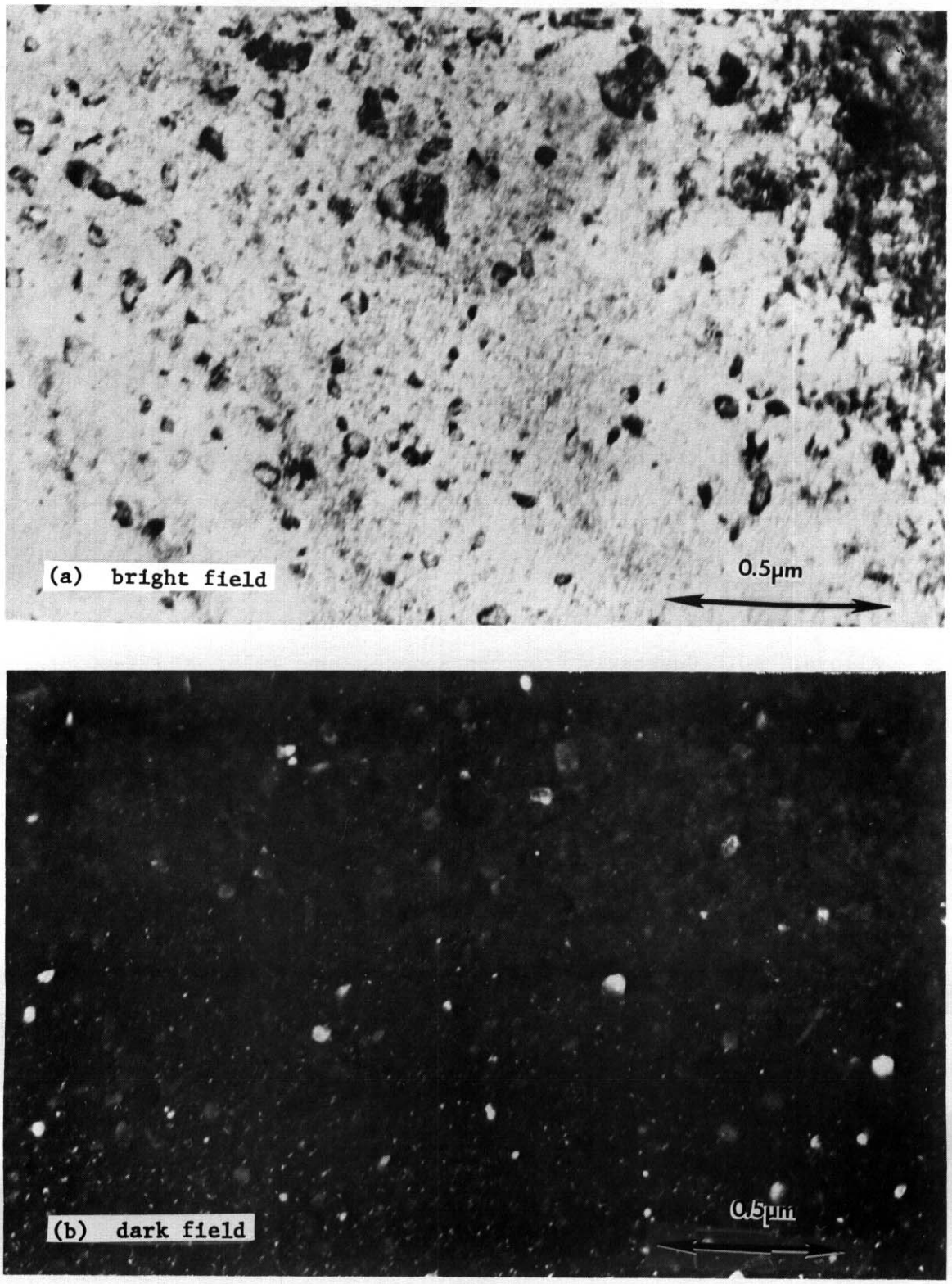

Figure 5.2.4 Microstructure of irradiated Ti-6242S after heating in an electron microscope for 10 minutes at 525°C, 10 minutes at 650°C, and 10 minutes at 750°C.

tendency towards a globular morphology, as seen at location "A" of Figure 5.2.5(b). The substructure in the beta phase consists of a high density of defect clusters and prismatic loops which are shown in location "B" of Figure 5.2.5(b). The details of the defect structure in the alpha phase were too fine to be resolved.

5.2.5 Future Work

During the next reporting period, the thermal stability of the radiation induced defect structure in Ti-6Al-4V, Ti-6242S, Ti-5621S and Ti-15-3 will be studied by vacuum annealing bulk samples of the irradiated alloys at various temperatures and monitoring the change in microhardness and microstructure.

5.2.6 References

1. R. E. Nygren, "Irradiation Induced Stress Relaxation in Titanium Alloys," ADIP Quarterly Progress Report, June 1978, DOE/ET-0058/2, pp. 106-116.
2. R. E. Nygren, E. K. Opperman, and R. W. Powell, "Irradiation Creep Studies of Titanium Alloys," presented at First Topical Meeting on Fusion Reactor Materials, Bal Harbour, Florida, January 1979, to be published in the Journal of Nuclear Materials.
3. S. M. L. Sastry, J. E. O'Neal, and J. W. Davis, "Comparison of Titanium Alloy Ti-6Al-4V and Ti-5621S Microstructures after EBR-II Irradiation," ADIP Quarterly Progress Report, December 1978, DOE/ET-0058/4, pp. 72-84.
4. J. W. Davis, S. M. L. Sastry, and L. J. Pionke, "Microstructure of Titanium Scoping Alloys Prior to Irradiation," ADIP Quarterly Progress Report, June 1978, DOE/ET-0058/2, pp. 85-99.
5. J. A. Sprague and F. A. Smidt, "The Microstructure of Ti-6242S Following Low-Fluence Neutron Irradiation at 400°C," ADIP Quarterly Progress Report, December 1978, DOE/ET-0058/4, pp. 67-71,

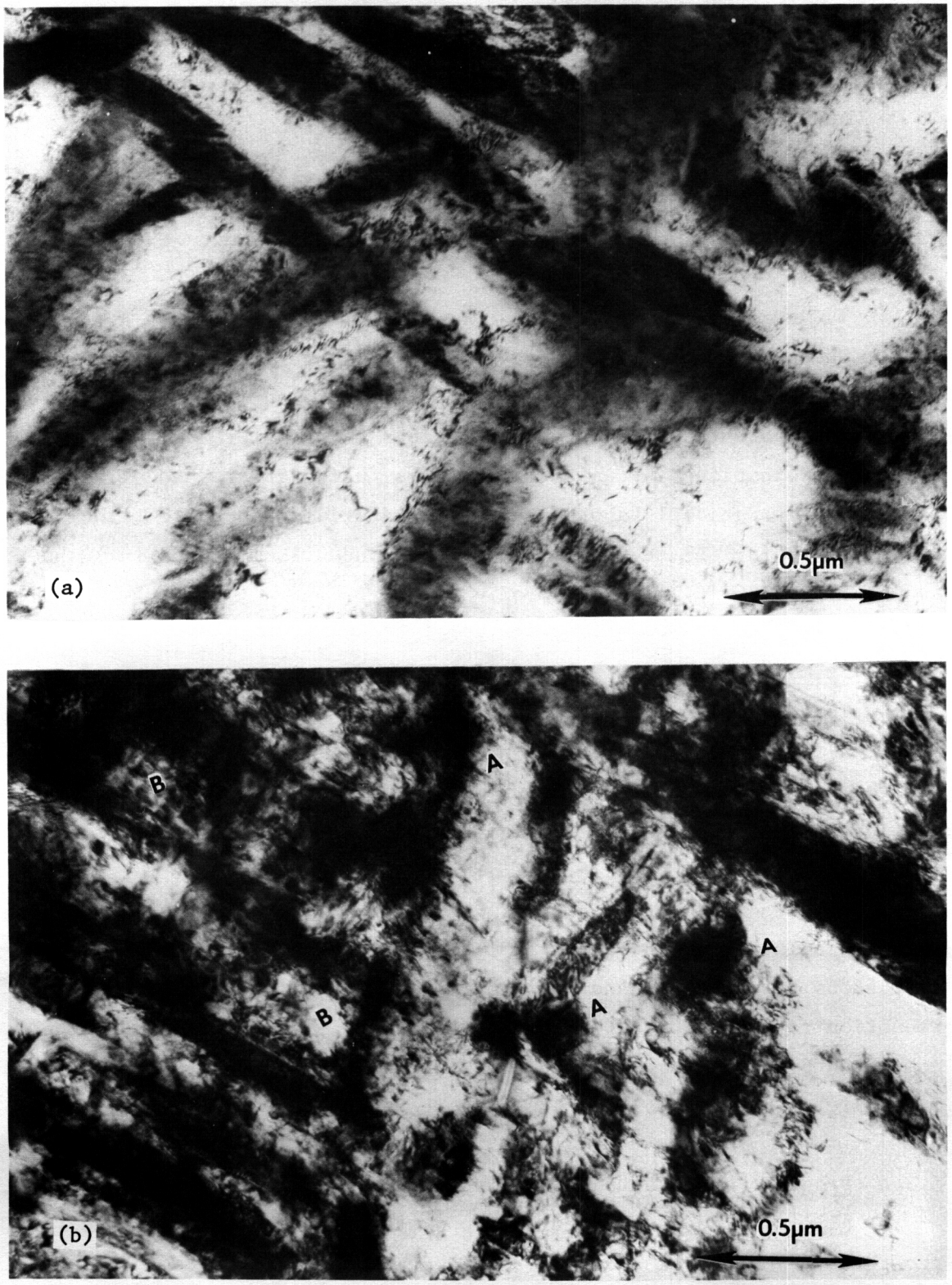

Figure 5.2.5 Microstructure of Solution treated and aged Ti-15-3. (a) solution treated for 15 minutes at 760°C and aged for 16 hours at 510°C. (b) irradiated to 2.1 dpa at 450°C.

long. Chemical analyses are being obtained for each of the ten (10) total second melt ingots. Analyses will be performed for both metallic solute contents and interstitial (carbon, oxygen, and nitrogen) levels.

One of each of the 20 cm long ingots will be cut in half to yield two 10 cm long extrusion billets. For each of the scoping alloys a total of three extrusions will be carried out. These are:

INGOT SIZE	EXTRUDE TO
8.6 cm Diam. x 20 cm long	Sheet Bar (∿ 5 cm x 1.9 cm)
8.6 cm Diam. x 10 cm long	Sheet Bar (∿ 5 cm x 1.9 cm)
8.6 cm Diam. x 10 cm long	Round Bar (∿ 2.5 cm Diam.)

All extrusions will be carried out at approximately 1200°C. The reduction ratios are about 6:1 for the sheet bar extrusions and about 11.4:1 for the round bar extrusions. All ingots will be canned in evacuated stainless steel cans for the extrusion process.

Extrusions will be carried out at the metalworking facility at the Oak Ridge National Laboratory. Current estimates of the schedule indicate this should be completed by about early May. Westinghouse has requested, and received, a no-cost extension of the period of performance of this project. Delivery to the Oak Ridge Fusion Materials Stockpile is now scheduled for mid-July. This extension was necessitated by a nine (9) week delay in the receipt of the starting material.

5.4 THE DUCTILITY IN BENDING OF MOLYBDENUM ALLOYS IRRADIATED BETWEEN 425 and 1000°C — F. W. Wiffen and B. L. Cox (ORNL)

5.4.1 ADIP Task

ADIP Task I.B.15, Tensile Properties of Reactive/Refractory Alloys.

5.4.2 Objectives

This work was directed at measuring the effect of elevated-temperature irradiation on the mechanical properties of molybdenum and molybdenum-base alloys. Small tab specimens were bend-tested over a range of test temperatures. Ductile-to-brittle transition temperatures (DBTT) were defined by the break or bend behavior in the test. Further refinement was provided by scanning electron microscopy of fracture surfaces on broken or cracked specimens.

5.4.3 Summary

Irradiation of Mo, Mo—0.5% Ti, and TZM at 425 to 1000°C to fluences producing 11 dpa resulted in DBTTs in bending above room temperature for all irradiation temperatures. The most severe embrittlement was a DBTT between 550 and 700°C produced by irradiation at 585°C. Alloying at the concentrations in the two alloys tested had a relatively minor effect on the DBTT. For the two most embrittling irradiations, at 585 and 790°C, the alloys had lower DBTTs than did the unalloyed Mo. This may be related to the alloying raising grain boundary decohesion stress. The DBTT shift with irradiation temperature could not be quantitatively related to the observed microstructures.

The increase in DBTT to above room temperature for all irradiation temperatures investigated suggests that molybdenum alloy structures could not survive a fusion reactor shutdown. Unless molybdenum alloys more resistant to irradiation embrittlement could be developed, it is unlikely that they could be used for a fusion reactor first wall.

5.4.4 Progress and Status

The major experimental results of this work, reported last quarter,[1] are summarized in Fig. 5.4.1. The experimental findings lead to the following observations:

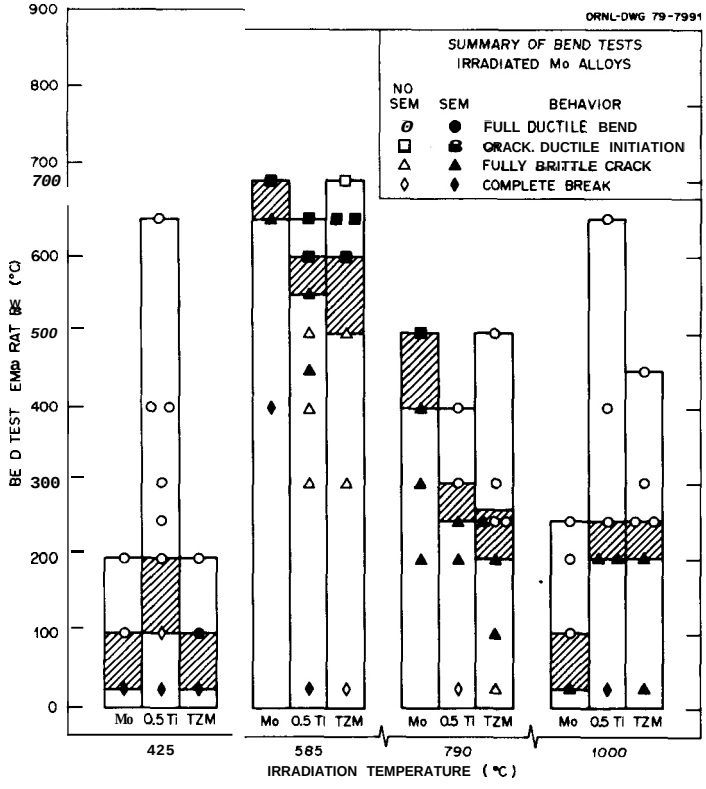

Fig. *5.4.1.* Summary Compilation of all the Bend Test Results for Three Molybdenum Alloys Irradiated at Four Temperatures. Open symbols indicate behavior determined by macroexamination only; filled symbols indicate scanning electron microscopy of the fracture surface. The shaded zone contains the DBTT.

1. The preirradiation DBTT is below room temperature for all three materials.

2. Differences in behavior of the three materials are smaller than differences due to irradiation conditions.

3. The shift in the DBTT is a strong function of the irradiation temperature.

4. For the available irradiation temperatures, the greatest degradation of properties was produced by the 585°C irradiation.

5. For all four irradiation temperatures and for all three materials, the DBTT is above room temperature.

6. For a single irradiation temperature, the fracture appearance changes from predominantly cleavage to mainly grain boundary separation and finally to ductile tearing as the test temperature is increased from below the DBTT to above the DBTT.

7. Molybdenum generally shows more grain boundary separation than Mo–0.5% Ti or TZM when tested at the same temperature, although there was some cleavage area in all brittle fractures.

5.4.4.1 Discussion and Comparison with Literature Results

The results show that irradiation temperature has a strong influence on the DBTT of irradiated molybdenum alloys, but that composition (within the range examined) has only a minor effect. For a fixed irradiation temperature, the fracture mode can include a combination of cleavage, grain boundary separation, and ductile dimple fractures. Cleavage is predominant at the lowest temperatures, grain decohesion at the intermediate temperatures, and ductile failure at the highest temperatures.

The criterion used to define brittle failure in this work is far less restrictive than in many other investigations. In this work, a test that resulted in a crack, but with some ductile failure at the tensile face of the fracture, was defined as being above the DBTT. In contrast, Webster et al.[2] defined specimen fracture in a tensile test with less than 50% reduction of area as brittle behavior. This type of difference in definition of "brittle fracture" and the many other experimental differences make comparison of the present results with the few available published results difficult.

Results for the two lowest irradiation temperatures indicate a very strong irradiation temperature dependence of the DBTT in this range: irradiation at 425°C produced DBTTs in the range from 50 to 200°C, but irradiation at 585°C shifted the DBTT to above 550°C. Tensile tests[3] on rod specimens from this same irradiation experiment showed that for a strain rate of 3×10^{-4}/s irradiation at about 450°C resulted in a DBTT between 550 and 650°C. Since the two test types are quite different, this result is within the range defined in the current experiments and also suggests that the dependence on irradiation temperature may be strongest in the 400 to 500°C range. Only two rod specimens of molybdenum from the earlier experiment had been irradiated at a higher temperature. These samples were irradiated at about 1000°C; the two tensile tests showed the DBTT to be above 22°C but below 400°C, which is also consistent with the current results.

Webster et al.[2] tensile tested samples of irradiated molybdenum and TZM at room temperature and at the irradiation temperature for irradiation temperatures of 465 to 680°C. They reported brittle failures for all tests at room temperature, with elongation less than 0.4% in all cases and too small to measure in most cases. They inferred DBTTs in the range from 450 to 720°C for various test and material conditions. The current results agree approximately with those results, but detailed comparison is not possible because of the differences in definition of DBTT and because Webster et al. tested only at the irradiation temperature. Their irradiations were also for fluences well below ours.

All the specimens in this experiment had a fully recrystallized microstructure before irradiation. This undoubtedly had a major influence on the high amount of grain boundary separation in many of the brittle failures but probably is not a determining factor between ductile or brittle behavior. Since there was an appreciable fraction of cleavage fracture, even in failures that were mainly by grain separation, strengthening or elimination of grain boundaries could have raised the fracture stress in a given test, but would not have restored ductile fracture. Webster's[2] results indicated a similar effect. Recrystallized molybdenum and TZM failed by intergranular separation but cold-worked or stress-relievei specimens failed by transgranular cleavage. The DBTT appeared to be relatively insensitive to fracture mode for these two brittle modes.

The effect of test temperature on the fracture mode suggests that, while the cleavage stress is relatively temperature independent, the grain boundary decohesion stress decreases with increasing temperature and drops below the cleavage stress over the testing range. The three fracture modes can be understood in terms of the modified Ludwig-Davidenkov diagram shown schematically in Fig. 5.4.2. At the lowest temperatures the cleavage stress is the lower of the three stresses shown, and cleavage is the predominant failure mode. At increasingly higher test temperatures, the grain boundary decohesion stress drops below the cleavage stress and failure is initiated by the separation of the most highly stressed grain boundaries. The fracture progresses

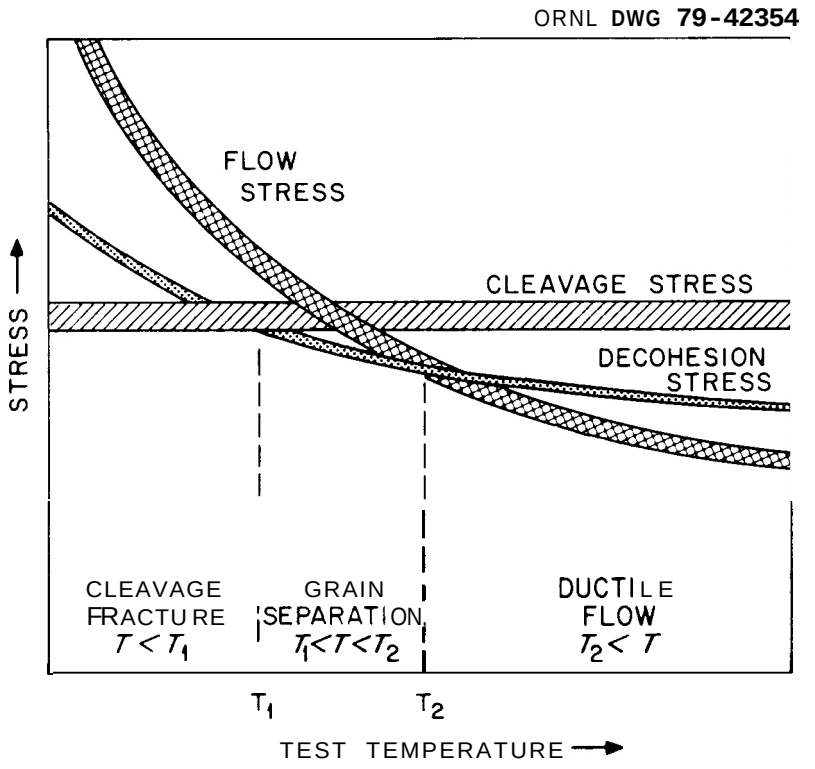

Fig. 5.4.2. Schematic Ludwig–Davidenkov Diagram, with Grain Boundary Decohesion Stress Added. The test temperature T_2 is the DBTT; T_1 is the boundary between cleavage and decohesion failure modes.

through connected separation of grain boundaries appropriately oriented, with cleavage failures through some grains to connect the opening boundaries. At still higher test temperatures the flow stress is lower than either of the brittle failure mode stresses and the sample deforms. The deforming sample may then either work harden to the cleavage stress, and brittle fracture will occur, or it may deform to produce fully ductile failure.

The cleavage stress of molybdenum and molybdenum alloys is little affected by irradiation.[5] The decohesion strength is assumed to be only weakly temperature dependent, is probably raised by alloying, and may be sensitive to irradiation. The flow stress is markedly increased by irradiation.

Irradiation temperature thus affects the DBTT through the effectiveness of the matrix hardening produced at each temperature. Hence, raising the flow stress increases the intersection with the brittle

fracture stresses to higher temperatures, thus raising the DBTT (Fig. 5.4.2). The DBTT shifts measured in these experiments can only be qualitatively related to the previously reported microstructural features in these same samples. The highest void concentration was found[4] after the irradiation at 585°C, with void concentrations decreasing in the order 425, 790, and 1000°C. The highest DBTT corresponds to the highest void density, but the other DBTT results do not correlate with observed void concentrations. The dominant microstructural feature after irradiation at 425°C was the very high concentration of small dislocation loops. The susceptibility of this microstructure to deformation by channeling, with high local ductility,[3] is probably related to the DBTT being lower after 425°C irradiation than after 585°C irradiation, where void hardening predominates. Void concentration differences among the three materials at any one irradiation temperature also do not correlate with the DBTT results. The other microstructural components that strengthen the matrix are dislocation loops and dislocation networks. These microstructural features were described only qualitatively. The dislocation density decreased with increasing irradiation temperature and was higher in the two alloys than in the molybdenum. Loop concentrations after 425 and 585°C irradiation were too high to measure and would be expected to provide the major part of the strengthening.

The differences in fracture mode between the molybdenum and the two alloys suggests that alloying has raised the decohesion strength relative to that of unalloyed molybdenum. The cleavage stress in molybdenum and Mo–0.5% Ti was previously found[3] to be almost identical and essentially independent of temperature.

5.4.5 Future Work

This work is complete. No future work or further reporting is planned.

5.4.6 References

1. B. L. Cox and F. W. Wiffen, "The Ductility in Bending of Molybdenum Alloys Irradiated Between 425 and 1000°C," *ADIP Program Quart. Prog. Rep. Dec. 31, 1978*, DOE/ET-0058/4, pp. 84-98.

2. T. W. Webster, B. L. Eyre, and E. A. Terry, "The Effect of Fast Neutron Irradiation on the Structure and Tensile Properties of Molybdenum and TZM," pp. 61-80 in *Irradiation Embrittlement and Creep in Fuel Cladding and Core Components*, British Nuclear Energy Society, London, 1972.

3. F. W. Wiffen, "The Tensile Properties of Fast Reactor Neutron Irradiated BCC Metals and Alloys," pp. 176-97 in *Defects and Defect Clusters in B.C.C. Metals and Their Alloys, Nucl. Met.* 18 (Proc. 1973 Int. Conf. Aug. 14-16, 1973), R. J. Arsenault, ed., National Bureau of Standards, Gaithersburg, Maryland.

4. J. Bentley and F. W. Wiffen, "Neutron Irradiation Effects on Molybdenum and Molybdenum Alloys," pp. 209-18 in *Proc. 2nd Top. Meet. Technol. Controlled Nucl. Fusion* (Sept. 21-23, 1976, Richland, Washington) Vol. I, G. L. Kulcinski and N. M. Burleigh, eds., CONF-760935 - Part 1.

5.5 MECHANICAL PROPERTY TESTING OF UNIRRADIATED PATH C ALLOYS — K. C. Liu (ORNL)

5.5.1 ADIP Task

ADIP Task I.B.3, Fatigue Crack Growth in Reactive and Refractory Alloys.

5.5.2 Objective

Fatigue and crack growth behavior are among the most important properties of an alloy to be used in a fusion reactor. There is essentially no information on these properties for refractory metal alloys. The objective of this work is to develop base-line information for the Path C refractory metal scoping alloys in the unirradiated condition.

5.5.3 Summary

A closed-loop controlled servohydraulic testing system has been assembled and checked out for conducting tensile, fatigue, and crack growth tests at elevated temperatures. A set of axial strain extensometers specifically designed for miniature sheet specimens has been developed for testing under high vacuum at elevated temperatures.

5.5.4 Progress and Status

A multipurpose material testing system with closed-loop servo-control features, as described in an earlier progress report,' has been assembled, checked out, and put into operating condition. A set of special grips was designed for use in vacuum and is adaptable to either sheet or rod specimens tested at elevated temperatures. Heating for elevated-temperature tests is accomplished with an induction heating generator.

A vacuum system has been designed for use with the special grips and is being constructed by a commercial vacuum product firm. The chamber will be pumped by a cryogenic vacuum pump capable of pressure below 0.1 μPa. The supplier has delayed delivery of the system from December 1978 promised on the bid to the end of May 1979.

A few preliminary tests using sheet fatigue specimens with Grodzinski fillets made of stainless steel were performed at temperatures up to 750°C. Lack of an appropriate environmental chamber in the testing system was the reason not to use specimens made of refractory metal alloys in these tests. An examination of test results indicates that the testing system is performing at its optimum condition.

The outcome of experiments using miniature specimens is sensitive to the accuracy and methods of strain measurement used. For tests using hourglass rod specimens, a diametral strain extensometer will be used. However, tests using Grodzinski specimens with a constant-width gage section require axial strain extensometers. A short-stroke axial strain extensometer was designed and fabricated for use in the system checkout tests. The limit is ±10% strain. Tensile tests require a long-stroke axial strain extensometer. A new design capable of accurately measuring a relative displacement in excess of 10 mm (0.4 in.) across an axial gage length of 12.7 mm (0.50 in.) is being fabricated. Use of the extensometer beyond the design strain range is permissible provided the strains exceeding the limit are properly extrapolated with correction factors.

Details of the apparatus development and experimental techniques will be summarized in a topical report.

5.5.5 Future Work

Miniature central crack tension specimens similar to those specified in ASTM E 338-67 are being considered for fatigue crack growth studies. A preliminary test will be performed with use of visual methods of crack extension measurement. Unless the induction heating used in the test system is a restriction, dc potential techniques[2,3] will be used with the direct optical method.

5.5.6 References

1. K. C. Liu, "Mechanical Property Testing of Path C Alloys in Unirradiated Condition," *ADIP Quart. Prog. Rep. January–March* 1978, DOE/ET-0058/1, pp. 153–56.

2. **G. J. Lloyd,** *On the Use of Electrical Analogues in Crack Propagation Experiments,* TRG-Report-2818(R) **(March 1976).**

3. **J. L. Straalsund and D. A. Mervyn, "Adaptation of an Electrical Potential Technique to Measure Fatigue Crack Growth,"** *ADIP Quart. Prog. Rep. October–December 1978,* **DOE/ET-0058/4, pp. 4-9.**

6. PATH D ALLOY DEVELOPMENT — INNOVATIVE MATERIAL CONCEPTS

Innovative material concepts are included as a path in the alloy development program because the fusion reactor environment is extremely demanding on materials in the high-flux region and the more conventional materials and metallurgical concepts may not be adequate. Novel approaches to alloy design, nonconventional material processing to tailor properties, or alternate materials such as structural ceramics and fiber composites will be considered.

7. STATUS OF IRRADIATION EXPERIMENTS

Irradiation experiments are presently being conducted in the ORR and HFIR, which are mixed-spectrum fission reactors, and in the EBR-II, which is a fast-spectrum reactor. Experiments are generally cooperative between several program participants. Experiment plans, test matrices, etc., are reviewed by the Alloy Development for Irradiation Performance Task Group.

7.1 IRRADIATION EXPERIMENT STATUS AND SCHEDULE

The following charts show the irradiation experiment schedule, including experiments completed, in progress, and planned. Experiments are presently under way in the ORR and HFIR, which are mixed-spectrum reactors, and the EBR-II, a fast reactor.

EBR-II subassembly X 287 was received at ORNL and will be disassembled early in the next quarter.

ORR-MFE-II was removed from the reactor on November 27 because a small pinhole leak developed in a weld in the experiment containment. Hardware necessary for remote repair of the weld was developed during December. The capsule is expected to be repaired and reinstalled in the reactor by May 1, 1979. While the MFE-II was out of the reactor, a dosimetry experiment was conducted. Results from this experiment are being analyzed at the present time. This dosimetry experiment had been previously assembled and was awaiting a convenient time for irradiation.

Irradiation and disassembly of HFIR-CTR-23 containing hourglass specimens of Nimonic PE-16 will be completed by early May, and specimens will be available for fatigue testing.

Experiment HFIR-CTR-24 was removed from the reactor in December. Disassembly is complete. This experiment was basically a temperature calibration experiment, containing passive temperature monitors (melt wires, SiC, Mo for postirradiation recovery experiments). Evaluation is in progress.

Experiment Designation	Major Objective
A. Oak Ridge Research Reactor	
ORR-MFE-1	Experiments to scope the effects of composition and microstructure on the tensile, fatigue, and irradiation creep of representative path A, B, and C alloys.
ORR-MFE-2	
ORR-MFE-3	Effects of irradiation on postirradiation fatigue crack growth in representative path A, B, and C alloys.
ORR-MFE-4	Effect of irradiation on tensile, fatigue, and irradiation creep of path A PCA (Prime Candidate Alloy) and path B base research alloys. Spectral tailoring to maintain correct He/dpa ratio. Irradiation on continuing basis.

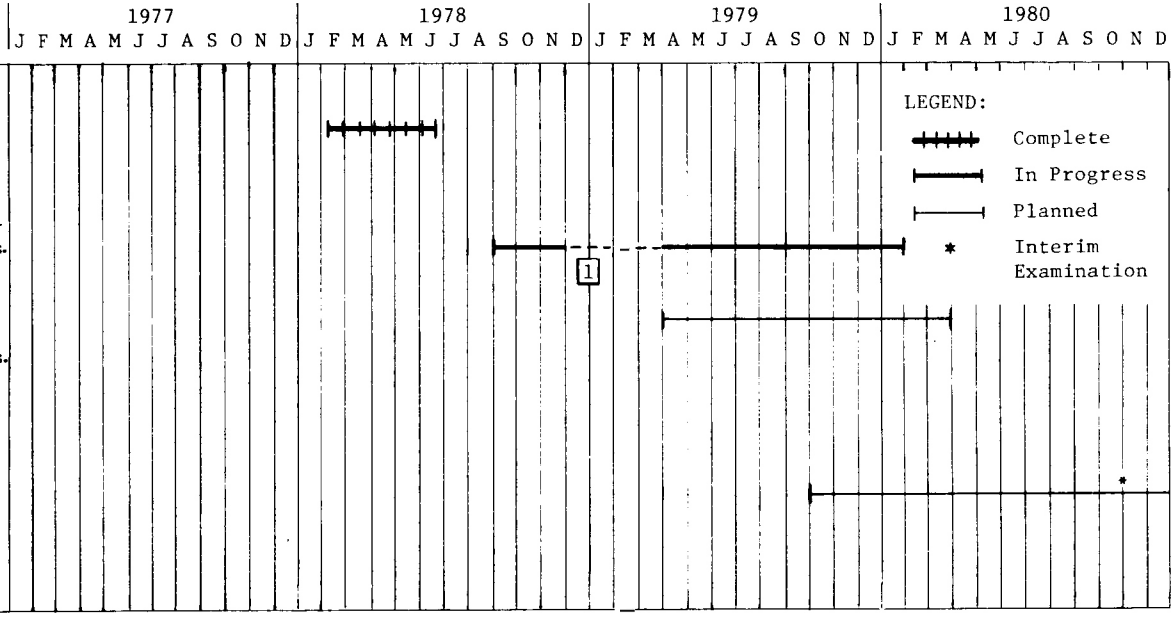

[1] MFE-2 was removed from the ORR on Nov. 29, 1978, to repair a small helium leak in the experiment containment. It is anticipated that the experiment will be reinstalled in the reactor during the latter part of April 1979. While the experiment was out of the reactor a dosimetry experiment was performed with core configuration as with MFE-2.

Experiment Designation	Major Objective
ORR-MFE-5	In-reactor fatigue crack growth experiment
B Experimental Breeder Reactor II	
S Subassembly X 264	Effect of preinjected helium (2–200 at. ppm) on microstructure and tensile properties of 316 SS, PE-16, V and Nb alloys. Fluence $\leq 2.3 \times 10^{26}$ n/m^2, 500–825°C.
Subassembly X 287	Effect of preinjected helium (2–200 at. ppm He) on microstructure and tensile properties of 316 SS, PE-16, V and Nb alloys. Fluence $\leq 4 \times 10^{26}$ n/m^2, 400–700°C.
Subassembly X 217D	Stress relaxation Ti Alloys
See footnotes [1] [2] and [3]	Effect of irradiation on swelling, tensile, fatigue, and crack growth properties of Ti scoping alloys. 370, 450, and 550°C, fluence 4.5–5.5 × 10^{26} n/m^2.

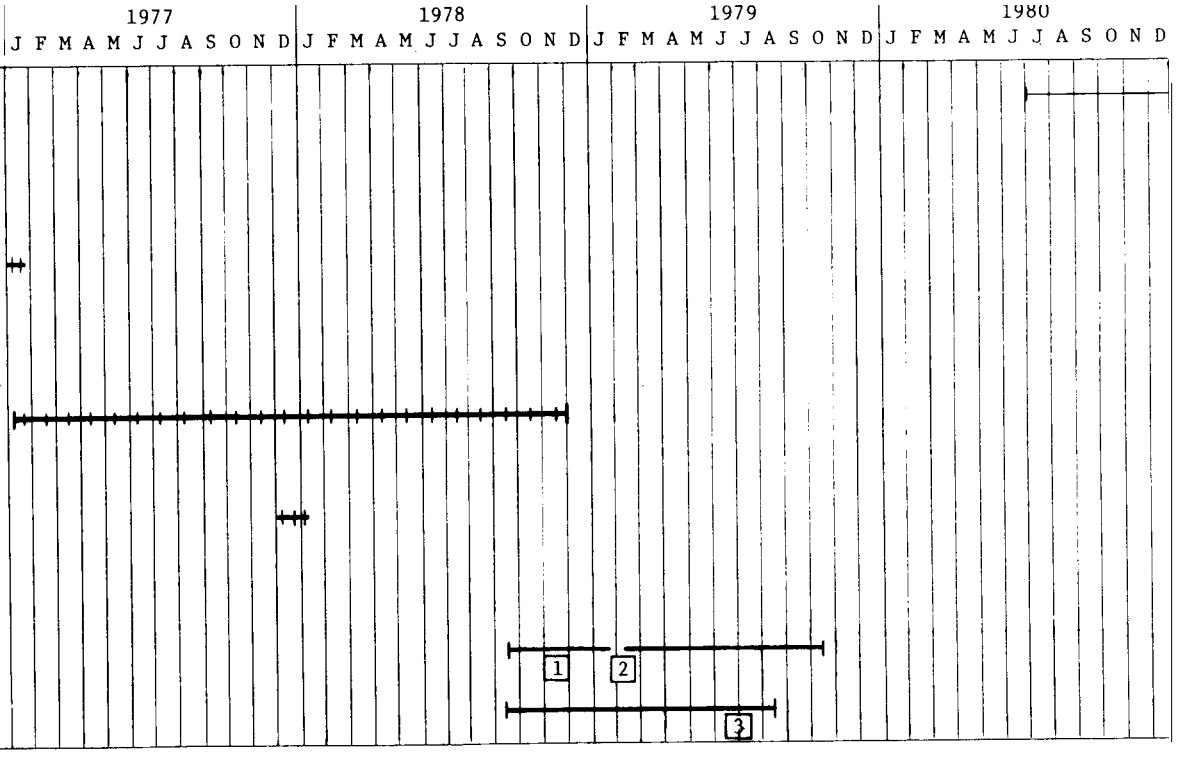

[1] EBR-II, row 2, pins B285 and B286.

[2] Subassembly removed for EBR-II run 99.

[3] Pin B284, row 2 for runs 96–98; row 4 for runs 100–102

Experiment Designation	Major Objective
Experiment plan depends on alloy availability. EBR-II space not yet identified.	Effect of Irradiation on swelling, tensile, fatigue, and crack growth properties of V and Nb scoping alloys. 370, 450, 550, and 650°C. Position in reactor not finalized, therefore no fluence estimate.
C. High Flux Isotope Reactor (HFIR)	
HFIR-CTR-6	PE-16 for swelling and tensile properties, 300–700°C 2.2–4.5 dpa, 100–350 at. ppm He
HFIR-CTR-7	PE-16 for swelling and tensile properties, 300–700°C 9–18 dpa, 1250–3000 at. ppm He
HFIR-CTR-8	duplicate of -7
HFIR-CTR-9	316 and 316 + Ti for swelling and tensile properties, 280–680°C, 9–18 dpa, 400–1000 at. ppm He

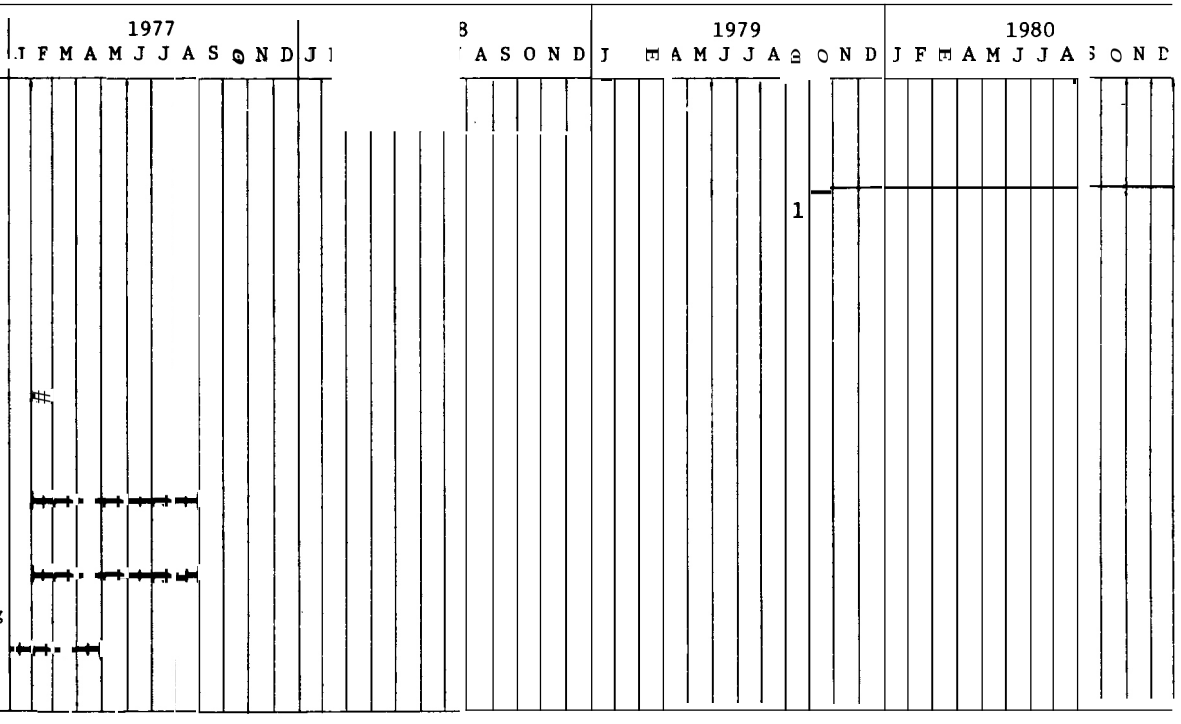

[1] Earliest date irradiations can begin on present alloy development schedule.

Experiment Designation	Major Objective
HFIR-CTR-10	duplicate of -9
HFIR-CTR-11	
HFIR-CTR-12	316 and 316 + Ti for swelling and tensile properties, 280–680°C, 5.5–11 dpa, 200–500 at. ppm He
HFIR-CTR-13	duplicate of -12
HFIR-CTR-14	20%-CW 316 for fatigue testing 300°C. 9–18 dpa, 400–1000 at. ppm He
HFIR-CTR-15	20%-CW 316 for fatigue testing 500°C, 5.5–11 dpa, 200–500 at. ppm He
HFIR-CTR-16	316, welds, PE-16, and Inconel 600 for swelling and tensile properties, ~55°C, 5.5–11 dpa, 150–2700 at. ppm He (depending on alloy)
HFIR-CTR-17	Type 316 welded with 16-8-2 filler metal for tensile properties and failure analysis, 280–620°C, 6.7–13 dpa, 180–460 at. ppm He in weld metal

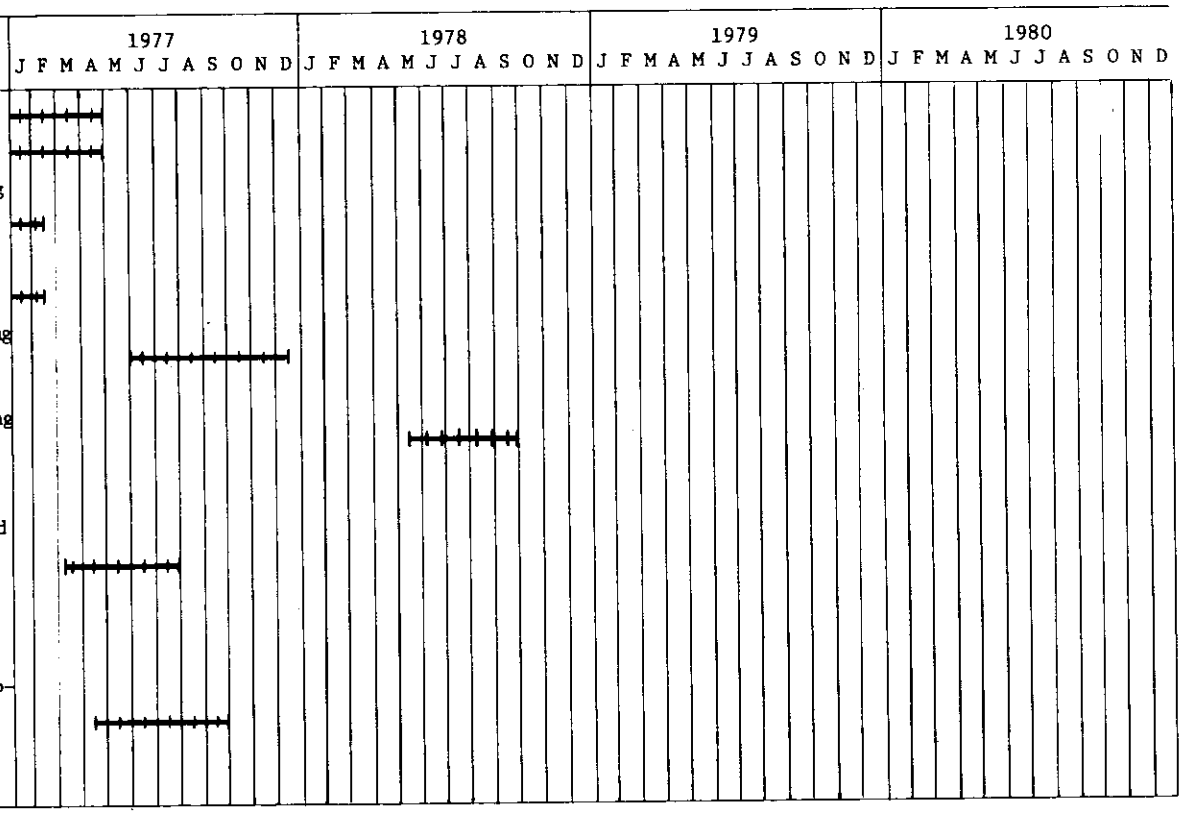

Experiment Designation	Major Objective
HFIR-CTR-18	PE-16 and 20%-CW type 316 for swelling and tensile properties, 280–700°C, PE-16: 17–27 dpa, 3400–5600 at. ppm He 316: 27–34 dpa, 1600–2100 at. ppm He
HFIR-CTR-19	316 welded with 316 filler metal for tensile properties, 280–620°C, 5.5–11 dpa, 200–500 at. ppm He
HFIR-CTR-20	20%-CW 316 for fatigue testing, 300°C, 5.5–11 dpa, 200–500 at. ppm He
HFIR-CTR-21	20%-CW 316 for fatigue testing, 500°C, 9–18 dpa, 400–1000 at. ppm He
HFIR-CTR-22	Duplicate of -20
HFIR-CTR-23	PE-16 for fatigue testing, 300°C, 4 4–9 dpa, 370–1000 at. ppm He

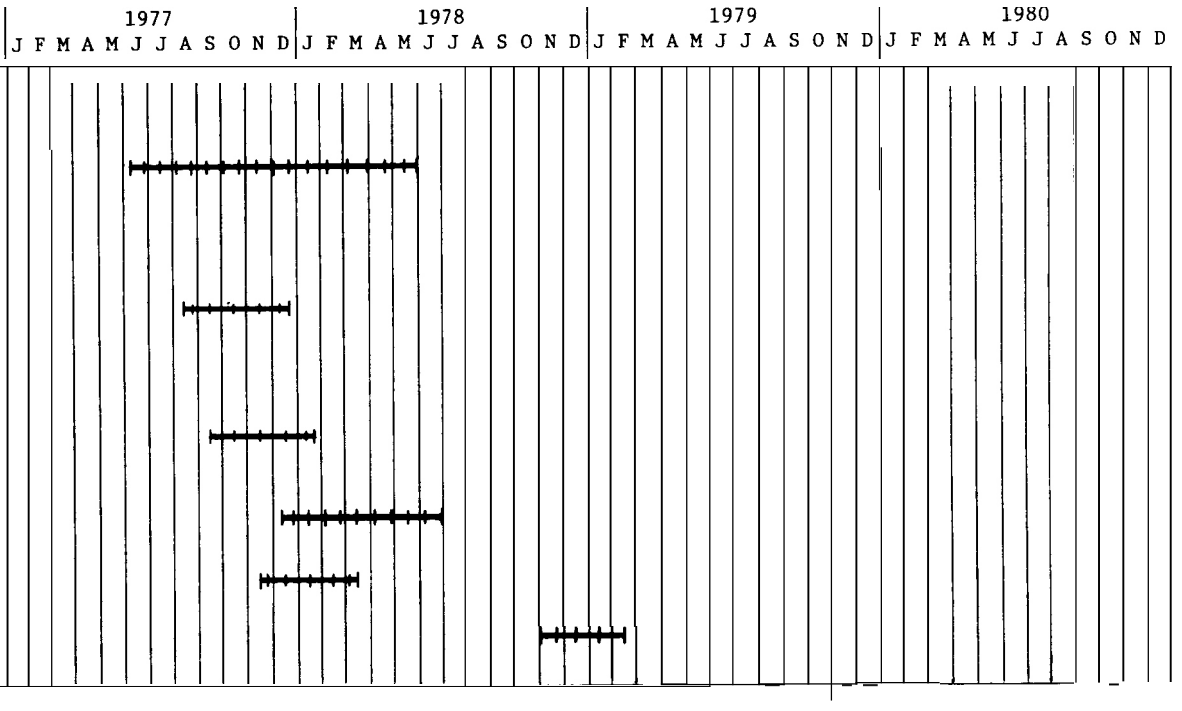

Experiment Designation	Major Objective
HFIR-CTR-24	Temperature calibration, tensile properties of MFE Ref. 316, 2.25 dpa, 30 at. ppm He
HFIR-CTR-25	Temperature calibration, tensile properties of MFE Ref. 316, 2.25 dpa, 30 at. ppm He
HFIR-CTR-26	Swelling and tensile properties of MFE Ref. 316, 32 dpa, 1900 at. ppm He
HFIR-CTR-27	Swelling and tensile properties of MFE Ref. 316, 56 dpa, 3450 at. ppm He
HFIR-CTR-28	Swelling and tensile properties of MFE Ref. 316, 32 dpa, 1900 at. ppm He
HFIR-CTR-29	Swelling and tensile properties of MFE Ref. 316, 56 dpa, 3450 at. ppm He
HFIR-CTR-30[a]	Swelling and tensile properties, Path A PCA microstructural variations, 40 dpa, 2500 at. ppm He
HFIR-CTR-31[b]	Swelling and tensile properties, Path B PCA microstructural variations

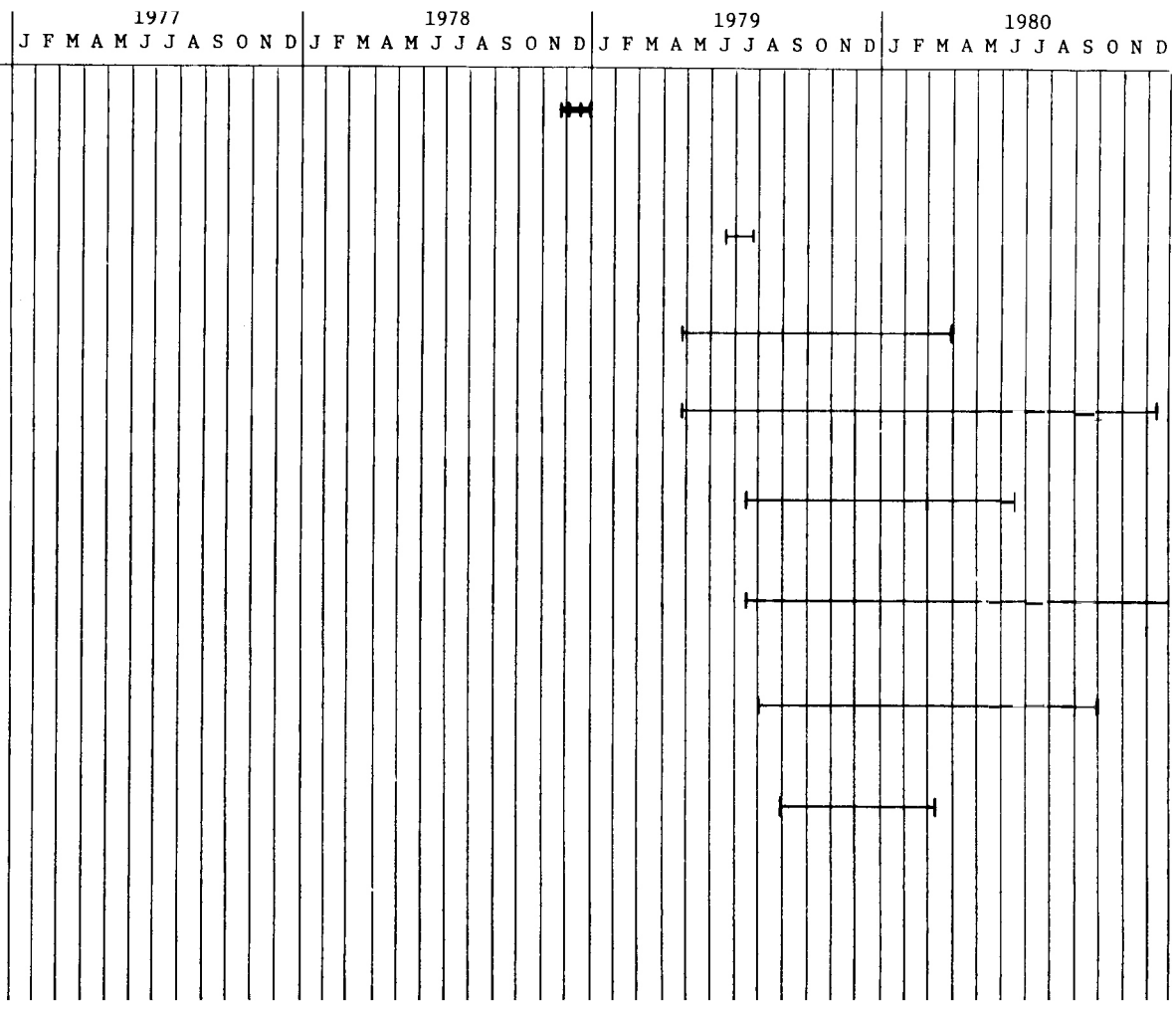

[a] Assumed 18 cycles for planning.

[b] Assumed 8 cycles for planning.

7.2 ETM RESEARCH MATERIALS INVENTORY — F. W. Wiffen, T. K. Roche (GRNL), and J. W. Davis (McDonnell Douglas)

7.2.1 ADIP Task

ADIP Task I.D.1, Materials Stockpile for MFE Programs.

7.2.2 Purpose and Scope

The Office of Fusion Energy (ETM) of the Department of Energy has assigned program responsibility to ORNL for the establishment and operation of a central inventory of research materials to be used in the Fusion Reactor Materials research and development programs of the DOE. The primary objective is to provide a common supply of materials for use in the nationally coordinated Fusion Reactor Materials Program. This will minimize unintended materials variables and provide for economy in procurement and for centralized recordkeeping. Initially this inventory is to focus on materials related to first wall and structural applications and related research, but various special-purpose materials may be added in the future. It is recognized that materials supplementary to this inventory will be introduced to the ETM programs from time to time, and records of those materials shall be made available to ORNL and incorporated in the records of the ETM Research Materials Inventory.

The use of materials from this inventory for research that is coordinated with or otherwise related technically to the Fusion Reactor Materials Program of DOE but which is not an integral or directly funded part of it is encouraged, with the understanding that the results of such research be made available to the Fusion Reactor Materials Program.

7.2.3 Materials Requests and Release

Materials requests must provide a statement of the programmatic end use and agreement that characterization information developed by the user shall be supplied to the inventory records. Requests for materials shall be directed to ETM Research Materials Inventory at ORNL (Attention: F. W. Wiffen). Materials will be released directly if:

(a) The material is to be used for programs funded by ETM, with goals consistent: with the approved Materials Program Plans of the Materials and Radiation Effects Branch.

(b) The requested amount of material is available, without compromising other intended uses.

Materials requests that do not satisfy both (a) and (b) will be discussed with the staff of the Materials and Radiation Effects Branch, Office of Fusion Energy, for agreement on action.

7.2.4 Records

Chemistry and materials preparation records are maintained for all inventory material. All materials supplied to program users will be accompanied by summary characterization information.

7.2.5 Summary of Current Inventory (March 1979)

7.2.5.1 Path A Alloys

1. Reference alloy – 20%-cold-worked type 316 stainless steel. Plate, rod, and 0.180-in.-diam tubing are in stock. Rework will be scheduled as required.
2. Prime Candidate Alloy (PCA) (Fe—16 Ni— 14 Cr-2 Mo—Mn, Ti, Si, C). All the PCA has been delivered to ORNL by the vendor, Teledyne Allvac. Table 7.2.1 lists the product forms in stock.
3. PCA tube production and remelt for composition variation is planned for late FY 1979.

7.2.5.2 Path B Alloys

4. A reference heat of PE-16 is in stock at ORNL. Plate, rod, and 0.180-in.-diam tubing are available.
5. Base Research Alloys

Alloy	Ni	Cr	Mo	Nb	Ti	Al	Si
B-1	25	10	1		3	1.5	0.3
B-2	40	12	3		1.5	1.5	0.3
B-3	30	12		2	2	0.5	0.3
B-4	40	12		3	1.8	0.3	0.3
B-6	75	15		1	2.5	1.5	0.3

Table 7.2.1. Material Receipts into the ETM Research Materials Inventory[a]

Alloy	Heat	Product Form[b]	Dimensions		Quantity				
			(mm)	(in.)	(kg)	(lb)	(m)	(ft)	(pieces)
Path A PCA	K-280	RCS bar	130	5					1[c]
		Round bar	100	4	417	920			
		Round bar	83	1 5/16	74	164	11	35	
		Round bar	52.06	0 475	63	138	69	227	
		Plate	13 × 130	1/2 × 5	70	154	4.6	15	
Path B BRA									
B-1	J-270	RCS bar	100	4	93	204			2
	J-271	RCS bar	100	4	91	200			2
B-2	J-268	RCS bar	100	4	98	217			2
	J-269	RCS bar	100	4	99	219			2
B-3	J-266	RCS bar	100	4	92	202			2
	J-267	RCS bar	100	4	93	204			2
B-4	J-264	RCS bar	100	4	92	202			2
	J-265	RCS bar	100	4	93	204			2
B-6	J-262	RCS bar	100	4	89	197			2
	J-263	RCS bar	100	4	83	184			2

[a] All from vendor Teledyne Allvac

[b] RCS = round-corner square.

[c] One 13-mm (1/2-in.) slice from bar

Two 140-kg (300-lb) heats of each alloy were purchased from Teledyne Allvac. This material was delivered to ORNL in September 1978, and the yield was approximately 180 kg *(400* lb) per alloy.

Secondary breakdown has begun. A single sheet bar and a rod have been extruded from each of the five alloys, and the material is being used to determine thermomechanical treatment to produce final product form.

Table 7.2.1 lists the available primary product forms of the five alloys. Chemical analysis and metallography of each alloy are given in Sect. 4.2 of this report.

7.2.5.3 Path C Alloys (Refractory Alloys)

6. Small amounts of several niobium- and vanadium-base alloys are currently available at ORNL. Quantity and product forms are limited.
7. An order has been placed for the purchase of approximately 6 kg each of five alloys. Only sheet and rod will be produced.

   Alloys: Nb—1% Zr
   Nb—5% Mo—1% Zr
   V—20% Ti
   V—15% Cr—5% Ti
   V—9% Cr—3.3% Fe—1.3% Zr—0.05% C (Vanstar 7)

   Delivery of material is expected in the late summer of 1979.

7.2.5.4 Path C Alloys (Reactive Alloys)

8. The titanium-base scoping alloys have the following compositions, wt %:

Alloy	Al	V	Mb	Zr	Sn	Cr	Si
Ti-64	6	4					
Ti-6242S	6		2	4	2		0.09
Ti-5621S	5		1	2	6		0.25
Ti-38644	3	8	*4*	4		6	

At least 0.75 m^2 (1200 $in.^2$) of each of these alloys is currently available in 0.76-mm (0.030-in.) thickness. This sheet is from the same heat as material currently in reactor experiments. Larger section sheet of alloy Ti-5621S is also available.

Orders are now being developed to purchase new stocks of these alloys in several product forms. Delivery dates have not yet been determined.

The titanium-base alloys are stored at McDonnell Douglas. However, inventory control and materials release are handled by ORNL, and requests should be addressed to ORNL.

8. CORROSION TESTING AND HYDROGEN PERMEATION STUDIES

Corrosion, erosion, and mass transfer are processes that may degrade mechanical properties, alter heat transfer characteristics of heat transport systems, and present maintenance problems when radioactive nuclides are involved. The importance of hydrogen permeation and the behavior of hydrogen in the alloy systems under development is clear from consideration of tritium inventory, containment, etc. In the early stages of the development program, base-line information is required to define compatible or noncompatible alloy systems and coolants. As optimized alloys are developed, more detailed data on effects of adjustments in alloy composition or structure may be required. Extensive engineering compatibility data will be required on the final optimized alloys.

8.1 HYDROGEN DISSOLUTION AND PERMEATION CHARACTERISTICS OF TITANIUM-BASE ALLOYS - E. H. Van Deventer, E. Veleckis and V. A. Maroni (Argonne National Laboratory).

8.1.1 ADIP Task

I.A.4. Hydrogen Dissolution and Permeation Effects. The results presented in this section contribute to Subtask I.A.4., Milestones I.A.b. and I.A.c.

8.1.2 Objective

The objective of the work reported in this section is to provide base-line hydrogen dissolution and permeation data for the group of titanium-base alloys currently under examination as part of the ADIP Path C alloy development activities. The hydrogen dissolution, outgassing and permeation characteristics of this family of materials is vital to an understanding of their performance as first-wall and blanket structural materials for fusion devices, A further objective of this work is to begin examining methods for overcoming any serious hydrogen isotope uptake and migration problems associated with the rather strong hydride-forming nature of titanium and its alloys,

8.1.3 Summary

Hydrogen dissolution in pure Ti-6Al-4V and the hydrogen permeation characteristics of an ion-nitride coated sample of Ti-6Al-4V have been evaluated. The permeability of the coated sample was at most ten times lower than had been observed for uncoated Ti-6Al-4V in the temperature range from 350 to 550°C. The solubility parameter for pure Ti-6Al-4V (Sieverts' constant) ranged from 360 wppm $H/torr^{1/2}$ at 500°C to 1600 wppm $H/torr^{1/2}$ at 700°C. The pressure exponent observed for the permeability relationship, ~ 0.8, indicated that surface interactions were affecting the hydrogen migration mechanism. The generally high hydrogen solubility and permeability exhibited by titanium-alloys must be considered as an important area of concern in any assessments of the applicability of titanium-base materials to fusion reactor first-wall/blanket systems.

8.1.4 Progress and Status

Studies of the hydrogen permeation characteristics of titanium-base alloys have continued through the second quarter of FY-1979. As an added feature of this effort we have initiated studies of the solubility of hydrogen in Ti-6A1-4V.

Extensive investigations were conducted on the hydrogen permeability of a nitride-coated Ti-6A1-4V specimen[1,2] and the results were compared with previously obtained data[2] for uncoated Ti-6A1-4V. Over 50 measurements were made in the temperature range from 350 to 780°C using hydrogen driving pressures from 0.4 to 56 Pa. The time span over which these measurements were made was ∿2300 hours.

The data for the nitride-coated Ti-6A1-4V alloy, normalized to a half-power pressure dependence, are represented by the designated hatched-in area in Fig. 8.1.1. A similarly derived hatched-in representation is given in Fig. 8.1.1 for the "as-received" Ti-6A1-4V alloy based on data reported in reference 2. Also included in Fig. 8.1.1 is the permeation curve for 316-stainless steel (SS) for comparison purposes. The results in Fig. 8.1.1 indicate that the permeability of the nitride-coated alloy is (1) at best an order of magnitude lower than that of the uncoated alloy and (2) still too high to be acceptable in most fusion reactor first wall, blanket or heat-transfer system applications.[3]

The increased scatter in the permeation results for the class of titanium-alloys currently under study, compared to previous results for austenitic and nickel-base alloys,[4,5] is believed to be due in part to the sensitivity of the titanium-bearing materials to surface impurity effects and metallurgical phase transformations. However, we have also observed that the pressure dependence factor (pressure exponent) for the titanium alloys studied to date usually comes out to be in the range from 0.7 to 0.8 instead of the expected value[3] of 0.5 for bulk-diffusion-limited flow. As is shown in Fig. 8.1.2, the range of the scatter for the nitride-coated Ti-6A1-4V data is reduced considerably if an optimized pressure exponent is used. In fact, in any subsequent utilization of the results presented herein for the nitride-coated sample, it would be advisable to apply the data represented by the $P^{0.8}$ curve in Fig. 8.1.2.

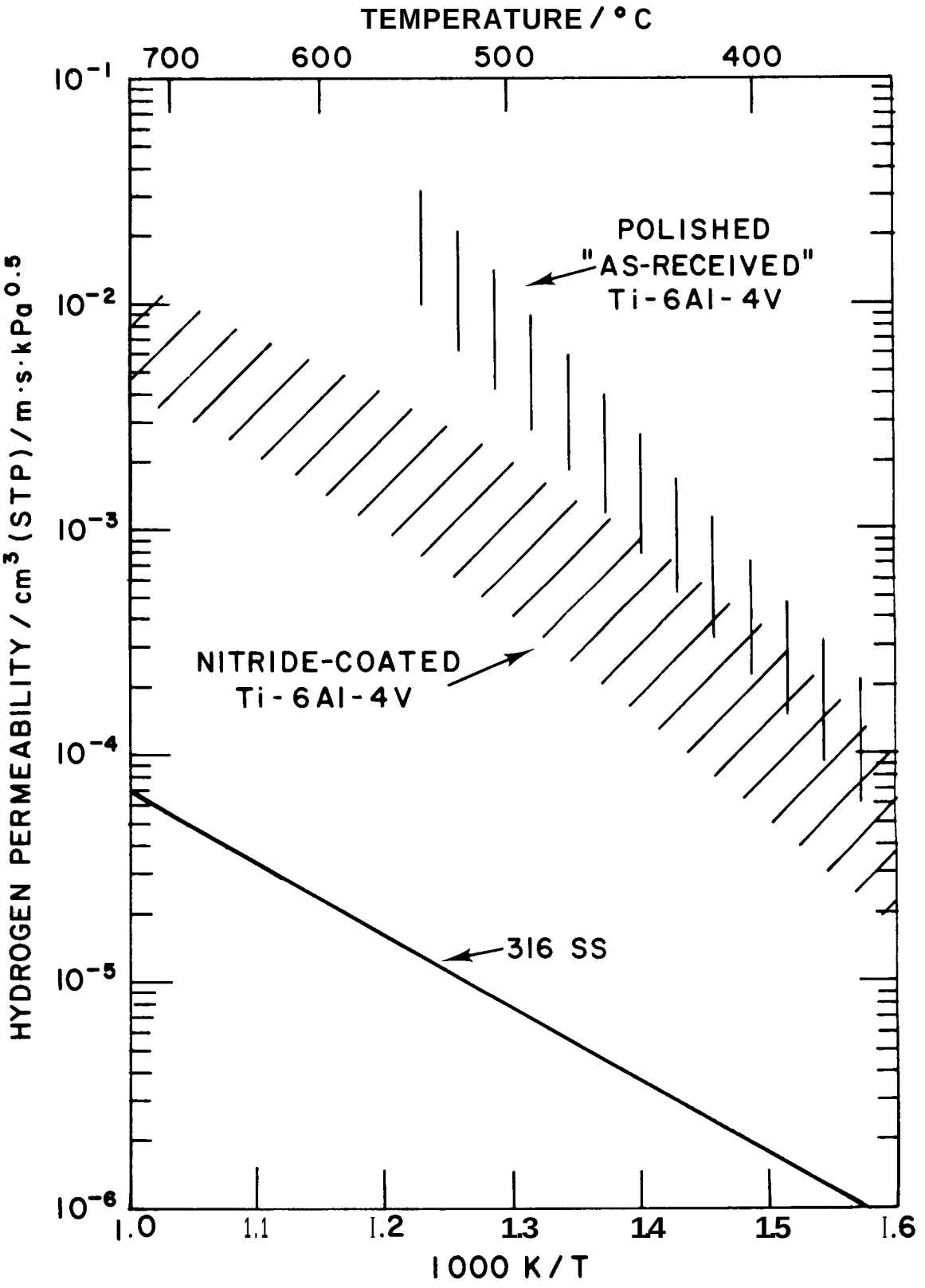

Fig. 8.1.1 Hydrogen permeability versus temperature for "as-received" and nitride-coated Ti-6Al-4V.

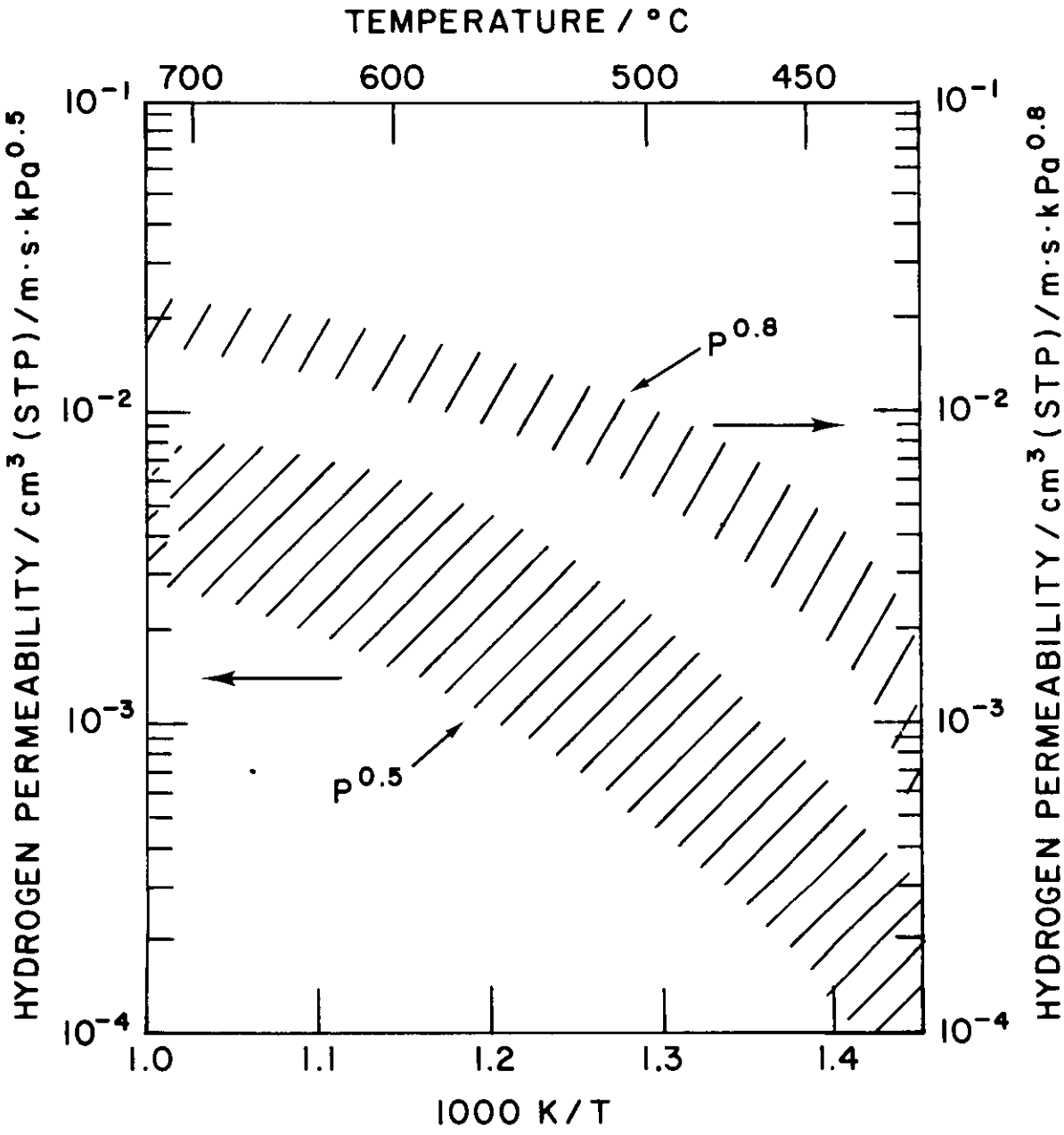

Fig. 8.1.2 Hydrogen permeability versus temperature and pressure (P) dependence factor for nitride-coated Ti-6Al-4V alloy.

The apparent curvature in the hatched areas in Fig. 8.1.2 is believed to be a real effect and is most probably due to the fact that the solubility of hydrogen in titanium is decreasing at a greater exponential rate with temperature than the corresponding diffusion coefficient is increasing. Although a complete understanding of the permeation mechanism for these titanium alloys is not yet at hand, it is clear that it is more involved than the classical Fick's Law formulation normally employed for non-hydride forming metals.[3]

Visual examination of the ion-nitride coated sample after permeation testing gave evidence that some of the nitride surface coating has either partially diffused into the bulk alloy or been chemically transported to another region of the permeation apparatus (presumably by hydrogen). Metallurgical and chemical analyses of this sample are in progress.

The sample presently under study in the permeation apparatus is a specimen of Ti-6A1-4V that has an anodized coating on both surfaces (upstream and downstream). Preliminary data for this sample indicate that the hydrogen permeability may be reduced by a factor of 50 to 100 compared to uncoated Ti-6Al-4V.

Because of the present uncertainties with regard to the exact nature of the permeation mechanism in titanium-alloys, it has not been possible to obtain reliable values for the solubility of hydrogen in these alloys by unfolding the initial transient portions of the time versus flow rate curves. Accordingly, an equilibrium solubility experiment has been conducted using tensimetric procedures and employing an existing Sieverts' Law apparatus. Results for the Ti-6Al-4V alloy are shown in Fig. 8.1.3 as isothermal plots of $P^{0.5}$ versus the amount of hydrogen dissolved in the alloy. Sieverts' constants, K_S, obtained from the linear sections of the isotherms in Fig. 8.1.3 are plotted in Fig. 8.1.4 together with some earlier data for the same alloy reported by Waisman et al.[6] The two sets of data taken collectively are considered to represent a reliable expression of the Sieverts constant as a function of temperature for Ti-6Al-4V. Observe that at 500°C and a pressure of 10^{-2} torr (1.3 Pa), the weight fraction of hydrogen in the alloy would be

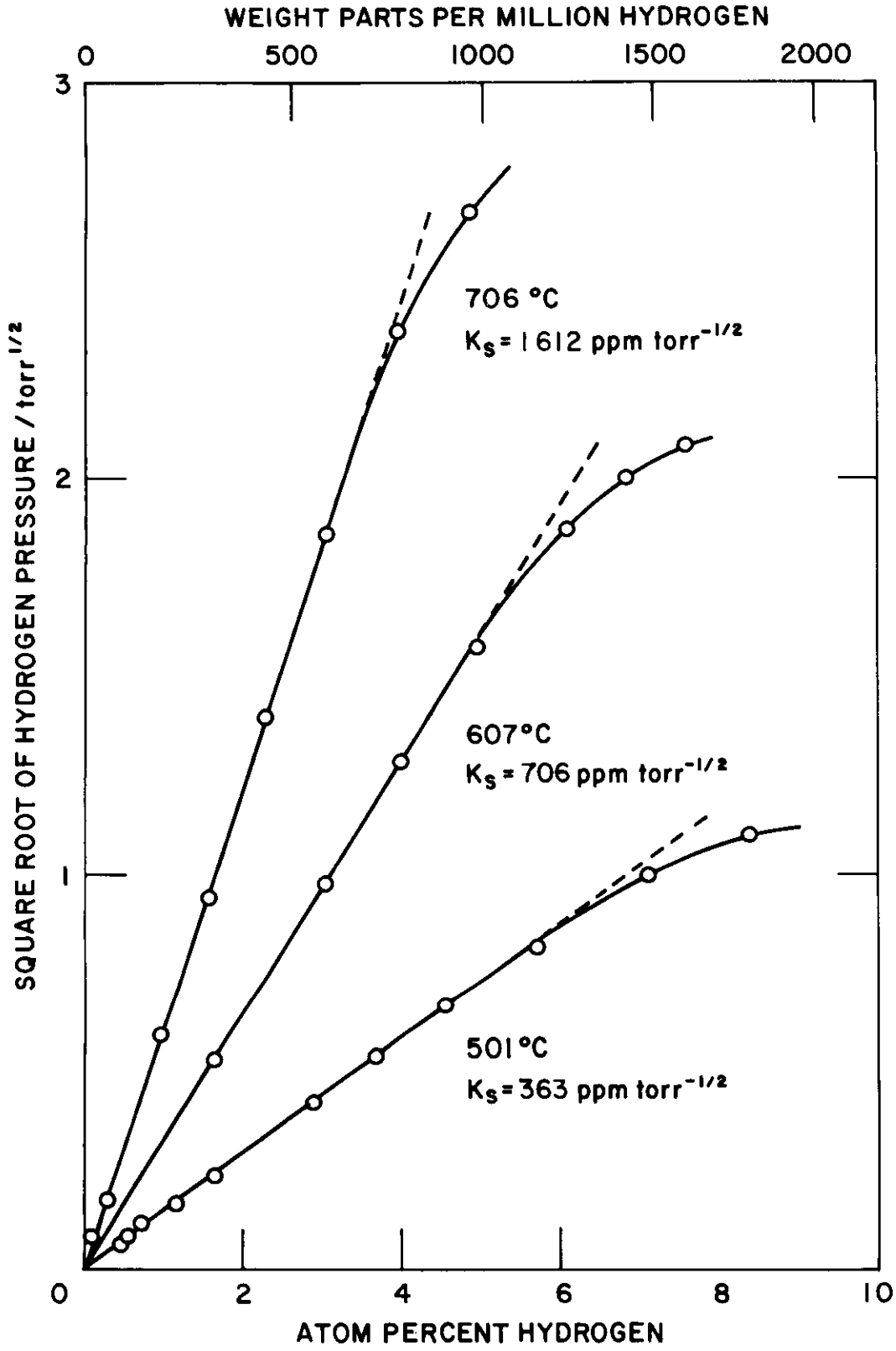

Fig. 8.1.3 Sieverts' Law constants for hydrogen in the α-phase of Ti-6Al-4V alloy.

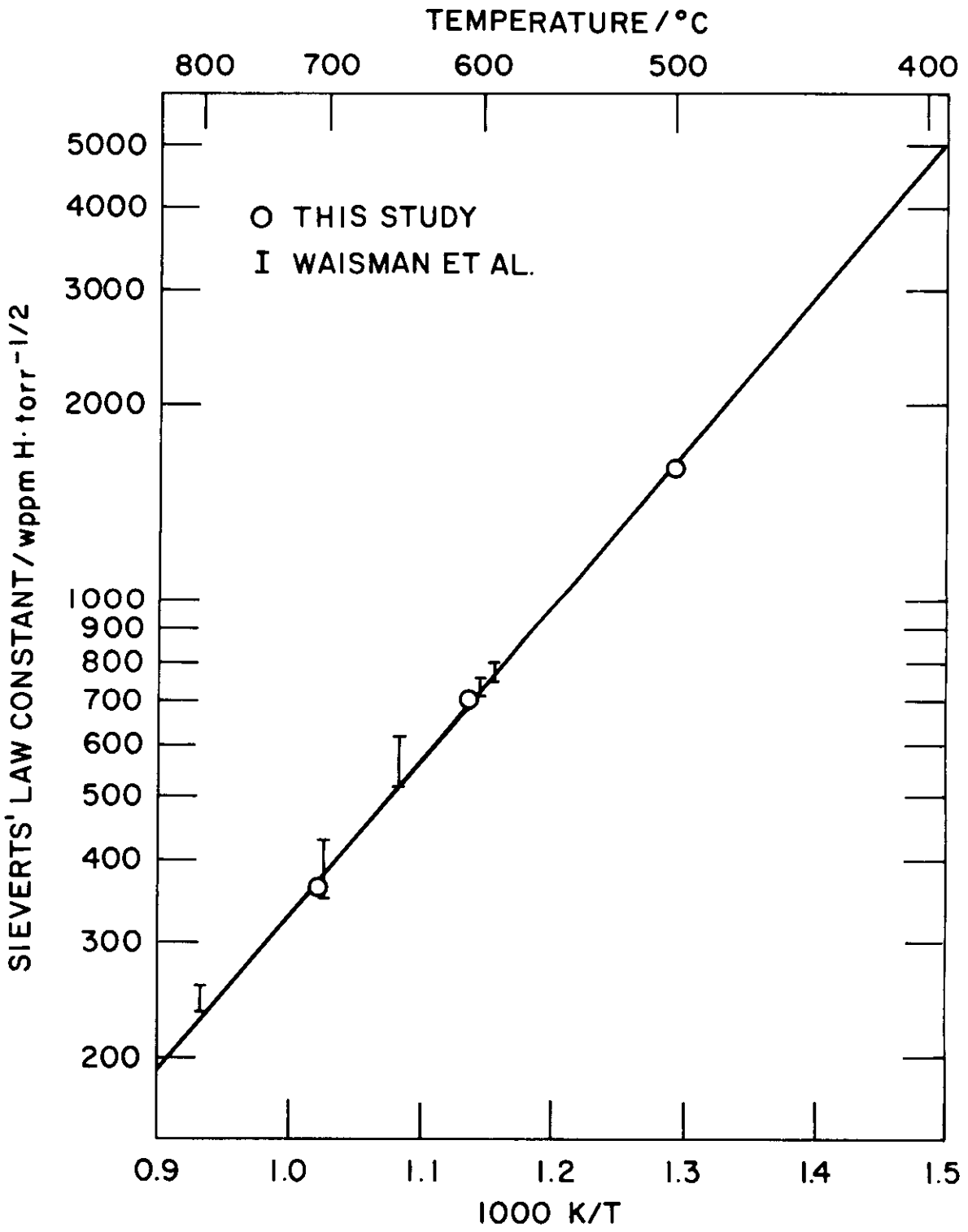

Fig. 8.1.4 Temperature dependence of Sieverts' Law constant for hydrogen in the α-phase of the Ti-6Al-4V alloy.

> 150 wppm and the corresponding atomic fraction would be >7500 wppm. A data set is presently being collected at a temperature near 400°C to extend the results in Fig. 8.1.4. The data values in the 400 to 550°C region are particularly important because this is the temperature region wherein it is expected that alloys such as Ti-6Al-4V will be operating in fusion reactor applications.

8.1.4 Conclusions

The reduction in hydrogen permeability attributable to the ion-nitride coating applied to the upstream surface of a Ti-6Al-4V sample was at best a factor of 10-X compared to the uncoated material. The pressure exponent of the permeation equation for this coated alloy, ∿0.8, indicates that surface-related interactions were affecting the hydrogen migration process. Recent measurements of the solubility of hydrogen in Ti-6Al-4V between 500 and 700°C are consistent with earlier data collected between 600 and 800°C. Because of the generally high solubility and permeability of hydrogen isotopes observed with these alloys, tritium inventories, migration rates, and hydrogen embrittlement must be considered as major concerns in addressing the applicability of titanium-base materials to fusion first wall/blanket systems.

8.1.5 References

1. E. H. Van Deventer and V. A. Maroni, *Hydrogen Permeation Characteristics of Path A, Path B, and Path C Alloys*, Alloy Development for Irradiation Performance Quarterly Progress Report: July-September 1978, U.S. Department of Energy Report DOE/ET-0058/3 (1978) pp. 101-107.
2. E. H. Van Deventer and V. A. Maroni, *Hydrogen Permeation Characteristics of Titanium-Base Alloys*, Alloy Development for Irradiation Performance Quarterly Progress Report: October-December 1978, U.S. Department of Energy Report DOE/ET-0058/4 (1979) pp. 128-132.
3. V. A. Maroni and E. H. Van Deventer, "Materials Considerations in Tritium Handling Systems," Proceedings of the First Topical Meeting on Fusion Reactor Materials, to appear in *J. Nucl. Mater.*.

4. E. H. Van Deventer and V. A. Maroni, *Hydrogen Permeation of Type-316 Stainless Steel,* Alloy Development for Irradiation Performance Quarterly Progress Report: January-March 1978, U.S. Department of Energy Report DOE/ET-0058/1 (1978) pp. 215-224.

5. E. H. Van Deventer and V. A. Maroni, *Hydrogen Permeation Characteristics of Path A, Path B, and Path C* AZZoys, Alloy Development for Irradiation Performance Quarterly Progress Report: April-June 1978, U.S. Department of Energy Report DOE/ET-0058/2 (1978) pp. 169-174.

6. J. L. Waisman, G. Sines and L. B. Robinson, "Diffusion of Hydrogen in Titanium Alloys Due *to* Composition, Temperature, and Stress Gradients," *Metall. Trans.* 4 (1973) pp. 291-302.

8.2 THE CORROSION OF Ni-Fe-Cr AND Co-V-Fe (LRO) ALLOYS IN STATIC LITHIUM — P. F. Tortorelli and J. H. DeVan (ORNL)

8.2.1 ADIP Task

ADIP Task I.A.3, Perform Chemical and Metallurgical Compatibility Analyses.

8.2.2 Objective

The purpose of this program is to determine the chemical compatibility of possible fusion reactor materials with metallic lithium. Specimens are exposed to static lithium containing selected solute additions to identify the kinetics and mechanisms that govern corrosion by lithium. Specific program objectives are (1) to determine the effects of N, C, H, and O on apparent solubilities in lithium; (2) to determine the C and N partitioning coefficients between alloys and lithium; (3) to determine the effects of soluble (Ca, Al) and solid (Y, Zr, Ti) active metal additions on corrosion by lithium; and (4) to determine the tendencies for dissimilar-metal mass transfer.

8.2.3 Summary

The compatibility of alloy 600 and a 60% Co–25% V–15% Fe ordered alloy with static lithium was investigated. Alloy 600 corroded significantly in pure lithium between 500 and 700°C. However, it lost no weight when exposed to Li–5 wt % Al under otherwise similar conditions. Alloy 600 welds were not significantly attacked by the lithium. A long-range-ordered (LRO) alloy was exposed to lithium at 600 and 850°C for 2000 h and then tensile tested. The samples exposed at 850°C showed no loss of ductility at room temperature and just a small amount of intergranular cracking; however, specimens exposed at 600°C exhibited loss of ductility and an extensive number of grain boundary cracks. No chemical dissolution of the LRO alloy due to lithium exposure was observed.

8.2.4 Progress and Status

In order to obtain preliminary data on the compatibility of molten lithium and representative Path B alloys, alloy 600 was tested in static lithium. It has about the same nickel content as the 75%-Ni base research alloy (B-6). Alloy 600 coupons were sealed with pure lithium or Li—5 wt % Al in alloy 600 tubing, and these assemblies were enclosed in type 316 stainless steel capsules. Tests were performed for 1000 h at 500, 600, and 700°C. The resulting weight losses are given in Table *8.2.1* together with comparable data for type 316 stainless steel. Despite the scatter in the data, two points are evident: (1) the corrosion of alloy 600 is much more severe than that of austenitic stainless steel, and (2) the addition of aluminum to the lithium appears to be an effective means of inhibiting the corrosion.

Table 8.2.1. Weight Changes of Alloy 600 and Type 316 Stainless Steel Exposed to Lithium and Li—5 wt % Al[a]

Bath	Temperature (°C)	Weight Change, g/m2	
		Alloy 600	316 SS
Li	500	0.0, −47.3	+0.3
Li	600	−2.3, −5.7	−0.1
Li	700	−176.6, −227.6	−0.3
Li—5 wt % Al	500	+9.0, +9.3	+1.1
Li—5 wt % Al	600	+2.9, +17.1	+6.5
Li—5 wt % Al	700	+10.9, +33.1	+19.3

[a]Exposure time of 1000 h for all tests except the 316 SS/Li—5 wt % Al series, which had 2000 h exposures.

The enhanced corrosion of alloy 600 relative to that of stainless steel is not unexpected since nickel is much more soluble in lithium than iron or chromium.[1] This trend has already been observed[2] in that type 310 stainless steel (20%Ni) corroded more in static lithium at 700°C than did other austenitic stainless steels with 8 to 12%Ni. The results of these alloy 600 experiments, however, are confused by the

inconsistency of the observed corrosion. In addition to the scatter in the weight change data, metallographic examinations revealed non-uniform corrosion across the surfaces of individual specimens. Figure 8.2.1 shows how the extent of the corrosion varied on one particular specimen. More experiments are required to clearly define the corrosion processes. The welds (82T filler wire) that were used to join the alloy 600 tubing to the alloy 600 end caps were also metallographically examined after test and appeared to be more compatible with the static lithium than the wrought alloy.

In the same test series we also determined the effect of aluminum additions to lithium on the corrosion of alloy 600. Previous work[2] had shown that weight losses between 500 and 700°C were significantly reduced for type 316 stainless steel when aluminum was added to static lithium. Additionally, the corrosion of type 316 stainless steel in flowing lithium was reduced by a factor of 5 at 600°C when the lithium contained 5 wt % Al.[3] Because of the effectiveness of 5 wt % Al additions in previous tests, that same aluminum concentration was used in the present test series. With the aluminum added, the weight losses of alloy 600 were negligible in static lithium at 500, 600, and 700°C. As with the type 316 stainless steel tests in lithium plus aluminum,[2] the aluminum reacted with the alloy 600 to form corrosion-resistant intermetallic surface layers. An example of this layer is shown in Fig. 8.2.2.

A series of long-range-ordered (Co-V-Fe, Co-V-Fe-Ni) alloys **has** been developed at ORNL and may offer a significant advantage over conventional or disordered alloys for first-wall applications.[4] Consequently, they are primary candidates for Path D of the ADIP program. In order to gain a preliminary assessment of the compatibility of these alloys with molten lithium, samples of the LRO-1 alloy (60 wt % Co-25 wt % V-15 wt % Fe) were exposed to pure static lithium. Tensile specimens were placed in LRO-1 alloy cylinders (open at the top) containing lithium and were subsequently sealed inside type 316 stainless steel capsules. In 2000 h at 600 and 850°C the average weight changes were -0.2 g/m^2 and +2.1 g/m^2, respectively. The 600°C test result is comparable to that for type 316 stainless steel, which lost about

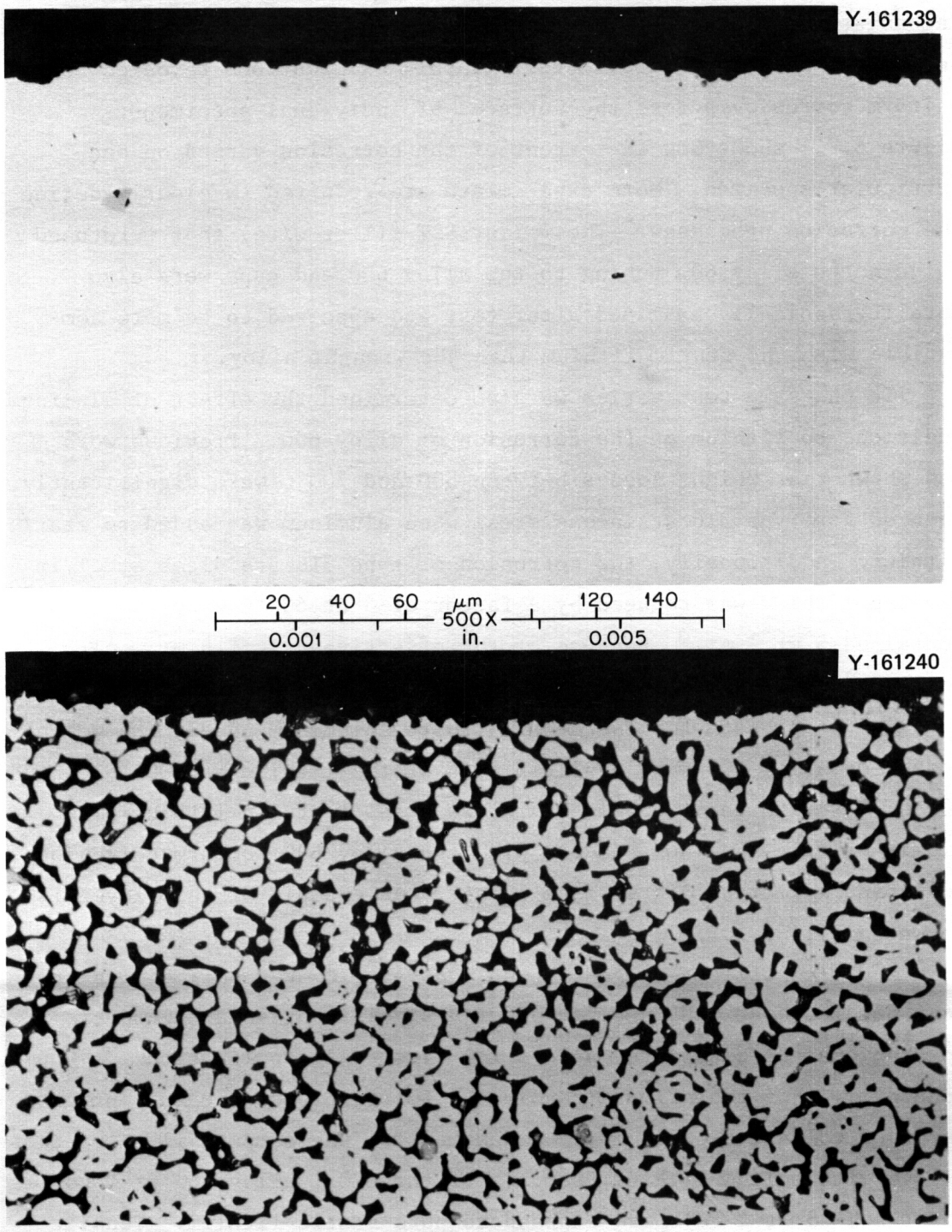

Fig. 8.2.1. Alloy 600 Exposed to As-Purified Lithium for 1000 h at 700°C; Two Areas on the Same Surface.

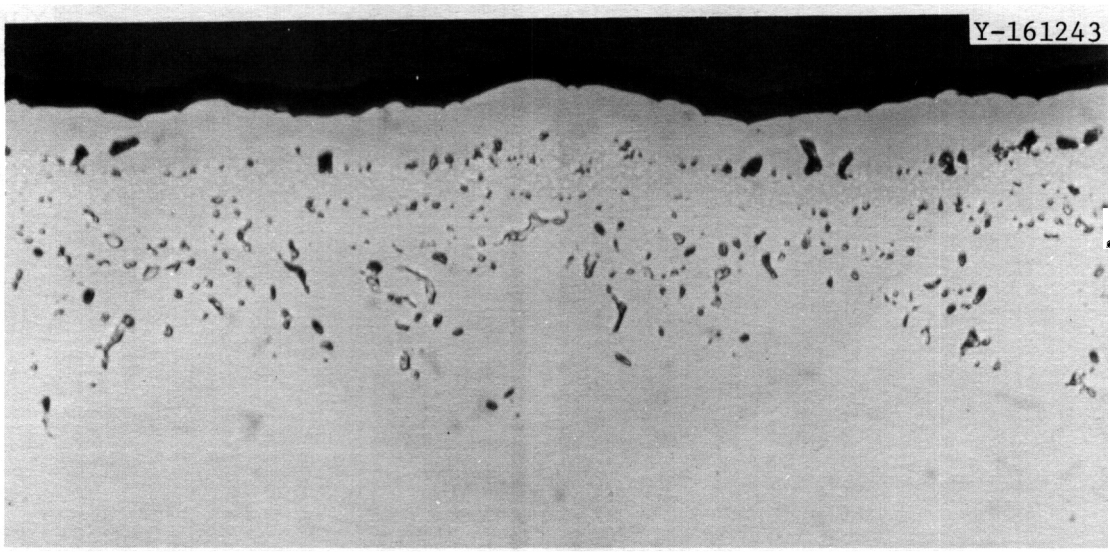

Fig. 8.2.2. Alloy 600 Exposed to Li—5 wt % Al for 1000 h at 700°C. 500×.

0.1 g/m^2 in 2000 h at 600°C. After lithium exposure, the ordered alloy was tensile tested at room temperature. Compared with tensile results for an unexposed specimen, lithium exposure at 600°C caused a decrease in ductility at room temperature. However, the ductility was unaffected by exposure at 850°C. The reduced ductility after 600°C exposure is not well understood at the present time, but may be related to contamination by interstitials that come from the lithium or the stainless steel capsule.

After mechanical testing, two of the LRO-1 alloy tensile specimens were metallographically examined. The results are summarized by the micrographs in Fig. 8.2.3. For the specimen that was held in a lithium bath at 600°C for 2000 h, tensile straining produced many intergranular cracks along the exterior surface, including the grip area, where the amount of deformation was small. In contrast, tensile deformation of the sample exposed to lithium for 2000 h at 850°C resulted in fewer intergranular cracks over the gage length and no significant cracking in the grip area. The specimens are now being chemically analyzed to determine whether the deformation behavior can be correlated with changes in contents of carbon, nitrogen, or oxygen.

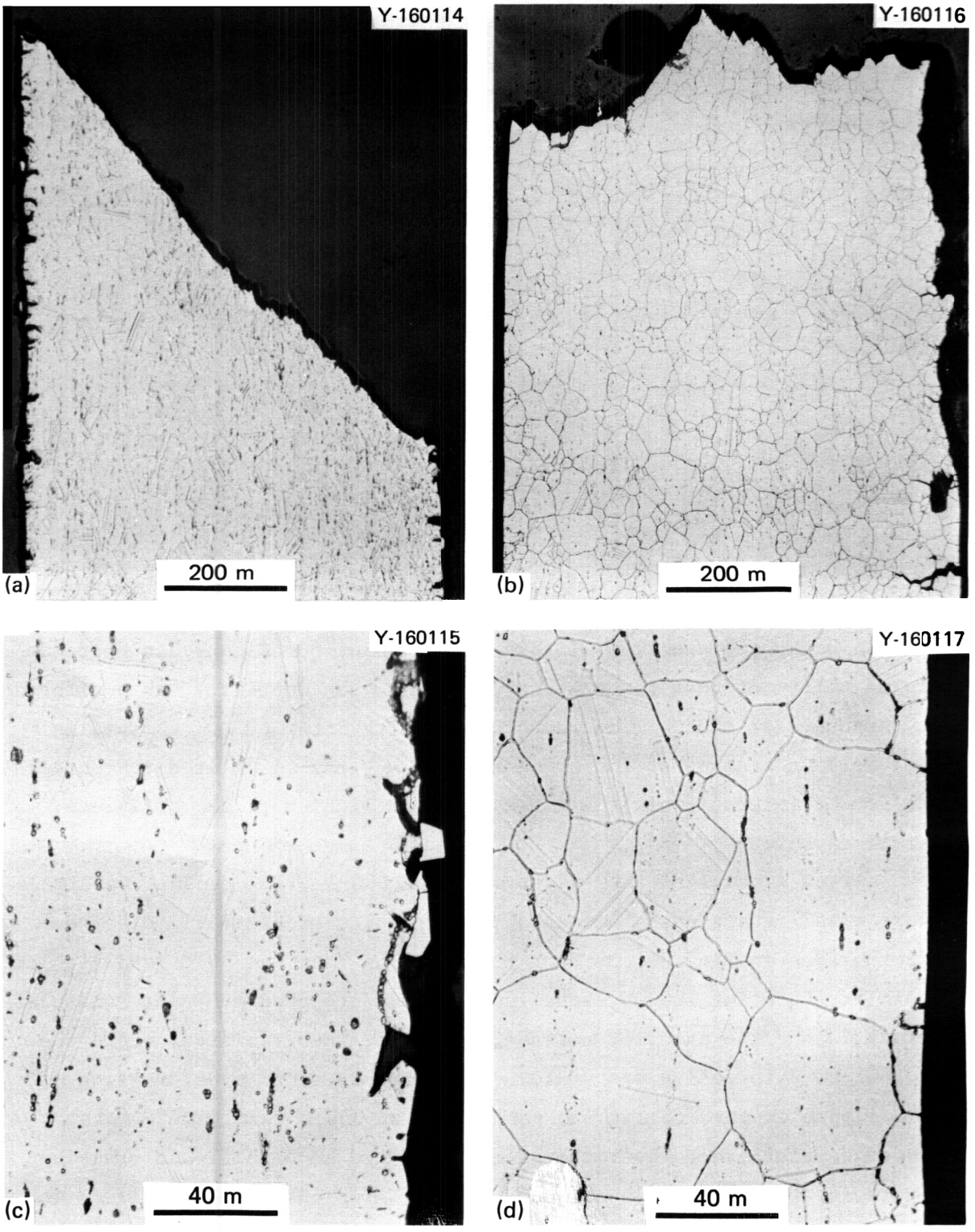

Fig. *8.2.3.* Long-Range-Ordered Alloy LKO-1 *(Co-25%* V-15% Fe) Exposed to Lithium for *2000* h and Then Tensile Tested at Room Temperature. (a,b) Fracture area. (c,d) Grip area. (a,c) *600°C* exposure. (b,d) 850°C exposure.

8.2.5 Conclusions

1. The corrosion of alloy 600 in static lithium was more severe than that of stainless steel. The addition of 5 wt % Al to the lithium effectively inhibited the corrosion.

2. Long-range-ordered alloy LRO-1 (60% Co-25% Fe-15% V) was as corrosion resistant in static lithium as stainless steel. After a 850°C exposure in lithium, it retained its original room temperature ductility, but a decrease in ductility was observed after exposure at 600°C.

8.2.6 References

1. H. W. Leavenworth and R. E. Cleary, "The Solubility of Ni, Cr, Fe, Ti, and Mo in Liquid Lithium," *Acta Metall.* 9: 519-20 (1961).

2. P. F. Tortorelli and J. H. DeVan, "Capsule Tests of Iron-Base Alloys in Lithium," *ADIP Quart. Prog. Rep. June 30, 1978,* DOE/ET-0058/2, pp. 148-57.

3. J. H. DeVan and J. R. DiStefano, "Capsule Tests of Iron-Base Alloys in Lithium," *ADP Quart. Prog. Rep. Mar. 31, 1978,* DOE/ET-0058/1, pp. 190-99.

4. C. T. Liu, "Development of Ductile Long-Range Ordered Alloys for Fusion Reactor Systems," paper presented at First Topical Meeting on Fusion Reactor Materials, January 1979; to be published in the *Journal* of *Nuclear Materials.*

8.3 CORROSION IN LITHIUM–TYPE 316 STAINLESS STEEL THERMAL–CONVECTION SYSTEMS – P. F. Tortorelli and J. H. DeVan (ORNL)

8.3.1 ADIP Task

ADIP Task I.A.3, Perform Chemical and Metallurgical Compatibility Analyses.

8.3.2 Objective

The purpose of this task is to determine the corrosion resistance of possible first–wall materials to flowing lithium in the presence of a temperature gradient. Corrosion rates (in terms of both dissolution and deposition) are measured as functions of time, temperature, additions to the lithium, and flow conditions. These measurements are combined with chemical and metaliographic examinations of specimen surfaces to establish the mechanisms and rate–controlling processes for dissolution and deposition reactions.

8.3.3 Summary

X–ray fluorescence of the coupons from a type 316 stainless steel thermal–convection loop that circulated lithium with 500 wt ppm N indicated that the addition of nitrogen to the lithium affected the distribution of nickel around the circuit. Metallographic examination revealed that the added nitrogen did not change the basic dissolution mechanism and did not promote intergranular attack. Two type 316 stainless steel loops that had circulated as–purified lithium for long periods of time developed plugs. One of these plugs was examined and appeared to be composed of a tangle of small chromium crystals.

8.3.4 Progress and Status

As described previously,[1] two types of thermal–convection loops (TCLs) are being used to determine the compatibility of austenitic stainless steels with lithium. The first type is in the form of a 0.46–m by 0.64–m parallelogram that contains interlocking tab specimens of the same material as the loop. The loop is operated without interruption for 3000 to 10,000 h and is then cut open to remove tab specimens

for analysis. The second type of TCL is larger (0.48 m by 0.76 m) and is designed so that tab specimens can be withdrawn and inserted without altering the loop operating conditions. In this way, corrosion rates can be monitored at selected time intervals for a given set of test specimens.

The preceding quarterly[2] reported weight losses for a type 316 stainless steel thermal-convection loop that operated for 3000 h with a maximum temperature of 590°C and a temperature difference of 170°C. The lithium in the loop had been purposely contaminated with Li_3N to about 500 wt ppm N. From the weight losses of this loop and similar data for earlier loop experiments using pure and nitrogen-contaminated lithium, we concluded that the presence of added nitrogen (500—1700 ppm) in lithium had no significant effect on the amount of dissolution in type 316 stainless steel systems.[2] Since then, both chemical and metallographic examinations of this loop's coupons have been completed. X-ray fluorescence of the individual samples revealed the same type of behavior as found for earlier loops with purer lithium: preferential losses of nickel and chromium from the hotter region of the loop and subsequent deposition in the colder areas. This phenomenon is illustrated in Fig. 8.3.1, which shows coupon surface composition, as determined by x-ray fluroescence, versus position in the TCL. While it is similar, in general, to data obtained from other stainless steel loops (see, for example, ref. 3), the plot in Fig. 8.3.1 differs in one important respect: the position of the cold leg nickel balance point, which is defined as the location at which the nickel concentration of the coupon is approximately its original weight fraction in the steel. This point is noted in Fig. 8.3.1. The difference between the nickel balance point in this loop and other lithium TCLs that contained differing nitrogen concentrations is shown in Table 8.3.1. Note that for the loops with added nitrogen, the nickel balance point is further downstream than in type 316 stainless steel loops containing purer lithium. In contrast, the chromium balance points for the four TCLs listed in Table 8.3.1 are all less than 0.48 m downstream from the point of maximum temperature. Their positions cannot be measured exactly because they fall in horizontal sections of the loops, which cannot

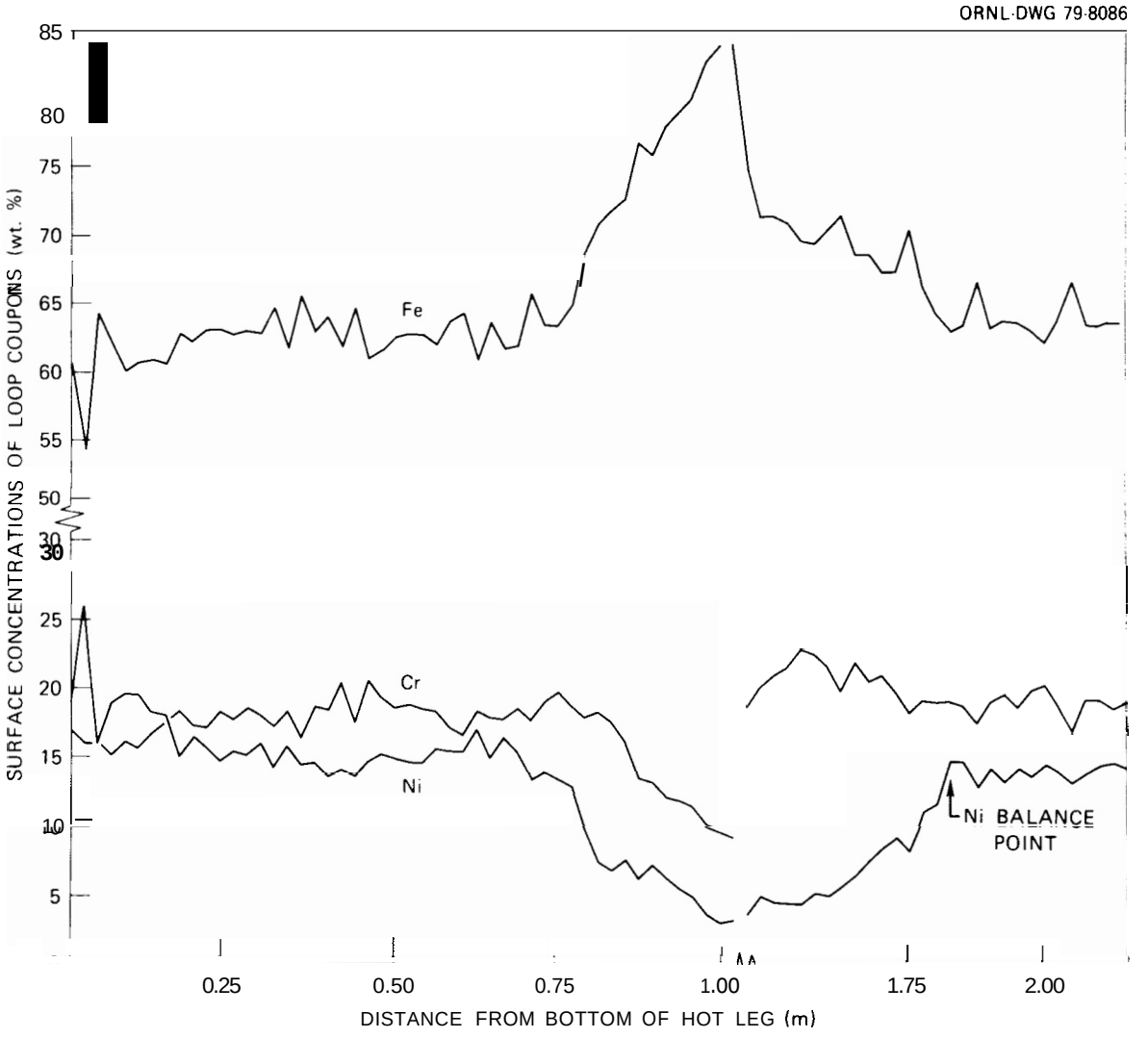

Fig. 8.3.1. Coupon Surface Composition Versus Loop Position as Determined by X-Ray Fluorescence.

Table 8.3.1. Comparison of Nickel Balance Points in Thermal-Convection Loops of Lithium in Type 316 Stainless Steel

Loop	Exposure (h)	N Content (wt ppm)	T_{max} (°C)	ΔT (°C)	Flow Velocity (mm/s)	Ni Balance Point Location[a] (m)
1	3,000	0	600	200	22	0.58
2	10,000	0	600	200	15	0.58
3	3,000	500	590	170	7	0.78
4	3,000	1700	600	200	16	0.70

[a]Measured downstream from the point of maximum temperature.

be monitored by coupons. Nevertheless, one can conclude that the distribution of chromium is less affected by nitrogen added to the lithium than is the distribution of nickel.

The ratio of the complementary regions of weight gains and losses in a thermal-convection loop is critically dependent on the relative kinetics of the dissolution and deposition processes. For example, if dissolution is rapid compared with deposition, then, given the fact that at steady state what goes into the lithium must come out (that is, conservation of mass), deposition must occur over a larger region than dissolution. In view of this, the above observation that nitrogen in lithium tended to move the nickel balance point downstream — that is, tended to decrease the area over which nickel deposition took place — indicates that if the same mechanisms are operative, the nickel dissolution step was slowed and/or the nickel deposition reaction was accelerated. Since the difference in the weight changes at the maximum temperature between the loop with 500 wt ppm N (loop 3 as reported in Table 8.3.1) and loop 1, which circulated pure lithium, is not great,[2] we can assume that the nickel dissolution rate was unchanged and therefore the nickel deposition rate was faster in flowing lithium containing nitrogen.

Coupons from selected positions in the TCL test with 500 wt ppm added N (loop 3) were metallographically examined. Parts (a), (b), and

and (c) of Fig. 8.3.2 are micrographs of coupons from this loop that represent the maximum temperature, an intermediate temperature in the cold leg and the minimum temperature (bottom of cold leg), respectively. For comparison, a micrograph (d) of the coupon at the maximum temperature position in loop 1 (Table 8.3.1) is also included. Although the depth of attack at the hottest points is different in loops 1 and 3, the manifestations of attack are quite similar in the two loops. In particular, no grain boundary attack was observed in either loop. Coupon surfaces near the points in the loop where there was no apparent weight change showed a combination of a porous layer, indicative of material loss, and surface deposits [see Fig. 8.3.2(b)]. Further downstream, deposition was dominant, as seen in Fig. 8.3.2(c).

The accumulation of deposits in the colder regions of a lithium circuit tends to be even more serious a problem than the loss of structural material in higher temperature regions. Such deposits slow or stop flow by plugging. In this last quarter, two of our large thermal-convection loops had to be shut down because of this problem. Both were drained of their lithium, and their cold legs were cut out of the circuits and sliced lengthwise. Examination of the leg from the loop with over 10,000 h operation revealed a plug near what was the loop's coldest point (see Fig. 8.3.3). However, no plug was found in the second loop (over 6000 h of operation), but remnants of one were observed in the same location as the plug in the first loop. We thus believe that it dislodged during draining. The plug from the first loop appeared to be composed of lithium and small crystals that seemed to resemble the almost pure (95%) chromium deposits found[4] on cold leg coupons in a loop that operated for 1700 h. These deposits and the extracted plug are presently being studied in detail. Preliminary indications are that the initial mass transfer deposits are nearly pure chromium, but as the loop operation continues, the composition of the deposits changes. We hope that the results from this work will help in understanding the complex deposition processes that take place in nonisothermal systems of lithium and stainless steel.

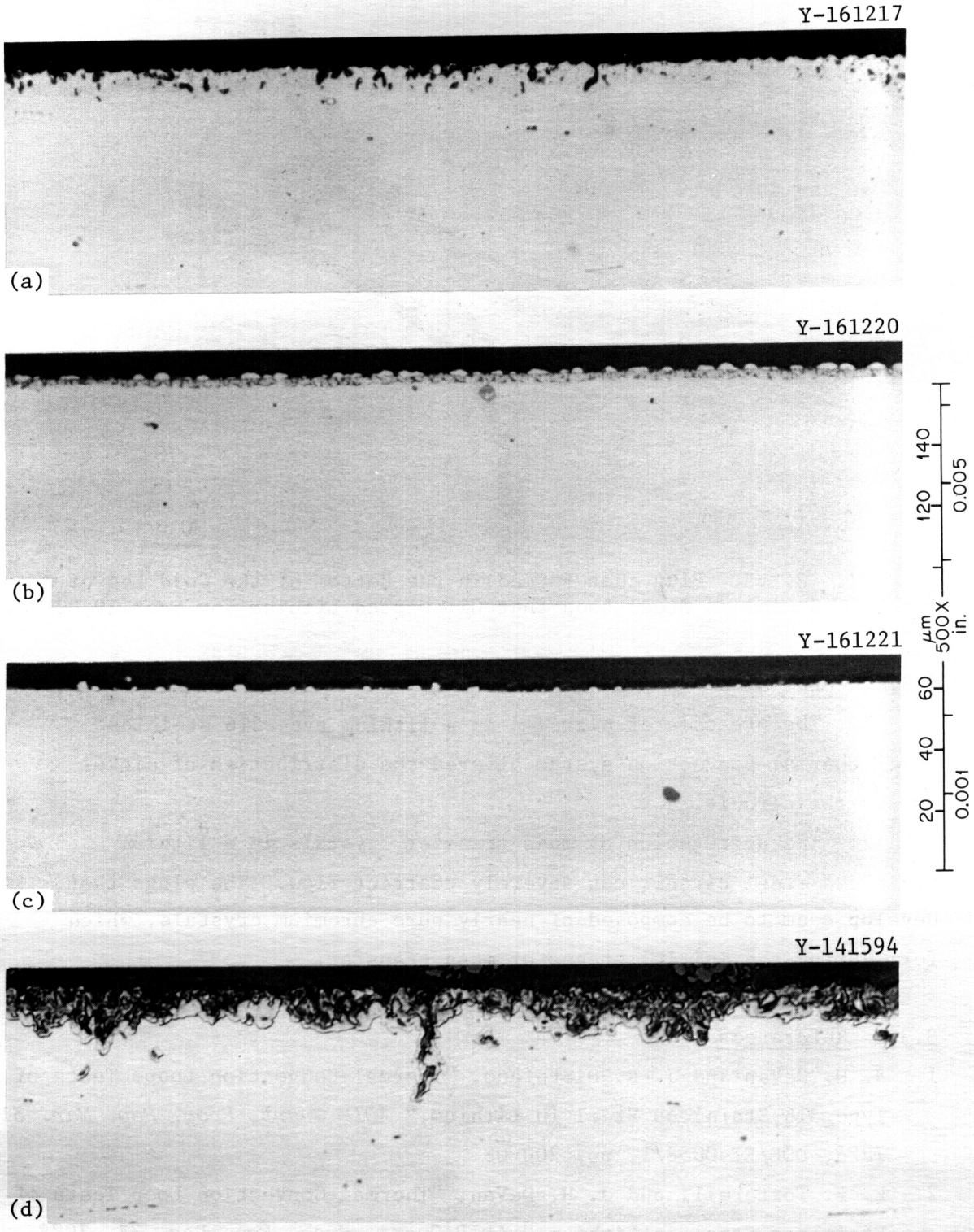

Fig. 8.3.2. Surfaces Exposed 3000 h to Flowing Lithium. (a) Li—500 wt ppm N, 590°C. (b) Li—500 wt ppm N, ∿460°C. (c) Li—500 wt ppm N, 420°C. (d) Pure Li, 600°C.

Y-159587

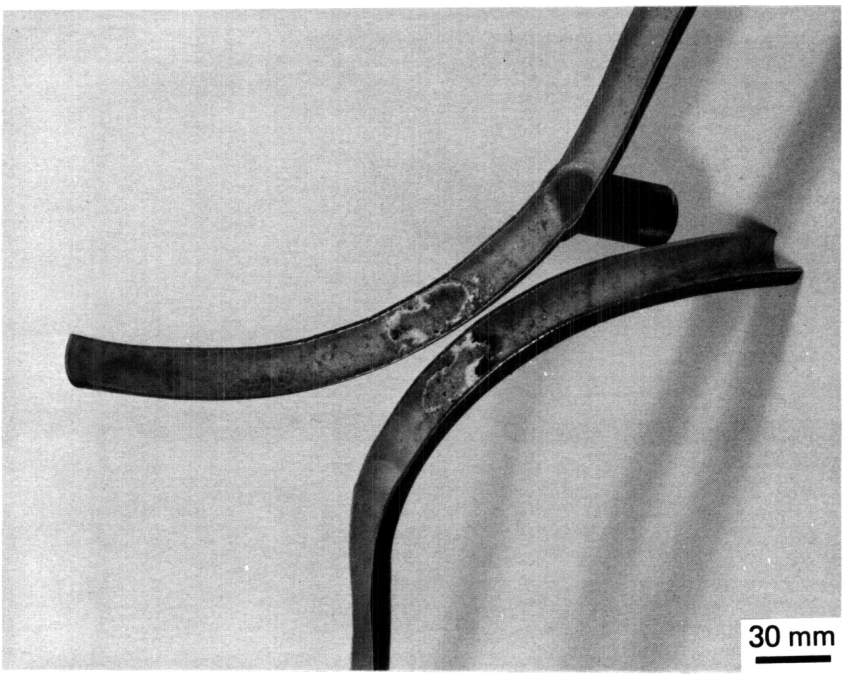

Fig. 8.3.3. Plug that Formed in the Bottom of the Cold Leg of a Type 316 Stainless Steel Loop that Circulated Lithium for over 10,000 h.

8.3.5 Conclusions

1. The presence of nitrogen in a lithium type 316 stainless steel thermal-convection system altered the distribution of nickel around the circuit.

2. The aggregation of mass transfer crystals in a lithium stainless steel circuit can severely restrict flow. The plugs that develop seem to be composed of nearly pure chromium crystals, which form during the initial stages of mass transfer.

8.3.6 References

1. J. H. DeVan and J. R. DiStefano, "Thermal-Convection Loops Tests of Type 316 Stainless Steel in Lithium," *ADP Quart. Prog. Rep. Mar. 31,* 1978, DOE/ET-0058/1, pp. 200-08.

2. P. F. Tortorelli and J. H. DeVan, "Thermal-Convection Loop Tests of Stainless Steel in Lithium," *ADIP Quart. Prog. Rep. Dec. 31, 1978,* DOE/ET-0058/4, pp. 120-27.

3. J. E. Selle, "Corrosion of Iron-Base Alloys by Lithium," pp. 453–61 in *Proc. Int. Conf. Liquid Metal Technology in Energy Production, May 3–6, 1976*, M. H. Cooper, ed., CONF-760503-P2.

4. P. F. Tortorelli and J. H. DeVan, "Thermal-Gradient Mass Transfer in Lithium-Stainless Steel Systems," paper presented at First Topical Meeting on Fusion Reactor Materials, January 1979; to be published in the *Journal* of *Nuclear Materials*.

8.4 VANADIUM ALLOY/LITHIUM PUMPED LOOP STUDIES – D. L. Smith and V. A. Maroni (Argonne National Laboratory).

8.4.1 ADIP Task

I.A.3. Chemical and Metallurgical Compatibility Analysis. The results presented in this section contribute to Subtask I.A.3.4, Milestones I.A.3.c, and I.A.3.d.

8.4.2 Objective

The objective of this work is to develop preliminary data on the compatibility of candidate Path C alloys exposed to a flowing lithium environment. The major effort will involve investigations of nonmetallic element interactions in reactive/refractory metal-lithium systems. Information relating to atmospheric contamination of reactive/refractory metal alloys will also be generated. Specific near-term experiments will include measurements on the distribution of nonmetallic elements between selected vanadium alloys and lithium, and the effects of lithium exposure on the mechanical properties of vanadium alloys. The results of this work will contribute to the data base for relating compatibility and corrosion phenomena to other alloy development activities and provide a basis for selecting candidate alloys for further development.

8.4.3 Summary

A stainless-steel-clad vanadium-15% chromium alloy loop for circulating liquid lithium has been constructed and placed in operation at the Argonne National Laboratory. This 0.5-liter-capacity, forced circulation loop will be used for investigations of the distribution of nonmetallic elements in lithium/refractory metal systems and effects of a lithium environment on the mechanical properties of selected refractory metals. Valuable information on weld integrity of vanadium-base alloys and problems associated with protection of refractory metals from atmospheric contamination is also being obtained. The results of this effort will contribute to the selection of candidate Path C alloys for extended development within the ADIP program.

8.4.4 Progress and Status

A small ($0.5 liter capacity) stainless steel-clad, vanadium-15% chromium loop for circulating liquid lithium has been constructed, filled with lithium, and placed in operation. The basic features and design details of the loop have been described elsewhere.[1,2] Figure 8.4.1 is a photograph of a typical joint assembly showing the vanadium-alloy weld and the stainless steel cladding. Figure 8.4.2 contains photographs of the fully assembled loop before and after applying heaters, instrumentation, insulation, etc. The horizontal legs of the loop are 45 cm long. The 0.125-cm-wall vanadium-alloy tubing was extruded in the ANL Materials Science Division. The short vertical leg and the horizontal legs are 1.25 cm OD whereas the extended vertical leg, which serves as the specimen test section, is 1.50 cm OD. The vanadium alloy tubing is clad with 0.125-cm-wall Type 304 stainless steel tube to form the duplex stock which serves to protect the vanadium alloy from atmospheric attack. The extended vertical leg is equipped with a retrieval tube and a ball and gate valve arrangement that provides a specimen loading and sample retrieval capability. The loop is equipped with an electromagnetic linear induction pump on the lower horizontal leg and a magnetic flowmeter on the upper horizontal leg.

The loop was filled with lithium from an attached reservoir and flow was initiated in early April. During checkout of instrumentation and procedures the loop has been operated at a temperature of *400 - 450°C* with lithium flow rates of 1.0 cm^3/s. Samples of lithium have been taken from the loop for analysis before increasing the temperature to the scheduled 600°C operating value. After the desired operating conditions are established a series of refractory metal test specimens will be loaded into the test section.

8.4.5 Conclusions

No experimental results have been obtained to date on this program.

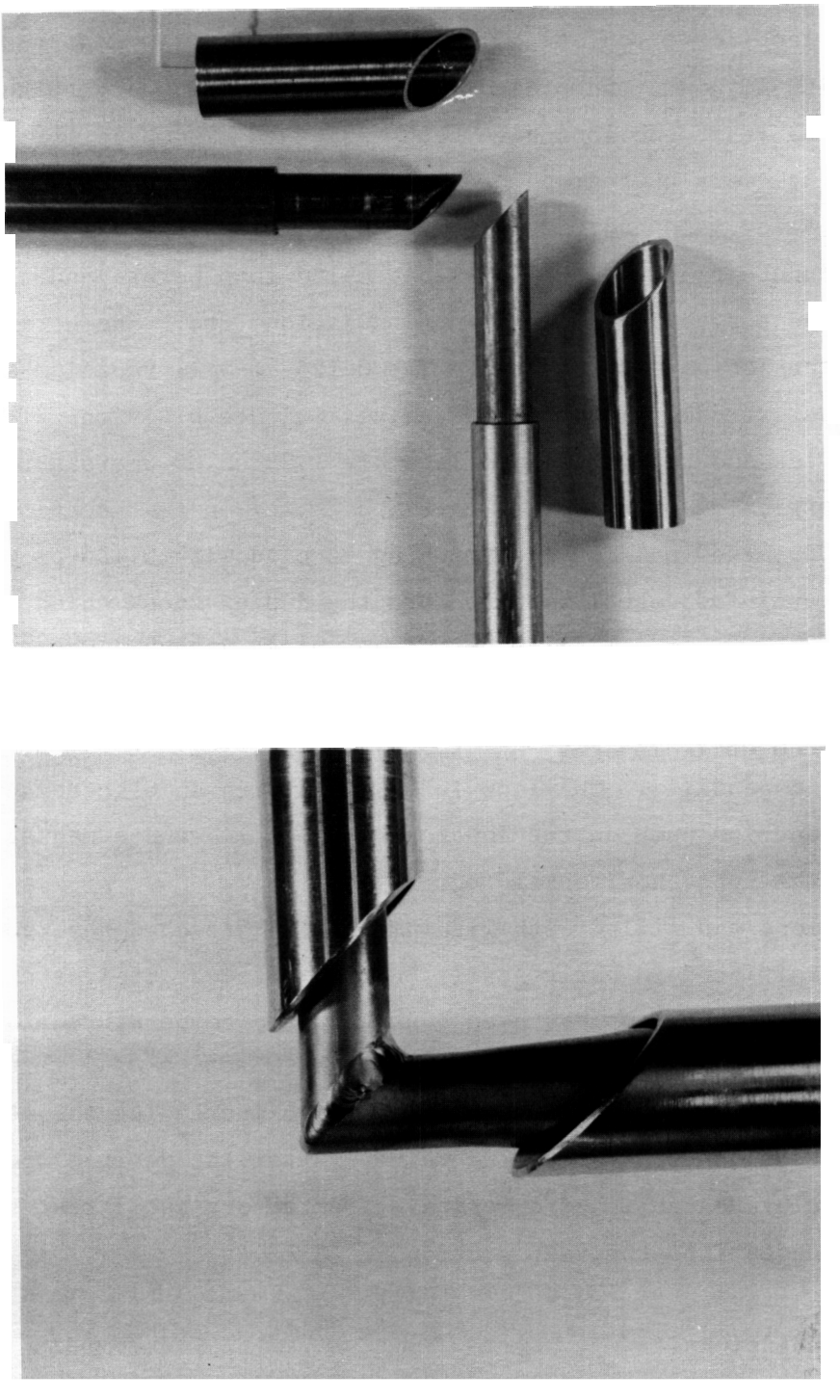

Fig. 8.4.1 Photographs of the preassembly and welded configuration for a typical joint in the SS-clad V-15Cr lithium loop.

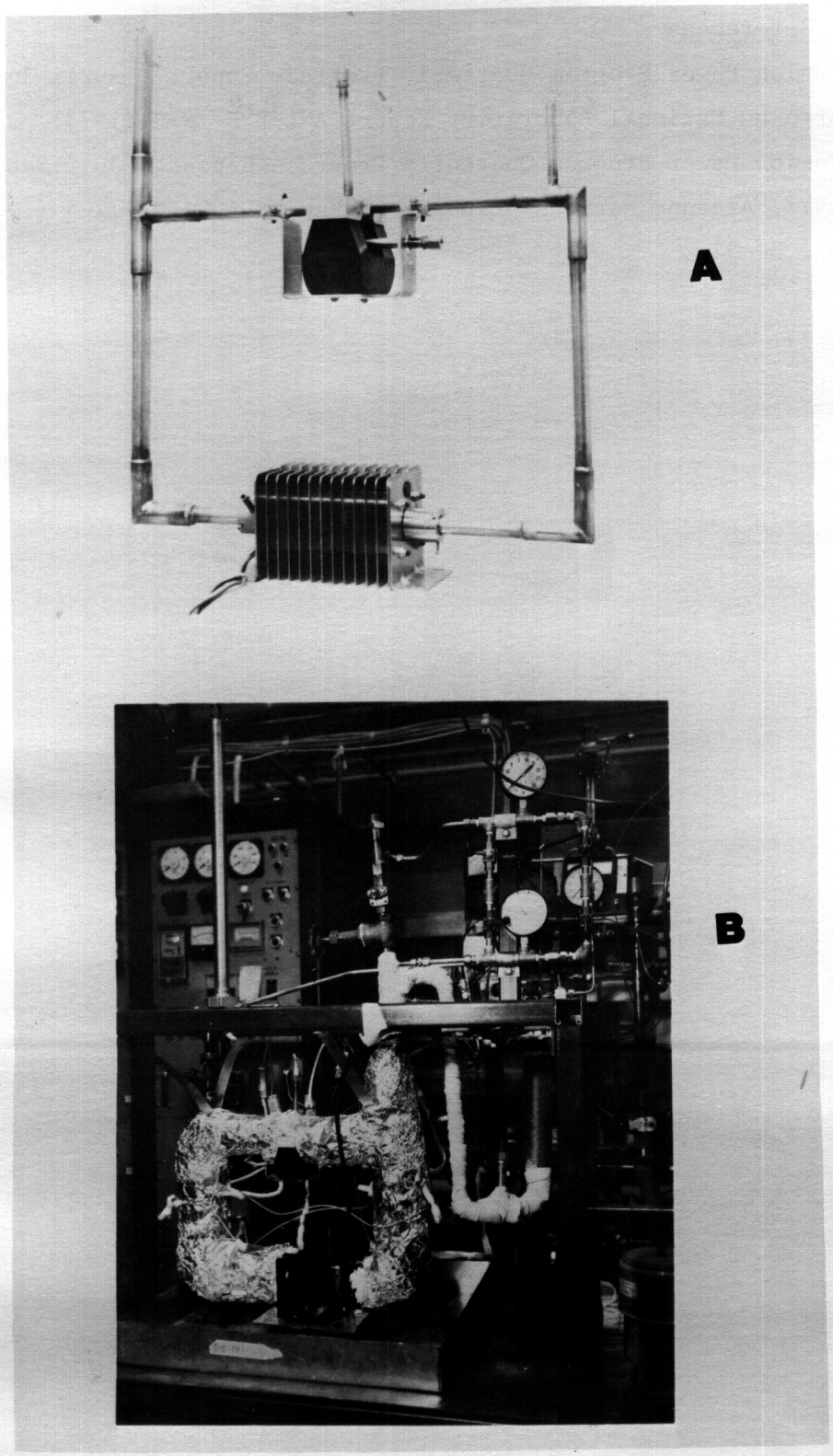

Fig. 8.4.2 Photographs of the SS-clad V-15Cr lithium loop before (A) and after (B) application of insulation and instrumentation.

8.4.6 References

1. Fusion Power Program Quarterly Progress Report: April-June 1978, Argonne National Laboratory Report ANL/FPP-78-2 (1978) p. 28.
2. Fusion Power Program Quarterly Progress Report: July-September 1977, Argonne National Laboratory Report ANL/FPP-77-4 (1977) pp. 30-32.

DOE/ET-0058/5
Distribution
Category
uc-20, 20c

DISTRIBUTION

1–4. Argonne National Laboratory, 9700 South Cass Avenue, Argonne, IL 60439

L. Greenwood
V. Maroni
D. L. Smith
H. Wiedersich

5–6. Battelle-Pacific Northwest Laboratory, P.O. Box 999, Richland, WA 99352

J. L. Brimhall
D. Dingee

7. Carnegie-Mellon University, Schenley Park, Pittsburgh, PA 15213

J. C. Williams

8–203. Department of Energy, Technical Information Center, Office of Information Services, P.O. Box 62, Oak Ridge, TN 37830

For distribution as shown in TID-4500 Distribution Category, UC-20 (Magnetic Fusion Energy), and UC-20c (Reactor Materials)

204–209. Department of Energy, Office of Fusion Energy, Washington, DC *20545*

M. M. Cohen
T. C. Reuther, Jr. (5 copies)

210. Department of Energy, Oak Ridge Operations Office, P.O. Box E, Oak Ridge, TN 37830

Office of Assistant Manager, Energy Research and Development

211. General Atomic Company, P.O. Box 81608, San Diego, CA 92138

S. M. Rosenwasser

212—217. Hanford Engineering Development Laboratory, P.O. Box 1970, Richland, WA 99352

D. G. Doran
J. J. Holmes
R. E. Nygren
E. C. Opperman
R. W. Powell
J. L. Straalsund

218—219. Lawrence Livermore Laboratory, P.O. Box 808, Livermore, CA 94550

M. Guinan
C. M. Logan

220. Massachusetts Institute of Technology, Cambridge, MA 02139

D. J. Rose

221—222. McDonnell Douglas Astronautics Company, East, P.O. Box 516, St. Louis, MO 63166

J. W. Davis
D. L. Kummer

223—225. Naval Research Laboratory, Washington, DC 20375

Superintendent, Materials Science and Technology Division
J. A. Sprague
H. Watson

226—253. Oak Ridge National Laboratory, P.O. Box X, Oak Ridge, TN 37830

Central Research Library (2 copies)
Document Reference Section
Laboratory Records Department (2 copies)
Laboratory Records Department, RC
ORNL Patent Section
B. G. Ashdown
E. E. Bloom (5 copies)
D. N. Braski
J. H. DeVan
T. A. Gabriel
M. L. Grossbeck
M. R. Hill (3 copies)
K. C. Liu
P. J. Maziasz
C. J. McHargue
T. K. Roche
J. L. Scott
P. F. Tortorelli
F. W. Wiffen
J. W. Woods

254–255. Sandia Laboratories, Livermore Division 8316, Livermore, CA 94550

J. Swearengen
W. Baller

256. University of California, Department of Chemical, Nuclear, and Thermal Engineering, Los Angeles, CA 90024

R. W. Conn

257. University of Virginia, Department of Materials Science, Charlottesville, VA 22901

W. A. Jesser

258. University of Wisconsin, 1500 Johnson Drive, Madison, WI 53706

W. G. Wolfer

259. Westinghouse Electric Company, Fusion Power Systems Department, P.O. Box 10864, Pittsburgh, PA 15236

R. E. Gold

☆ U.S. GOVERNMENT PRINTING OFFICE: 1980-640-245/017